Alma Mater Studiorum — Università di Bologna

SCUOLA DI SCIENZE
Corso di Laurea Magistrale in Astrofisica e Cosmologia
Dipartimento di Fisica e Astronomia

Kinematics of the circumgalactic medium in early-type galaxies

Tesi di Laurea Magistrale

Candidato:
Andrea Afruni

Relatore:
Chiar.mo
Prof. Filippo Fraternali

Co-relatore:
Dr. Gabriele Pezzulli

Sessione III
Anno Accademico 2015-2016

Contents

Sommario

Un ruolo fondamentale nella formazione ed evoluzione delle galassie è svolto dal mezzo circumgalattico (CGM), una componente ionizzata e diffusa che si estende fino a centinaia di kiloparsec dalla galassia centrale. Questo gas multifase costituisce la connessione tra la galassia e il mezzo intergalattico (IGM) e rappresenta perciò un elemento fondamentale per la comprensione della dinamica del gas all'interno delle galassie. Nel presente lavoro di tesi ci occupiamo principalmente della fase ionizzata fredda di questo gas ($T < 10^5$ K), osservata tramite righe in assorbimento UV negli spettri di quasar di background. Lo scopo di questo lavoro è quello di caratterizzare la cinematica e le proprietà di questo gas, focalizzandoci in particolare sulle galassie ellittiche. I nostri modelli sono basati sulle osservazioni del gruppo di COS-Halos, che ha analizzato il CGM di galassie a basso redshift osservando diverse nubi con differenti proprietà cinematiche, legate alla galassia centrale. In particolare, cerchiamo di riprodurre i due principali vincoli forniti da queste osservazioni: la dispersione di velocità delle nubi e le densità di colonna dell'idrogeno. Una particolarità di questi assorbitori è quella di avere, nelle galassie ellittiche, una dispersione di velocità molto più bassa rispetto alla dispersione viriale aspettata per queste galassie massive, peculiarità che i nostri modelli si propongono di riprodurre.
Nel corso di questa tesi vengono presentati una notevole quantità di modelli cinematici, costruiti utilizzando assunzioni molto diverse fra loro ed esplorando lo stato di equilibrio e di non equilibrio dinamico per descrivere il moto delle nubi. In prima analisi riportiamo uno studio delle caratteristiche fisiche di queste nubi, che ci porta ad escludere che possano essere supportate dalla loro autogravità. Attraverso l'utilizzo di simulazioni idrodinamiche viene poi analizzata la sopravvivenza degli assorbitori all'interno degli aloni delle galassie. I risultati forniti da queste simulazioni portano a concludere che queste nubi vengono molto probabilmente distrutte nelle regioni più interne dalle violente interazioni con la corona di gas caldo, che assume in queste regioni densità molto elevate. Nelle regioni più esterne invece, il gas caldo è molto diffuso e il moto delle nubi è assumibile come balistico, non influenzato dalle interazioni con il mezzo circostante. Dopo aver analizzato il loro stato fisico, il nostro lavoro si concentra principalmente nella creazione di modelli cinematici atti a spiegare le osservazioni di COS-Halos, in particolare la dispersione di velocità e le densità di colonna. In un primo momento

ci occupiamo di modelli di equilibrio non collisionale, risolvendo l'equazione di Jeans attraverso l'utlilizzo di differenti distribuzioni di densità e profili di dispersione ed esplorando parametrizzazioni molto diverse tra loro. Questa analisi porta ad escludere una grande varietà di modelli e a trovare che i modelli migliori sono descritti da nubi le cui orbite hanno una forte anisotropia tangenziale che le forza ad essere confinate nelle regioni esterne, in accordo con le precedenti considerazioni sulla sopravvivenza delle nubi.
Infine, descriviamo questo sistema attraverso modelli di non equilibrio, rappresentanti un flusso di nubi verso il centro della galassia, accresciute dal mezzo intergalattico o formatesi dalla condensazione del gas caldo tramite instabilità termiche. Esplorando anche in questo caso una grande varietà di modelli, concludiamo che i risulati più simili alle osservazioni si ottengono con modelli caratterizzati da nubi accresciute dall' IGM, rallentate dalla forza di drag esercitata dalla corona e distrutte infine dalle interazioni col gas caldo.

Abstract

A fundamental role in galaxy formation and evolution is played by the CircumGalactic Medium (CGM), a very diffuse and ionized multiphase gas that extends to hundreds of kiloparsecs from the central galaxy. The CGM constitutes the interface between galaxies and the intergalactic medium (IGM) and modelling its kinematics and dynamics is critical to improve our understanding of galaxy inflows and outflows. In this thesis, we focus on the cold ionized phase ($T < 10^5$ K), observed through UV absorption lines in the spectra of background quasars, with the aim to understand its kinematics and physical state, in particular for early-type galaxies. Our work is based on the observations of the COS-Halos collaboration, who observe the cold CGM of nearby galaxies, finding that this phase is composed by several clouds bounded to the central galaxies. Our goal is to reproduce, using kinematic models, the two main constraints given by these observations: the velocity dispersion and the hydrogen column density as a function of the projected radius. Interestingly, the observed velocity dispersion of these clouds is too low in early-type galaxies with respect to the expected virial dispersion and explaining this small value is one of the main goals of our study.
In this Thesis we create a wide variety of models, with very different assumptions, and we investigate the equilibrium and the non-equilibrium state of the absorbers. First, we study the physical state of the cold clouds, through analytic calculations and hydrodinamical simulations. We find that these clouds cannot be supported by their own gravity and that they cannot survive in the internal regions of the halos, where the interactions with the hot dense coronal gas would likely destroy them. These interactions are instead weak in the outer regions, where the hot gas is more diffuse, and the clouds have a nearly ballistic motion.
We describe then the kinematics of the clouds with collisionless equilibrium models, using the Jeans equation and solving it with very different assumptions for the cloud density distribution and the radial velocity dispersion profile, exploring various parametrizations. We find that we can reproduce both the observational constraints (velocity dispersion and column density profile) only if the clouds are confined to the external regions of the halos by tangentially biased orbits, in agreement with our findings for the cloud survival.
Finally, we investigate models that describe a global inflow of the CGM clouds towards

the galaxy, assuming that they are accreted from the IGM or created at large radii by the condensation of the hot corona due to thermal instabilities. We find successfull models with clouds coming from the IGM, slowed down by the drag force acted by the corona and disrupted by the hydrodynamical interaction with the hot gas at a given internal radius.

Chapter 1

Introduction

Galaxies are commonly discovered and charachterized through their two most easily observable components, the stars and the interstellar medium (ISM). The latter is composed of gas and dust, lies between the stars and extends at most to a few tens of kiloparsecs from the centre of graviational potential. However, counting all the baryons associated with these components (e.g., McGaugh et al., 2010), the ratio between $M_{\rm bar}$ (the mass of observed baryons) and $M_{\rm tot}$ (the total mass including the dark matter) is significantly lower than the expected value of 0.17 (Planck Collaboration et al., 2016), predicted by cosmological theory. This means that baryons are apparently missing from galaxies, which is known as the *missing baryon problem*. A possible solution to this problem is that the missing baryons are present in some undetected form, within the dark halo.
In the last decades, X-ray and UV observations (Forman et al., 1985; Lanzetta et al., 1995; Wakker and Savage, 2009) have revealed a third fundamental component of galaxies: the **CircumGalactic Medium** (CGM, Shull, 2014), a very diffuse and ionized multiphase gas that extends to hundreds of kiloparsecs, out to the virial radius. The CGM is a reservoir of gas that may have as much mass as the stellar component and may provide an explanation to the missing baryon problem.
Moreover, this medium is the connection between the galaxies and the intergalactic medium (IGM) and can fuel the star formation of disc galaxies (Crighton et al., 2013). The CGM is therefore a source of information about the past and future of galaxies. Determining the interplay between the galaxies and CGM is essential to understand how galaxies form and evolve.

1.1 CGM phases

We call CGM the mainly ionized gas which lies in the galaxy halos and extends out to the virial radius, connecting the intergalactic medium with the galaxies. This medium

is not homogeneus and is composed by various components. In this work, we define in particular three different phases, with different temperatures:

- *Hot CGM* at $10^6 < T \leq 10^7$ K
- *Warm-Hot CGM* at $10^5 \leq T \leq 10^6$ K
- *Cold CGM* at $T < 10^5$ K

1.1.1 Hot CGM

Classical cosmological models predict the presence of hot gas surrounding galaxies (*corona*), heated by continuous shocks to the galaxy virial temperature and in hydrostatic equilibrium with the dark matter halo (White and Rees, 1978; White and Frenk, 1991). Unfortunately, this diffuse gas is hard to detect, due to its low density and therefore to its low X-ray surface brightness, and it is to date poorly characterized.
The Einstein Observatory detected hot gaseous halos around Early-Type Galaxies (ETGs) decades ago (Forman et al., 1979, 1985) and since then the emission from massive ETGs have been extensively studied (Sarazin et al., 2001; Jones et al., 2002; Mathews and Brighenti, 2003; Bogdán and Gilfanov, 2011), through X-ray observations. It is however hard to distinguish between the hot gas accreted from the IGM (hot mode accretion) and that expelled from the galaxy (e.g. due to stellar mass loss). In late type galaxies instead, the first detections were carried out with the new generation of X-ray telescopes, with strong evidence only for the more massive galaxies (Anderson and Bregman, 2011; Dai et al., 2012; Bogdán et al., 2013). In Figure 1.1 we show one such detection of hot diffuse gas in the giant spiral galaxy NGC 196, performed by Anderson and Bregman (2011). In this kind of galaxies, the coronal gas is more diffuse, and of a lower luminosity, than predicted by the analytic models of White and Frenk (1991), as explained in Crain et al. (2010).
A recent analysis of large samples of galaxies, performed using stacking technique (Anderson et al., 2013), finds that emission from a hot gas halo is present in almost all massive galaxies, both early and late type, and that the early-type galaxies have generally more extended and luminous coronae. In our own Milky Way, the presence of a hot corona was first hypothesized by Spitzer (1956) as the medium that provides pressure confinement to the High- Velocity Clouds (HVCs, see Section 1.1.3). It has recently been observed, with several indirect indications, like the head-tail structure of several HVCs (Putman et al., 2011) or absorption lines in quasar spectra (Yao et al., 2012; Miller and Bregman, 2013), and recent direct observations of several emission lines of OVII and OVIII (Miller and Bregman, 2015). In all galaxies, the hot coronal gas should contain at least as much mass as the galaxy stellar component (e.g. Gatto et al., 2013), but its mass is always much smaller than the one associated with the missing baryons of the galaxy (e.g. Miller and Bregman, 2015).

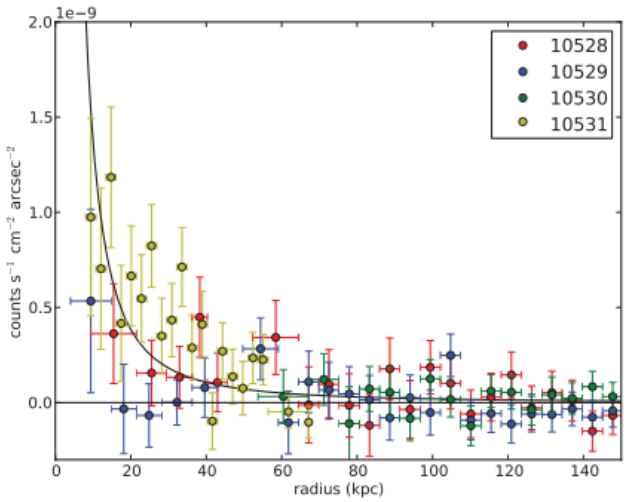

Figure 1.1: Radial X-ray surface brightness profile of the isolated giant spiral galaxy NGC 196, after the subtraction of the background. The black line is the best-fit β-model to the data. The data points represent four different observations of different regions of the same galaxy (from Anderson and Bregman, 2011).

1.1.2 Warm-Hot CGM

The warm gas phase is observed through the absorptions of highly-ionised species, expecially the OVI (Tumlinson et al., 2011; Werk et al., 2013, 2016). The incidence of detection of this gas is found to be larger around star-forming galaxies than around passive early-type galaxies with little or no star formation, suggesting that its presence could be related to the galaxy stellar feedback.
OVI is detected also in our Galaxy, with a covering fraction larger than 60% (Sembach et al., 2003) and ionization models (e.g. CLOUDY, Ferland et al., 1998) found that highly-ionised elements represent collisionally ionized gas, due to the interaction between cold clouds and the hot corona of the Milky Way (e.g. Fox et al., 2010).

1.1.3 Cold CGM

We divide the cold CGM phase in two distinct components:

- *neutral gas*, which is observed in late type galaxies and extends to $\sim$ 10 kpc from the disc;
- *ionized gas*, which is observed both in early and late type galaxies and extends to the galaxy virial radius.

Thick layers of extra-planar, neutral gas have been detected, through the neutral hydrogen (HI) 21-cm line emission, both in the Milky way and in nearby spiral galaxies (Sancisi et al., 2008), with an extension of ~ 10 kpc and a quite regular kinematics. In our galaxy there are numerous detections of extra-planar gas in the form of anomalous clouds, the so called High Velocity Clouds (Wakker and van Woerden, 1997), whose velocities deviate from the speed predicted by a differentially rotating thin disc by more than ~ 90km s^{-1} (Wakker, 1991). These metal-poor clouds, observed recently also in other galaxies (Oosterloo et al., 2007), have been generally considered the first evidence of accretion of cold gas from the IGM (Oort, 1970). There are however no detections of these clouds at large galactocentric distances, opposite to what is expected from an IGM origin. The low metallicity excludes the purely internal origin, but is possible that they arise from the interactions between the gas ejected from the disc and the coronal gas (Fraternali and Binney, 2008; Fraternali et al., 2013).

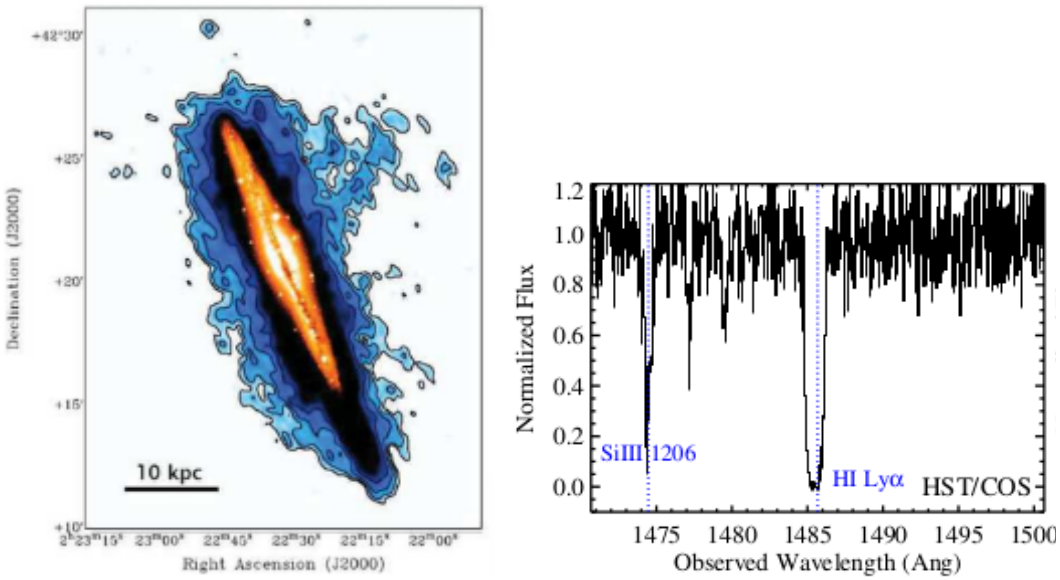

Figure 1.2: Left panel, HI map (blue) overlaid to the optical image (orange) of the extra-planar gas in the nearby galaxy NGC 891 (from Oosterloo et al., 2007). Right, an example of an HST/COS spectrum from the COS-Halos QSO-galaxy sample, focused on the HI Lyα absorption line (from Werk et al., 2013).

In the last decades a more diffuse and ionized medium, which extends to hundreds of kiloparsecs from the galactic centre, has been discovered both around passive and star-forming galaxies (Lanzetta et al., 1995; Stocke et al., 1995; Penton et al., 2002; Wakker and Savage, 2009; Prochaska et al., 2011). It is impossible to directly detect this gas in emission with any present-day telescope, due to its very low density. It

is therefore observed with UV absorption lines in the spectra of background quasars, with a multitude of transitions including the HI Lyman series and intermediate-low ions (e.g. the COS-Halos collaboration, see Chapter 2). Line diagnostics have revealed that this medium, despite the large galactocentric distances, is bounded to the central galaxy, because the velocities of the absorbers are lower than the virial velocities of the galaxies (Werk et al., 2013; Tumlinson et al., 2013). Mass estimates suggested that more baryons reside in this medium than in the stellar component of the galaxies (Werk et al., 2014). This estimate is however uncertain, due to the dipendence of this result on the photoionization models used in the analysis (Werk et al., 2016; Stern et al., 2016). To date, the origin of this gas is not clear and we do not have enough constraints to distinguish between various scenarios: they can come from galaxy outflows or IGM inflows or maybe they could be created by coronal instabilities (Maller and Bullock, 2004; Binney et al., 2009) or stripped from satellite galaxies.

1.2 CGM in galaxy formation and evolution

In the structure formation theory, the present inhomogeneities of the matter distribution in the Universe developed from initial density perturbations, which gravitationally collapsed. In the classical picture of galaxy formation, the baryonic matter falls into the dark matter potential wells and it is shock-heated to the virial temperature of the halo (White and Rees, 1978). The fate of the gas depends on the cooling time (Rees and Ostriker, 1977):

$$t_{\rm cool} = \frac{3 k_{\rm B} T m_{\rm p}}{\rho_{\rm gas} \Lambda(T)} \tag{1.1}$$

where T is the gas temperature, $m_{\rm p}$ the proton mass, $\rho_{\rm gas}$ the gas density, $k_{\rm B}$ the Boltzman costant and $\Lambda(T)$ the cooling function. If the cooling time of the halo gas is larger than the Hubble time, the cooling will not be effective and the hot medium remains mixed with the dark matter halo, preventing the formation of a galaxy. In the oppositely extreme case, if the cooling time is shorter than both the Hubble time and the free-fall time, the gas is not shock-heated and collapses to the centre (Binney, 1977), through gas flows along dark matter filaments: this scenario is called *cold mode accretion*. An intermediate case will lead to a central galaxy formed by the progressively cooling of hot corona (see Section 1.1.1) , which is called *hot mode accretion* (e.g. Birnboim and Dekel, 2003; Dekel and Birnboim, 2006). These different scenarios are predicted by both analytic models and ΛCDM cosmological simulations and the accretion mode is related to the halo mass: above a critical mass of $\sim 2-3\times10^{11}$ $\rm M_{\odot}$, the gas is expected to be heated by shocks to about the virial temperature, while for lower masses cold mode accretion dominates. Simulations predict that even in high mass halos cold filamentary flows exist at high redshift, as shown in Figure 1.3, while their importance decreases at lower redshifts.

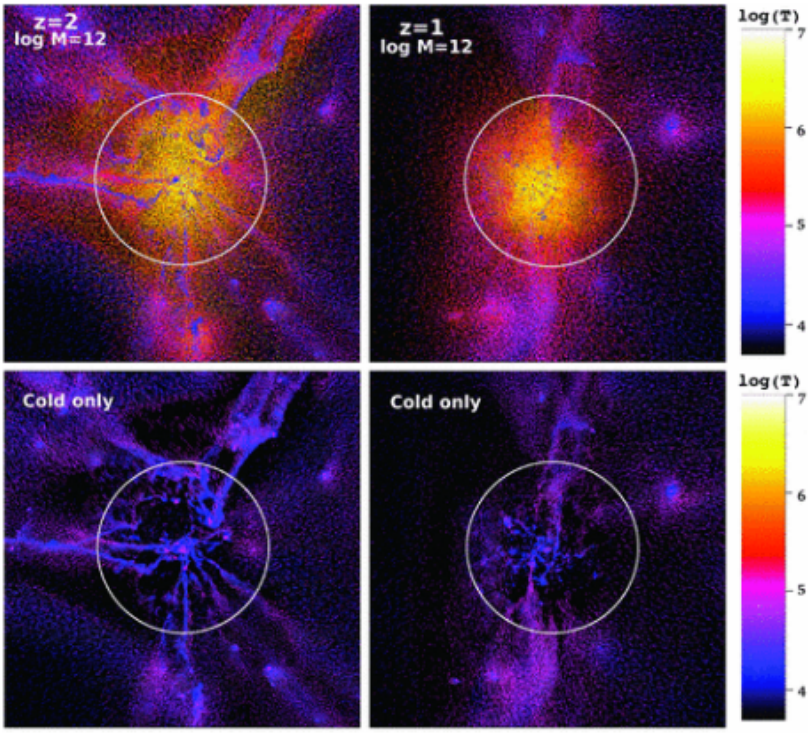

Figure 1.3: Temperature snapshots of a cosmological ΛCDM simulation of a Milky Way like galaxy from Kereš et al. (2009). The box is 1 h^{-1} Mpc (comoving) onn a side and 1 h^{-1} Mpc (comoving) in projected depth. Left panels show the galaxy at $z = 2$ and right panels at $z = 1$. Upper panels show all the galaxy particles, lower panels only the gas with $T < 10^5$ K, with the same colour scale. The circles indicate the virial radius.

Opposite to the accretion flows, galaxies eject material in the halos through outflows due to the central AGN activity (AGN feedback) or to the stellar compononent (stellar feedback: supernovae and stellar winds). Recent simulations (Ford et al., 2013) suggest that the most of the observed cold/warm gas absorption is due to large-scale galactic outflows. If the gas velocity is larger than the escape velocity the material is ejected in the IGM, otherwise it falls back and contributes to the "pollution" of the CGM out to the virial radius. Galactic outflows are a common features of vigorously star-froming galaxies in the local universe (Heckman et al., 2000; Shapley et al., 2003; Weiner et al., 2009) and are detected through multi-wavelength observations from X-ray to radio. They are composed of hot plasma (e.g. Strickland and Heckman, 2007), cold neutral and ionized material (e.g. Martin et al., 2012) and even molecular gas (Bolatto et al., 2013). Rubin et al. (2014) found that biconical outflows along the minor axis are nearly ubiquitous in star-forming galaxies. In ETGs instead, the predominantly old stellar

populations, together with little or no ongoing star formation, suggest a smaller contribution of outflows to their CGM.
In the modern picture, galaxy evolution is strongly influenced by gas outflows and inflows. The inflows from the IGM can feed the galaxy star formation and are counteracted by galactic outflows that also cause the metal enrichment of the IGM. A complete understanding of this *baryon cycle* is crucial to understand how galaxies evolve, and in this respect the circumgalactic medium plays a fundamental role, because it is the "interface" between galaxy discs and the IGM.

1.3 This Thesis

In the rest of this Thesis we use the term CGM to refer to the cold ionized gas phase described in Section 1.1.3. In the current picture this gas is associated to the baryon cycle scenario, with many claimed detections of inflows (Kacprzak and Churchill, 2011; Rubin et al., 2012; Crighton et al., 2013) and outflows (e.g. Rubin et al., 2010, 2014; Kacprzak et al., 2014), although its kinematics is often poorly constrained due to projection effects. Our goal is to characterize the kinematics of this phase, with models that reproduce the observational constraints given by the COS-Halos collaboration (Chapter 2). Interestingly, the observed properties of this gas are similar in star-forming and early-type galaxies (Thom et al., 2012). Here, we focus only on early-type galaxies, because the lack of star formation and galactic outflows make them easier to characterize than the star-forming one, with the aim to study also the latter with future works. The main goal of this thesis is therefore to explain the kinematics and densities of the cold circumgalactic medium in passive galaxies, in order to improve our understanding on the origin and fate of this elusive gas phase.
This thesis is structrured as follows: in Chapter 2 we describe the COS-Halos observations and we define the sample of ETGs which we analyse with our models; in Chapter 3 we study the physical state of the circumgalactic medium in early-type galaxies, through analytic calculations and hydrodynamical simulations; in Chapter 4 we show some equilibrium models, based on the Jeans equation, that aim to describe the CGM as a system of collisionless clouds; in Chapter 5 we show a set of infalling models to explain the CGM kinematics, alternatively to the equilibrium models; finally, in Chapter 6 we discuss our results and present our conclusions and future perspectives.

Chapter 2

COS-Halos observations

In this chapter we describe and discuss the observations and results carried out by the COS-Halos collaboration. They observed and characterized absorption lines (arising from cold/warm clouds) in the CGM of nearby galaxies. In this Thesis we focus on early-type galaxies and investigate physical models to explain the presence and the properties of the observed absorption features of the cold ionized gas ($T < 10^5$ K, see Section 1.1.3). In particular we aim to reproduce two key observables: the observed velocity dispersion and total hydrogen column densities of the absorbers. In Section 2.1 we describe the COS-Halos sample, their data analysis and their main results. In Section 2.2 we describe the results obtained using photo-ionizations models, in particular the CGM densities and masses, and we show our analysis on the uncertainties of this modelling. In Section 2.3 we describe in more detail our subsample of early-type galaxies.

2.1 Sample and data

The COS-Halos program is a survey of the CGM around a sample of low-redshift $L \sim L_*$ galaxies, performed using the Cosmic Origin Spectrograph (COS, Froning and Green, 2009; Green et al., 2012) aboard the Hubble Space Telescope (HST). The primary goal of this program is to examine, through the analysis of absorption lines in the spectra of background quasars (QSOs), the CGM content in low-redshift galaxies and to study its properties and its role in the galaxy baryon cicle (see Section 1.2).

2.1.1 QSO and galaxy selection

In this section we describe how the sample of galaxies was drawn by the COS-Halos collaboration and we outline the main properties of the selected galaxies. COS-Halos selected 38 galaxies from the Sloan Digital Sky Survey, based on their photometric

redshifts ($z_{\rm phot} \approx 0.15 - 0.4$), with impact parameters from the background quasars that range from 10 to 160 kpc, well inside the virial radii of these galaxies ($r_{\rm vir} \sim 200 - 800$ kpc). They consider a wide range of galaxy colors and stellar masses ($M_* \approx 10^{9.5} - 10^{11.5}$ $M_\odot$). Because of the uncertainties in the photometric redshift, in a second moment spectroscopic redshifts pf the galaxies in the sample were obtained. Five galaxies turned out to be at $z \lesssim 0.1$ and thus have correspondingly lower stellar mass and luminosity than expected, out of the selection range. Therefore, these five galaxies were discarded from the main sample and the study was restricted to galaxies with $L > 0.1\ L_*$. In addition to the targeted galaxies, also 21 "bonus" galaxies were discovered at close impact parameters from the QSOs and with the requested selection criteria of $z < z_{\rm qso}$ and $L > 0.1\ L_*$. Although not primary targets, these galaxies were included in the analysis in addition to the targeted objects and were treated in an identical fashion as the others. Almost all the bonus and targeted galaxies are isolated, as assessed by previous analyses of SDSS spectroscopy and photometry (Koester et al., 2007). The total sample was then modified by based on other selection criteria, explained in detail in Tumlinson et al. (2013). The final sample was composed of 44 absorption systems, each associated to the CGM of an $L \sim L_*$ galaxy.

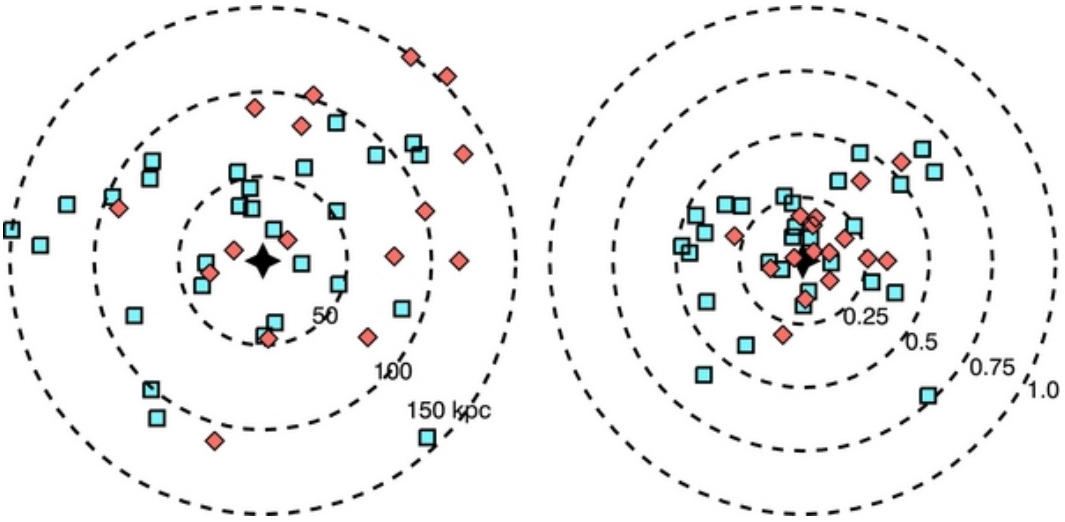

Figure 2.1: Projected distances of the 44 sightlines from their associated galaxy, shown at the centres of the two panels. Red symbols depict early-type galaxies while blue symbols depict star-forming galaxies. Left panel, distances in physical units; right panel, distances in fractions of the virial radius (from Tumlinson et al., 2013).

Figure 2.1 shows the position of the sightlines in the sample with respect to their associated galaxy, in physical units on the left and in fractions of the virial radius on the right. The blue symbols are for sightlines crossing the CGM of star-forming

galaxies, while red symbols are for sightlines crossing the CGM of passive galaxies. The distinction between the two types of galaxies is done on the basis of their specific Star Formation Rate (sSFR), as estimated from Hα and $[OII]$ emission lines (using the H$\alpha - SFR$ calibration from Kennicutt (1998) and the $[OII] - SFR$ calibration from Kewley et al. (2004)). Galaxies are classified as star-forming if they have $sSFR > 10^{-11}\mathrm{yr}^{-1}$, while they are classified as early-type if they have $sSFR < 10^{-11}\mathrm{yr}^{-1}$. Note that only the projected distances of the absorbers from the central galaxy are known, while the intrinsic galactocentric distances of the CGM absorbers are not. In principle, the absorption lines may arise from gas at hundreds of kiloparsecs from the centre and low impact parameters be due only to projection effects. This consideration will be critical for our models in the following chapters[1]. Figure 2.2 shows the distributions of the SFR, the stellar masses, the distances from the backround quasars and the luminosity of the 44 galaxies of the sample.

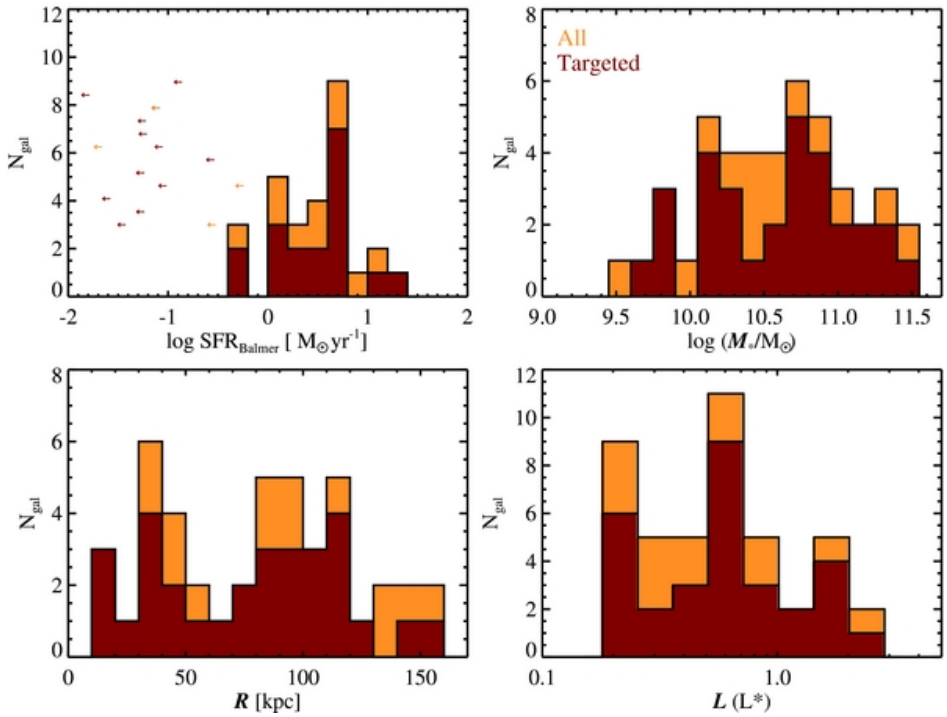

Figure 2.2: Distributions of the SFR (obtained from the balmer emission lines), the stellar masses, the projected distances from the background quasars and the luminosity of the 44 COS-Halos galaxies, with distinctions between the targeted (brown) and the total (orange) sample (from Werk et al., 2013).

[1]Throughout this Thesis, we use r to refer to intrinsic radii and R to refer to projected radii.

2.1.2 Data analysis and line measurements

For each sightline, COS-Halos performed absorption line diagnostics using the COS spectra, spanning $\lambda \approx 1150 - 1800$ Å with a resolution of 15 km s^{-1}. In addition to these spectra, for 35 quasars of the sample described above they used the Keck/HIRES (High Resolution Echelle Spectrograph) spectra, which have a resolution of 6 km s^{-1} and a nearly continuous wavelength coverage from $\lambda \approx 3050$ to 5880 Å. At $z > 0.1$, these spectra cover the MgII doublet, an excellent diagnostic of cold metal-enriched gas.
Tumlinson et al. (2013) searched for HI absorption lines within ± 600 km s^{-1} from the galaxy systemic velocity, while Werk et al. (2013) inspected the COS and HIRES spectra to find UV transitions of low ionization species in their expected spectral positions. They found only 4 non-detections of the $Ly\alpha$, all in passive galaxies, and they found detections of at least one metal absorption line in 33 galaxies (9/16 from the quiescent sample and 24/28 from the star-forming sample). In contrast to the low ions, they found a clear dicothomy in the detection of the OVI lines, which were observed only in star-forming galaxies. For both hydrogen and metals they measured the rest-frame equivalent widths and column densities, using the apparent optical depth method (AODM, Savage and Sembach, 1996), which converts the normalized flux spectrum into an optical depth and then to an apparent column density.

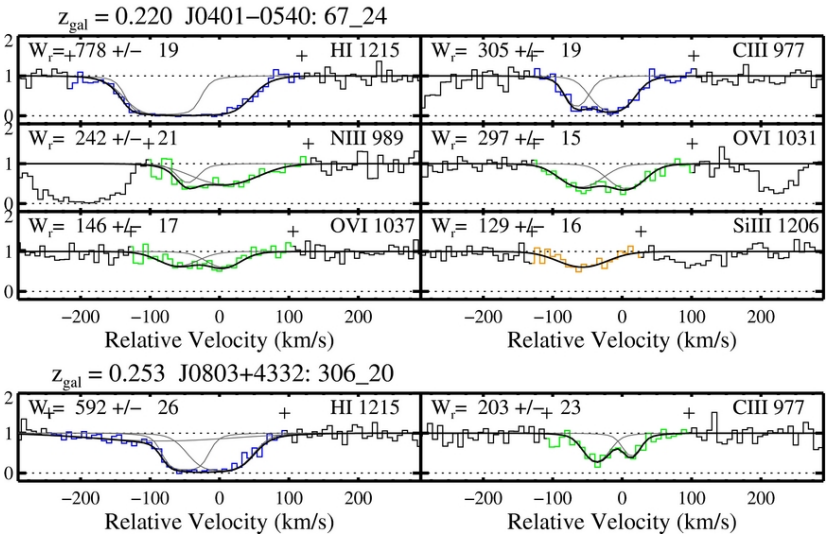

Figure 2.3: Velocity plots of the observed species observed in absorption in the sightlines J0401-0540, galaxy 67_24 and J0803+4332, galaxy 306_20, centered on the absorption lines included in the analysis. The various lines show the Voigt profiles associated to the different kinematics component. Green depicts an uncorrupted detection, blue indicates that the line is saturated and orange indicates that the line is blended with some intervening absorption. (from Werk et al., 2013).

For each line of sight they observe for every species various components with different velocities. Therefore, in order to study the single kinematic components, they fitted Voigt profiles to the absorption features. They derived for each kinematic component the column density N, the Doppler factor b (the component width in km s^{-1}) and the velocity offset from the galaxy systemic velocity δv. The total fit column densities are predominantly consistent with those derived using AODM. Figure 2.3 shows the velocity plots of the observed species, drawn from the spectra of two different sightlines, with overlaid the fits of Voigt profiles.

2.1.3 Properties of the cold CGM

Here we summarize the main results found by Tumlinson et al. (2013) and Werk et al. (2013) using the line diagnostic above. We focus in particular on the results obtained for the HI and the low-ionized species, which trace the cold gas phase of the circumgalactic medium, with $T \lesssim 10^5$ K, described in Section 1.1.3. The two panels of Figure 2.4 show the measured AODM column densities of HI and low-ions. Interestingly, they appear to be quite similar in the CGM of both star-forming and early-type galaxies. The high detection rate of HI and metal ions, leads to the conclusion that the presence of a cold, ionized CGM phase is nearly ubiquitous around $L \sim L_*$ galaxies, out to at least 160 kpc.

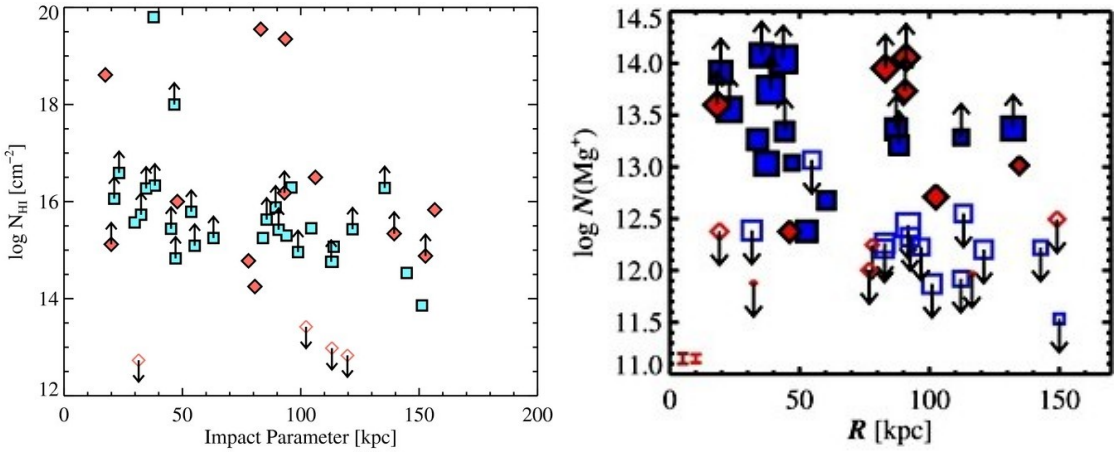

Figure 2.4: Column densities of the neutral hydrogen (left, from Tumlinson et al., 2013) and of MgII (right, from Werk et al., 2013).

Regarding the kinematics of this cold phase, in Figure 2.5 we show the HI and metal velocity offsets from the galaxy systemic velocity as functions of the virial (HI, left panel) and the stellar (metals, right panels) masses of the central galaxies. The majority of the velocities inferred from HI and metal lines lie within $\pm$200 km s^{-1} from the galaxy

systemic velocity. The curves in the left-hand panel show the escape velocity at 50, 100 and 150 kpc from the centre. We can see that the majority of the points are inside these lines, which implies that the CGM absorbers are bound to the galaxies. Interestingly, the observed velocity range is nearly independent on the galaxy mass, with the conseguence that the CGM absorbers around massive early-type galaxies have velocities much lower than the escape one. We will see in Section 2.3 that their velocity dispersion is indeed much smaller than the virial dispersion expected for this kind of galaxies and the physical interpretation of this result is not trivial. Understanding why the absorbers bounded to massive early-type galaxies have this small observed velocity dispersion is one of the main goals of our work.

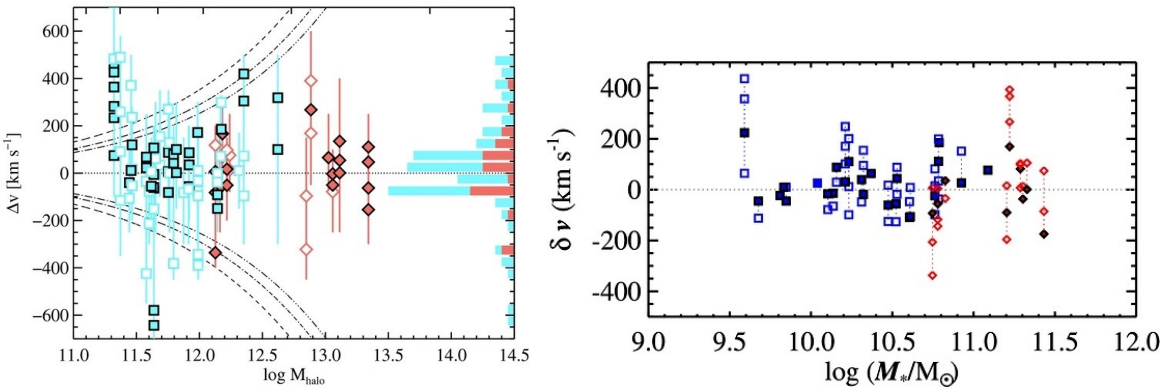

Figure 2.5: Velocity offsets from the galaxy systemic velocity inferred from the HI ($Ly\alpha$) absorptions (left, from Tumlinson et al., 2013) and from the absorptions of the metal ions (right, from Werk et al., 2013). The curves in the left panel show the escape velocities at 50, 100 and 150 kpc from the centre of the halos.

2.2 Photo-ionization models

Werk et al. (2014) applied photo-ionization models to the two datasets of the previous works, obtained from the HI and metal absorption line diagnostics, focusing on the 33 COS-Halos galaxies which exhibit metal absorptions. They used the version 13.03 of the spectral synthesis code CLOUDY (Ferland et al. 1998, 2013), to compute the total hydrogen column and number densities of the cold CGM, in order to estimate the total CGM mass for each galaxy. They applied the photo-ionization models to each one of the 33 selected galaxies. The fundamental assumptions adopted for this modelling are:

1. The low and intermediate ions observed in the COS spectra (e.g., SiII, SiIII; CII, CIII) are co-spatial and arise from a single gas phase.

2. The CGM probed by this absorption is a cold medium with $T < 10^5$ K, in which photoionization dominates over collisional excitation.

3. The gas is in ionization equilibrium.

4. The gas is assumed to be a uniform slab.

The OVI absorption lines are excluded from the analysis because it is quite likely that they do not fulfill hypothesis 1 (Werk et al., 2016). In particular, trhough the photo-ionization models Werk et al. (2014) obtained the values of the total hydrogen column density N_H (neutral and ionized) and of the ionization parameter U, defined as:

$$U = \frac{\Phi}{n_H c} \ , \tag{2.1}$$

where c is the speed of light, n_H is the total hydrogen volume density and Φ is the total flux of ionizing photons. Then, from the values of the ionization parameter, they inferred the hydrogen volume densities inverting equation (2.1), fixing the value of the ionizing flux ($\sim 1.21 \times 10^4$ cm^{-2} s^{-1} , as defined by Haardt and Madau (2001)).

2.2.1 Results obtained by the CLOUDY analysis

In Figure 2.6 we show the resulting total hydrogen column and volume densities, inferred from the CLOUDY models. Due to the uncertainities of the photo-ionizations modelling (see next section), the mean uncertainty of N_H is ± 0.5 dex.
Using a mean value of the total column densities, Werk et al. (2014) calculated the total contribution of the photoionized CGM to the baryonic budget of an $L \sim L_*$ galaxy, treating the COS-Halos sightlines as probes of a single "fiducial" galaxy halo. They found the mass of the cold CGM through the equation:

$$M_{\rm cold} = \int_0^{r_{\rm vir}} 2\pi R \Sigma_{\rm gas}(R) dR \ , \tag{2.2}$$

where $\Sigma_{\rm gas} = 1.4 m_p N_H$ is the CGM mean surface density (the 1.4 factor corrects for the presence of helium), and the median value of the COS galaxy virial radii is ~ 300 kpc. With these assumptions, the resulting mass of the cold CGM is $M_{\rm cold} = 1.2 \times 10^{11}$ M$_\odot$. Finally, they estimated the sizes of the individual CGM clouds, obtaining sizes that range from 0.1 to 2000 kpc, with up to three orders of magnitude uncertainty for the sightlines with the least-constrained CLOUDY solutions. The high uncertainties on the cloud sizes and the absurd values found for some cloud radii are mainly due to the photo-ionization modelling, that we describe in the following section.

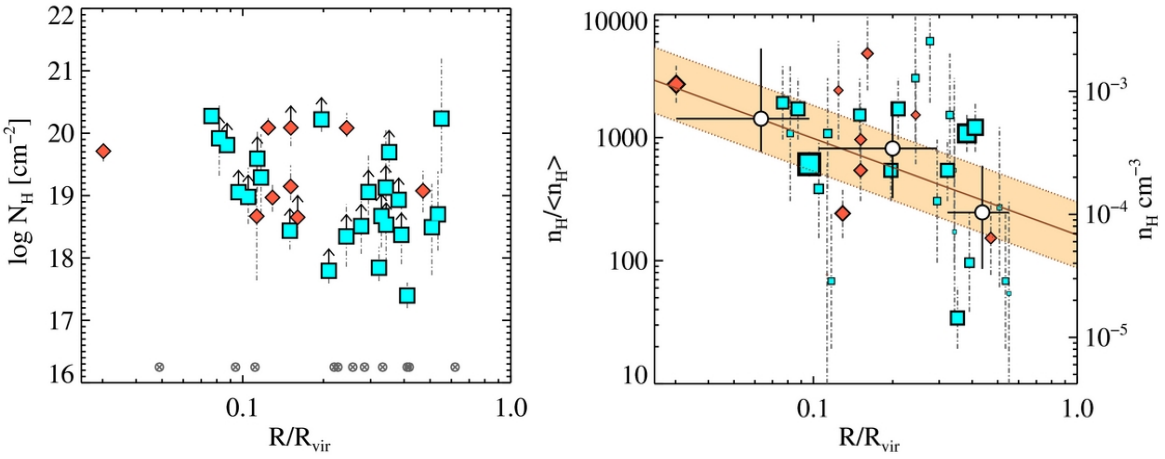

Figure 2.6: Total hydrogen column (left) and volume (right) densities, inferred from the CLOUDY analysis, as a function of the projected radius. The blue symbols depict star-forming galaxies, the red symbols early-type galaxies. In the right panel the three white points depict the data binned in three different ranges of projected radii (from Werk et al., 2014).

2.2.2 CLOUDY modelling

In this section we describe in detail the photoionization modelling, in order to investigate the uncertainties related to this analysis. In particular we focus on the galaxy 67_24 of the line of sight J0401−0540. To perform the CLOUDY models, Werk et al. (2014) used as CLOUDY inputs the solar abundances of Asplund et al. (2009) and the UV background radiation field from Haardt & Madau (2001) at $z \approx 0.2$, which is the mean redshift of the observed galaxies. Then they created a grid of models, changing as inputs the value of the metallicity, that varies from 0.001 to solar metallicities, and of the ionization parameter U, with $\log U$ varying from -5 to -1. Their results are shown in the right panel of Figure 2.7. Here the metallicity is already fixed at the preferred value to reproduce the observations, while the curves of different colours represent the column densities obtained by the CLOUDY models as a function of the ionization parameter. Note in particular that, fixed the background ionizing flux, the value of the ionization parameter defines also n_H and vice versa, due to equation (2.1). In the left panel we show instead our results obtained performing a similar analysis, using the same assumptions and inputs of Werk et al. (2014) for the CLOUDY models. The results are consistent with each other.
To find the ionization paramater of each galaxy, Werk et al. (2014) compared the CLOUDY outputs with the observed column densities (those found with the NAODM, see Section 2.1.2). In the right panel of Figure 2.7, the lines are in bold where they are consistent with the observed value. The yellow stripe represents the range of ionization

parameters that give results comparable with the observations. In particular, to infer the values of U, Werk et al. (2014) focus on the low-ionized species, that trace the cold gas (the OVI curve is reported in the figure for reference, but it was not used to infer the U values). Moreover, the photoionization models give the value of the total hydrogen column density N_H, which can be, if the ionization parameter is high, much higher than the column density of the neutral hydrogen N_{HI}, due to a large fraction of ionized gas.

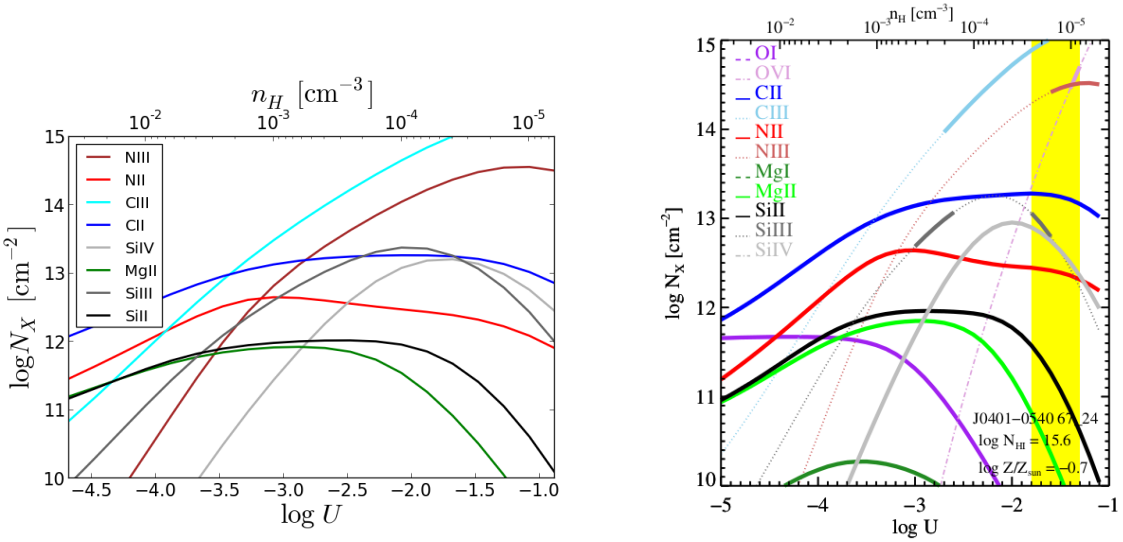

Figure 2.7: Column densities as a function of the ionization parameter and the intrinsic number density, calculated with CLOUDY assuming the ionizing flux of Haardt & Madau (2001) and the solar abundances from Asplund et al. (2009). The left panel shows our work, while the right panel shows the result of Werk et al. (2014). The yellow vertical stripe represents the range of allowed ionization parameters, because it gives results consistent with the observations (bold lines). In particular, for this galaxy, the most useful ions in constraining the ionization parameter are the SiIII, NIII and CIII because they are reliably measured.

In order to investigate the uncertainities of this analysis, we created similar model grids, changing different inputs. The two panels of Figure 2.8 show grids with the same previous properties, changing only the choice of the solar composition (left panel) and of the UV background flux (right panel). For the first grid of models (shown in the left panel of Figure 2.8), we used, instead of the Asplund et al. (2009) solar abundances, the default abundances of CLOUDY (Grevesse and Sauval, 1998; Holweger, 2001; Allende Prieto et al., 2001). With these conditions, we obtained results which are very similar to the previous one, as is shown by the comparison between the left panels of Figures 2.7 and 2.8. The CLOUDY outputs using these two different kinds of models are nearly the same. Therefore, the choice of the solar metallicities does not influence

the CLOUDY results.

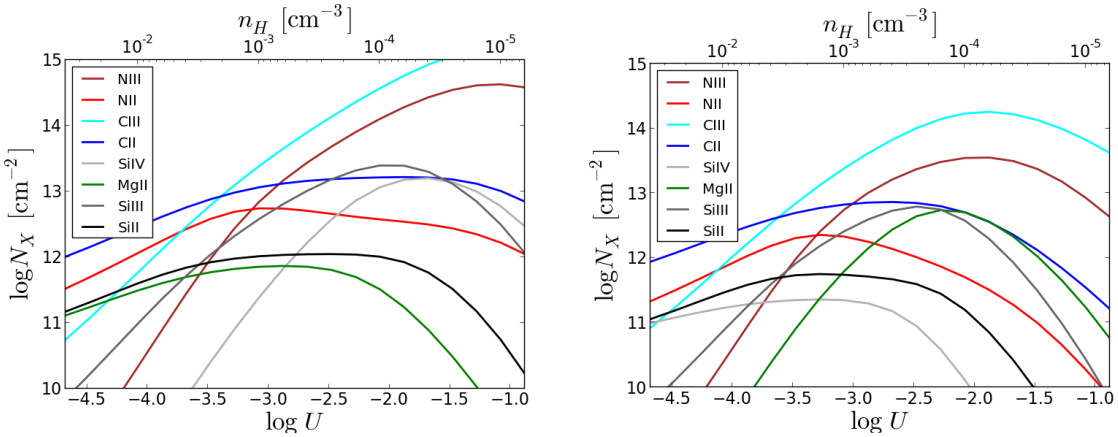

Figure 2.8: Left panel, column densities as a function of the ionization parameter and the intrinsic number density, calculated with CLOUDY assuming the ionizing flux of Haardt & Madau (2001) and the default solar abundances of CLOUDY. Right panel, same CLOUDY outputs, calculated this time assuming the ionizing flux of Haardt & Madau (2012) and the solar abundances from Asplund et al. (2009).

The right panel of Figure 2.8 instead shows how the results change using the UV background radiation field from Haardt & Madau (2012), (see Figure 2.9). The comparison of these last results with the one plotted in Figure 2.7 shows that there are significant differences in the predicted column densities, only due to the different form of the ionizing background field. Werk et al. (2014) estimated these uncertainities to be ± 0.3 dex, on average.

We conclude this investigation by describing what we consider to be potentially the most problematic assumption in the CLOUDY modelling performed by Werk et al. (2014), i.e. to consider the CGM as a uniform slab, instead of composed by a variety of clouds (assumption 4). For each line-of-sight, the different kinematic components, observed with the fitting of the Voigt profiles (see Section 2.1.2) indicate that the ion absorptions arise from different absorbers (Werk et al. 2013). Therefore, it could be not fair to perform the CLOUDY analysis using all the ions of one line-of-sight together. Different clouds of the same sightline could have different ionization parameters and a more thorough analysis may lead to different results. One of our future plans will be to perform this photo-ionization modelling on each kinematic component. However, this is outside the scope of this Thesis and in the following chapters we consider valid the results of Werk et al. (2014), even though they are affected by large uncertainties.

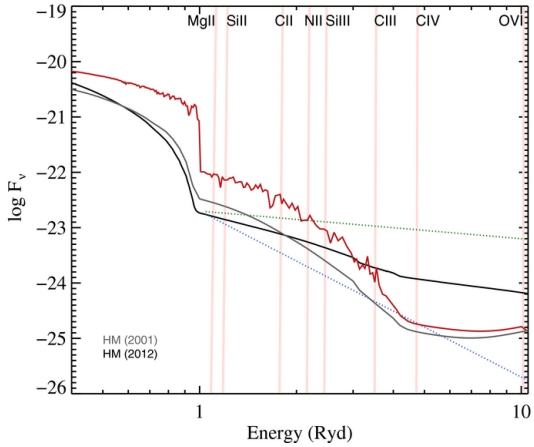

Figure 2.9: Comparison between the UV background fluxes from Haardt & Madau (2001), shown as the grey line, and from Haardt & Madau (2012), shown as the black line. The red line shows the Haardt & Madau (2001) background flux with the addition of the SED from the galaxy Starburst99 (from Werk et al., 2014).

2.3 Early-type galaxies

Here we describe in more detail the COS-Halos data for the ETGs, which are the focus of this Thesis. 16 out of 44 galaxies in the whole sample are early-type ($sSFR < 10^{-11}\mathrm{yr}^{-1}$). They differ from the star-forming subsample both in stellar mass and virial radius, as shown in Figure 2.10. The galaxy stellar mass is determined by *kcorrect* (Blanton et al., 2003) from the SDSS *ugriz* photometry, while the virial masses are estimated using abundance matching. In particular, they are calculated using the relation of Moster et al. (2010):

$$\frac{M_*(M_{\rm vir})}{M_{\rm vir}} = 2\left(\frac{M_*}{M_{\rm vir}}\right)_0 \left[\left(\frac{M_{\rm vir}}{M_1}\right)^{-\beta} + \left(\frac{M_{\rm vir}}{M_1}\right)^{\gamma}\right]^{-1} , \tag{2.3}$$

where $\beta = 1.057$, $\gamma = 0.556$, $M_1 = 10^{11.884}\ M_\odot$ and $(M_*/M_{\rm vir})_0 = 0.02820$. Systematic errors in the stellar mass estimates and the scatter and uncertainty in the $M_{\rm vir} - M_*$ relation gives an uncertainty on the virial masses of the 50%. Finally, the virial radii are calculated through the equation:

$$r_{\rm vir} = (3M_{\rm vir}/\Delta_{\rm vir}\rho_{\rm crit}4\pi)^{\frac{1}{3}} , \tag{2.4}$$

where $\rho_{\rm crit}$ is the cosmic critical density at the spectroscopically determined redshift of the galaxy and $\Delta_{\rm vir} = 200$. The distributions of the two types of galaxies are clearly different (see Figure 2.10). ETGs tend to have larger stellar masses and virial radii. A

Kolmogorov-Smirnov (K-S) test between the two subsamples[2] returned $p_{\rm val} = 5 \times 10^{-6}$, which confirms that the two samples differ significantly.

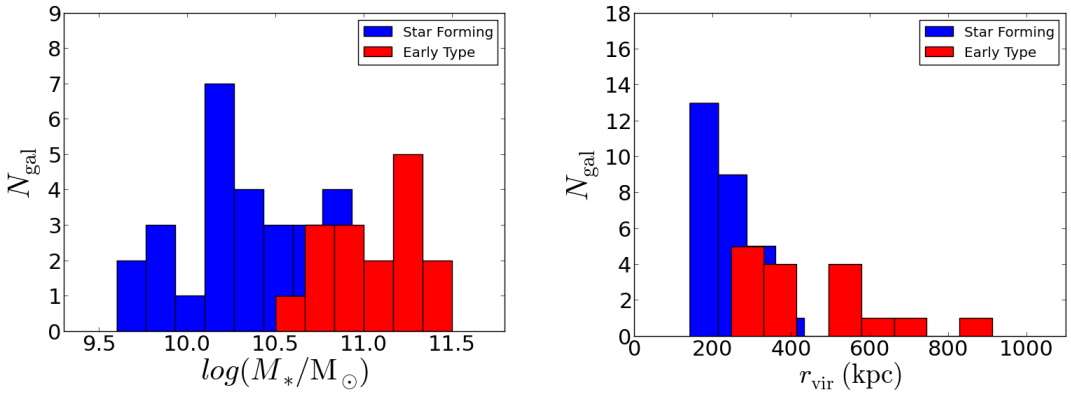

Figure 2.10: COS-Halos galaxy distributions: left, as a function of the stellar mass; right, as a function of the virial radius. star forming galaxies are represented with blue bars, ETGs with red bars.

SDSS Field	Galaxy ID	z	SFR ($M_\odot\ yr^{-1}$)	R_c (kpc)	R_{vir} (kpc)	log ($M_*/M_\odot$)	log ($M_{vir}/M_\odot$)
J0226+0015	268_22	0.23	<0.09	80	303	10.8	12.4
J0803+4332	306_20	0.25	<0.21	77	581	11.3	13.4
J0910+1014	242_34	0.26	<0.30	139	716	11.5	13.8
J0925+4004	196_22	0.25	<0.57	83	569	11.3	13.4
J0928+6025	110_35	0.15	<0.04	93	317	10.8	12.4
J0943+0531	216_61	0.14	<0.03	152	382	11.0	12.8
J0950+4831	177_27	0.21	<0.30	93	511	11.2	13.2
J1133+0327	110_5	0.24	<0.29	17	515	11.2	13.2
J1157–0022	230_7	0.16	<0.09	19	334	10.9	12.6
J1220+3853	225_38	0.27	<0.13	156	279	10.8	12.4
J1550+4001	197_23	0.31	<0.16	106	578	11.4	13.6
J2345–0059	356_12	0.25	<0.14	47	304	10.9	12.6

Table 2.1: List of the main properties of the twelve early-type galaxies on which we focus in our work.

In Table 2.1 we list the 12 galaxies of our sample. We report the SDSS field identifier

[2]We performed a K-S test only for the stellar masses, given the relation between the stellar masses and the virial radii (equations 2.3 and 2.4).

of the backround quasar, the galaxy identifier, the galaxy redshift, the estimated upper limits for SFR, the projected distance between the sightline and the centre of the galaxy (impact parameter), the virial radius, the stellar mass and the virial mass. We excluded from our sample the 4 galaxies for which hydrogen lines were detected (see Section 2.1).
COS-Halos data for early-type galaxies provide two fundamental observational constraints on which we focus in the rest of this Thesis: the total hydrogen column densities and the velocity distribution of the absorbers. The goal of our models is to reproduce these observed properties of the circumgalactic medium in ETGs.
The first important constraint given by the observations is the total hydrogen column density, N_H, estimated using the method of Section 2.2. In particular, as we see in Chapter 4 and 5, we aim to reproduce its flat slope with radius. In Figure 2.11 we show the data obtained for our selected subsample of ETGs. For three galaxies the absence of the metal absorptions has prevented the estimate of the ionization parameter, thus we use column density data only for the other nine galaxies. The error bars are computed taking into account the range of ionization parameters allowed using the CLOUDY procedure (see again 2.2) and the uncertainties in the observed neutral hydrogen column densities.

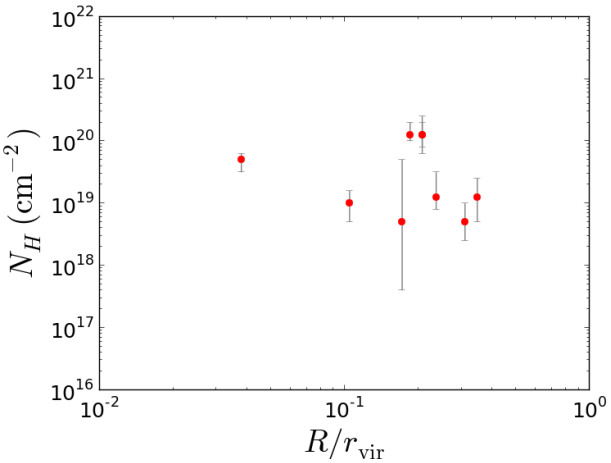

Figure 2.11: Total hydrogen column densities found by COS-Halos for the ETGs, with the associated errors, as a function of the (normalized) impact parameter. The distribution appears rather flat with radius.

The second important constraint given by the COS-Halos data is the distribution of the observed velocities of the CGM clouds. Along each line of sight, we observe for every species multiple components with different velocities (see Figure 2.3). To decide which components arise from the same clouds, we use the spectral resolution of COS

(15 km s^{-1}). We consider two velocities yelded by two different clouds if they differ by more than the COS resoltion. The resulting velocity distribution, where we report the velocities of every clouds, is shown in the left panel of Figure 2.12. The dispersion of this distribution, i.e. its standard deviation, is:

$$\sigma_{\rm obs} = 153 \text{ km s}^{-1} \ . \tag{2.5}$$

In Chapter 4 we consider that the CGM clouds are moving in the halos of ETGs with a velocity dispersion that reproduces this observed value. In Chapter 5 we explore infall patterns for the clouds keeping this observed distribution as kinematic constraints.
To associate an error on this value, we used the bootstrapping method. We randomly created 1000 velocity distributions with the same total number of velocities of the distribution in Figure 2.12 (left) and taking its elements, but randomly replacing them. Therefore all the distributions are different, depending on the (random) number of replacements of every elements. Then we calculated the standard deviations of all the distributions thus created, obtaining the histogram in the right panel of Figure 2.12. Finally we adopted the standard deviation of this distribution as an estimate of the error on $\sigma_{\rm obs}$. We find that this error is:

$$\delta_\sigma = 16 \text{ km s}^{-1} \ . \tag{2.6}$$

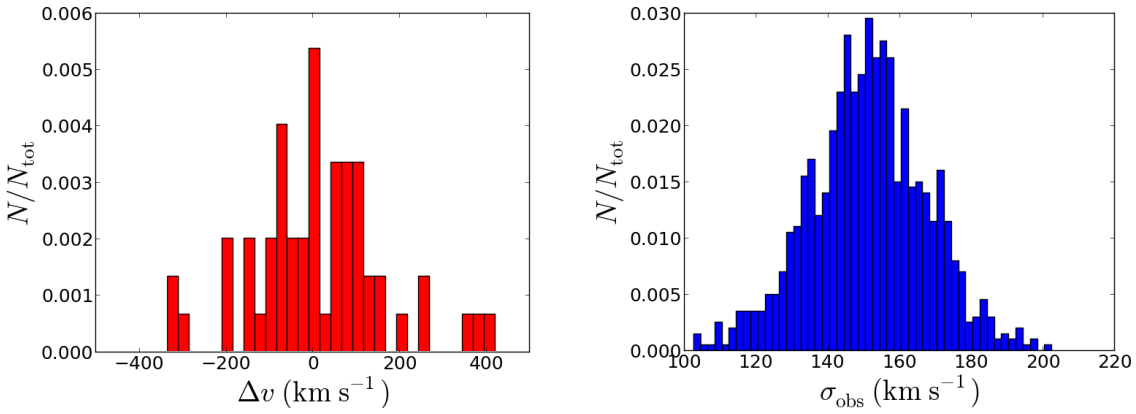

Figure 2.12: Left, observed velocity distribution of the CGM clouds in COS-Halos early-type galaxies. Right, distribution of the standard deviations of every distributions calculated with the bootstrapping method.

2.3.1 Halo model

In order to model the kinematics of the CGM clouds in COS-Halos early-type galaxies, it is necessary to estimate the gravitational potential of these galaxies. First, using Table 2.1 we found the mean values of the virial mass and the virial radius of the twelve galaxies of our sample: $M_{\rm vir} = 10^{13.2}$ M$_\odot$ and $r_{\rm vir} = 451$ kpc. Then, we assumed for the dark matter halo a NFW mass profile (Navarro et al., 1995):

$$M(r) = 4\pi\rho_0 r_s^3 \left[\ln(1 + r/r_s) - \frac{r/r_s}{1 + r/r_s}\right] , \tag{2.7}$$

Where ρ_0 is the normalization of the profile and r_s is the scale radius of the system. This mass profile leads to the following gravitational potential:

$$\Phi(r) = -G \int_r^\infty \frac{M(r)}{r^2}\, dr = -4\pi\rho_0 r_s^2\, \frac{\ln(1 + r/r_s)}{r/r_s} . \tag{2.8}$$

We used a concentration $C = r_{\rm vir}/r_s = 13$ (the same used in Werk et al. 2014). Taking into account that:

$$M_{\rm vir} = 4\pi\rho_0 r_s^3 \left[\ln(1 + r_{\rm vir}/r_s) - \frac{r_{\rm vir}/r_s}{1 + r_{\rm vir}/r_s}\right] , \tag{2.9}$$

we obtain $\rho_0 = 1.2 \times 10^{-24}$ g cm^{-3}.
In the rest of this Thesis, we will adopt the potential described above as an estimate of the typical gravitational potential associated to the ETGs in our sample. Finally, we estimated the expected line-of-sight radial velocity dispersion of these early-type galaxies using the virial speed of this model. This leads to:

$$\sigma_r = \frac{\sqrt{GM_{\rm vir}/r_{\rm vir}}}{\sqrt{3}} \simeq 230 \text{ km s}^{-1} , \tag{2.10}$$

which is 1.5 times larger than the observed velocity dispersion $\sigma_{\rm obs}$. The discrepancy between the expected and the observed value is larger than 3 times the estimated error δ_σ on the observations. Understanding this discrepancy will be one of the main goals of our analysis in the following chapters.

Chapter 3

Physical state of CGM clouds in ETGs

In this Chapter we investigate the physical state of the CGM clouds in our ETG sample (see Section 2.3). In Section 3.1 we make an analaysis of the Jeans mass of a CGM cloud, while in Section 3.2 we investigate the pressure equilibrium with the hot corona and we make a comparison between the typical timescales of the system. In Section 3.3 we show a more detailed analysis, based on the results of a set of hydrodynamical simulations and finally in Section 3.4 we outline our conclusions.

3.1 Jeans mass

If the CGM clouds are self-gravitating, there will be little influence of the external medium (the hot corona) on their motion. In order to assess this scenario, we consider the Jeans mass:

$$M_{\rm J} = \frac{\pi^{3/2} c_{\rm s}^3}{\rho_{\rm cl}^{1/2} G^{3/2}} \ , \tag{3.1}$$

where $c_{\rm s}$ is the speed of sound, defined as:

$$c_{\rm s} = \sqrt{\frac{k_{\rm B} T_{\rm cl}}{\mu m_{\rm p}}} \ , \tag{3.2}$$

where for $T_{\rm cl}$ we assumed the same value of 2×10^4 K, used in Werk et al. (2014), while $\mu = 0.67$ is the mean molecular weight derived from Sutherland and Dopita (1993) for a gas in collisional ionization equilibrium at the assumed temperature. Finally, $\rho_{\rm cl} = 1.4 m_p n_H$, where the factor of 1.4 accounts for the presence of helium, as in Werk et al. (2014). In the left panel of Figure 3.1 we show the hydrogen volume densities of our sample of early-type galaxies, found by Werk et al. (2014) using the procedure described in Chapter 2 (equation (2.1)), plotted as a function of normalized projected radius. By inserting in equation (3.1) the mean value of these volume densities, $n_H \sim$

7×10^{-4} cm^{-3}, we obtain $M_{\rm J} = 1.5 \times 10^{10}$ M$_\odot$, which is marked as a horizontal line in the right-hand panel of Figure 3.1. To establish whether a cloud is self-gravitating, we compare the Jeans mass obtained above with the mass of a typical CGM cloud, calculated as:

$$M_{\rm cl} = \frac{4}{3}\pi\rho_{\rm cl}R_{\rm cl}^3 \ , \tag{3.3}$$

using the average observed density, as above. The blue line in the right panel of Figure 3.1 shows the mass of a cloud as a function of its size $R_{\rm cl}$, exploring a wide range of radii, becase of the high observational uncertainties (see Section 2.2).

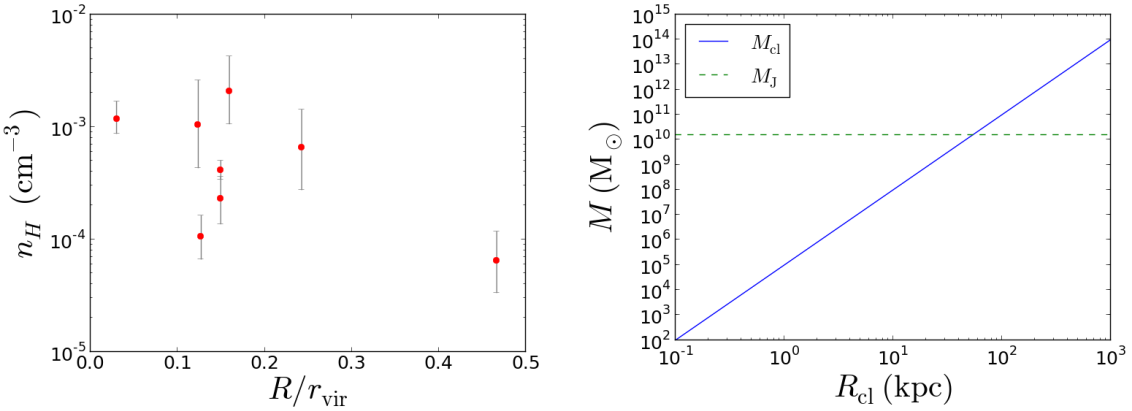

Figure 3.1: Left panel, intrinsic densities of the CGM in early-type galaxies, observed by Werk et al. (2014). Right panel, comparison between the Jeans and the clouds mass, expressed as a function of the clouds radius.

The comparison between the two masses in the right panel of Figure 3.1 shows that the mass of the cloud becomes larger than the Jeans mass only for $R_{\rm cl} \gtrsim 50$ kpc, which is unrealistically large for a CGM cloud. This analysis leads us to conclude that the CGM absorbers cannot be supported by their own gravity.

3.2 Pressure equilibrium

In the previous section we have shown that the cold CGM clouds are not self-gravitating, therefore to understand their physical state we have to taking into account also their interactions with the hot external medium. Werk et al. (2014) found that the densities of the cold gas predicted by the pressure equilibrium with a hot corona of a Milky-Way galaxy are two orders of magnitude higher than observations. Therefore, they conclude that this gas cannot be in pressure equilibrium with the hot corona and that the CGM clouds are transient phenomena that cannot survive for a long time in galaxy halos.

To be more thorough, here we calculate the cold gas density using the condition of pressure equilibrium with a hot corona consistent with our halo model (Section 2.3.1). In massive early-type galaxies we observe hot gas halos with high temperatures ($T_{\rm cor} \sim 10^7$ K) nearly constant with the radius (e.g. Finoguenov and Jones, 2000; Humphrey et al., 2011). We can describe the corona as an isothermal gas in hydrostatic equilibrium in the gravitational potential of the dark matter:

$$n_{\rm e,cor}(r) = n_{\rm e,0} \exp\left[-\frac{\mu m_{\rm p}}{k T_{\rm cor}}(\Phi(r) - \Phi_0)\right] \ , \tag{3.4}$$

where we used $T_{\rm cor} = 10^7$ K and $\mu = 0.58$, obtained again from Sutherland and Dopita (1993) for a gas in collisional ionization equilibrium at this temperature, while the normalization factor $n_{\rm e,0}$ is found by requiring the coronal mass to be a given fraction of the theoretical baryonic content of the halo. We assume a NFW potential, as described in Section 2.3.1. The theoretical baryonic mass is $M_{\rm bar} = 0.155 M_{\rm vir}$, corresponding to the cosmological baryonic mass fraction (Planck Collaboration et al., 2016). We adopted the virial mass of our model, found in Section 2.3.1: $M_{\rm vir} = 10^{13.2}\ M_\odot$. We assumed a mass for the hot gas equal to the 10% of the theoretical baryonic mass, in broad agreement with observational estimates (e.g. Anderson and Bregman, 2011; Bogdán et al., 2013). The resulting coronal density profile is shown as a red dashed-curve in Figure 3.2.

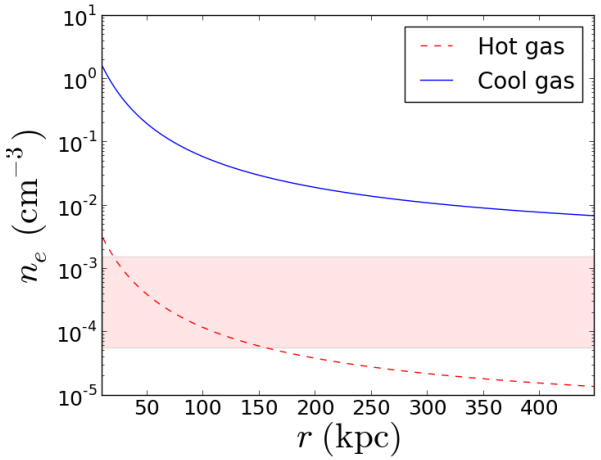

Figure 3.2: The red dashed-curve represents the density profile of the coronal hot gas, described by equation (3.4). The density profile of the cold gas, described by equation (3.5), is instead shown by the blue curve. The horizontal band shows the median value of the observations.

The density of the cold CGM under the assumption of pressure equilibrium with the

hot gas can be found through the equation:

$$n_{\mathrm{e,cl}}(r) = \frac{n_{\mathrm{e,cor}}(r) T_{\mathrm{cor}}}{T_{\mathrm{cl}}} \ , \tag{3.5}$$

and is shown in Figure 3.2 as a blue curve.
We have seen, in the left panel of Figure 3.1 the values of the intrinsic hydrogen densities found by Werk et al. (2014) for ETGs. To compare these values with the observations, we multiply them by 1.16 (as in Werk et al., 2014), to obtain the electron densities. The horizontal band in Figure 3.2 shows the mean observed value $\bar{n}_e$, with its standard deviation. The comparison between the blue theoretical line for the cold CGM densities and the observations shows that the difference is significant, larger than two orders of magnitude in the inner regions. Thus, as found by Werk et al. (2014), the CGM clouds cannot be, using a realistic corona for this kind of galaxies, in pressure equilibrium with the hot gas.
Note however that in the outer regions (beyond $\sim$ 300 kpc), the discrepancy between our pressure-equilibrium densities and observations can be less than one order of magnitude, which, as we have seen in Section 2.2, might be ascribed to uncertainties in photoionization modeling. Moreover, the uncertainties in the observations could be even larger than that, due to the approximation of the CGM as an uniform slab, as explained at the end of Section 2.2. Therefore, if we assume that the clouds that we are observing are confined to the external regions of the halo (which is possible, because the observations give informations only on the projected distances), then the density predicted by pressure equilibrium can be compatible with COS-Halos observations.

3.2.1 Analysis of the Jeans mass

In this section we assume pressure equilibrium and we recalculate the Jeans mass of the CGM through equation (3.1), using the densities inferred from equation (3.5). Figure 3.3 shows that with the pressure-equilibrium assumption the Jeans mass becomes a function of the galactocentric radius. For each radius the Jeans mass is larger than 10^8 $\mathrm{M}_\odot$. This is very large, compared to plausible masses of the absorbers, therefore we conclude that the gravity of the clouds is negligible and we cannot treat them as self-gravitating, even if they have the densities obtained with the pressure equilibrium with the the hot corona.

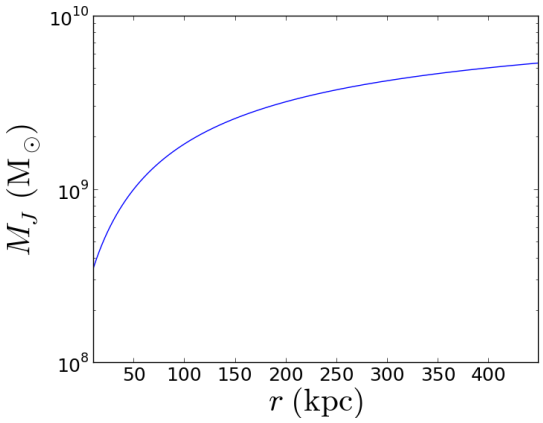

Figure 3.3: Jeans mass of the clouds, calculating here with the assumption of the pressure equilibrium, as a function of the galactocentric radius.

3.2.2 Analysis of the timescales

We make here a comparison of the different relevant timescales for the system: the *drag time*, which is useful to understand the influence of the hot gas on the cloud motion, and two different dynamical times, the *crossing time* and the *free-fall time*.
In our analysis, we assume that all the CGM clouds have the same mass. Then, fixed the mass of the clouds, we can calculate the radii of the clouds from the densities inferred by imposing the pressure equilibrium with the corona. Under these conditions the radius of the clouds is a function of the galactocentric radius, and it is expressed by:

$$R_{\rm cl}(r) = \left(\frac{3M_{\rm cl}}{4\pi\rho_{\rm cl}(r)}\right)^{\frac{1}{3}} . \tag{3.6}$$

In Figure 3.4 we show the radial profile of this radius for three different cloud masses: $M_{\rm cl} = 10^5, 10^6, 10^7$ $M_\odot$. This figure shows that the radius of the clouds increases with galactocentric radius and can reach values larger than 2 kpc in the external regions. In the outer regions in fact, the density of the clouds is lower than in the inner one and therefore they have to be larger to obtain the same mass. With the pressure-equilibrium assumption, the clouds shrink or expand while moving in the hot corona.
Let us now consider the influence of the hot gas on the clouds while they are moving through the galaxy halos, to understand whether the drag force acted by the corona can radically change the motion of the CGM clouds. To estimate the interactions between the hot gas and the CGM clouds, a fundamental quantity is the drag time of a cloud, which is:

$$t_{\rm drag}(r) = \frac{M_{\rm cl}}{v\pi R_{\rm cl}^2(r)\rho_{\rm cor}(r)} , \tag{3.7}$$

where v is the cloud velocity relative to the hot gas, and $\rho_{\rm cor} = (n_{\rm e,cor}/0.52)\mu$[1]. This time give an estimate of the timescale in which the hot gas dramatically influences the cloud motion. After one drag-time, the interactions between the cold clouds and the hot corona cannot be neglected. We calculate this quantity using as a typical velocity the observed velocity dispersion of 153 km s^{-1} and the same three masses mentioned above. The resulting profiles are plotted in the left panel of Figure 3.5.

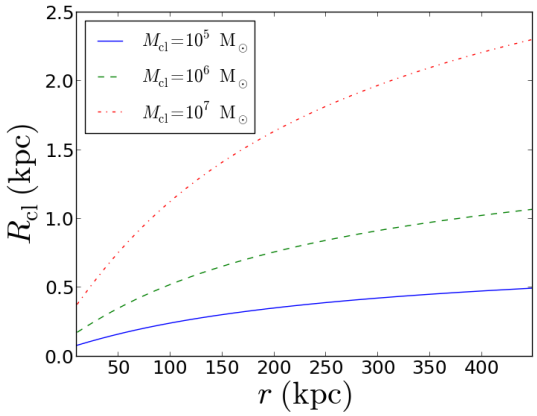

Figure 3.4: Radial profiles of the cloud radius as functions of the galactocentric radius, with three different assumptions fot the cloud mass: $M_{\rm cl} = 10^5, 10^6, 10^7$ M$_\odot$.

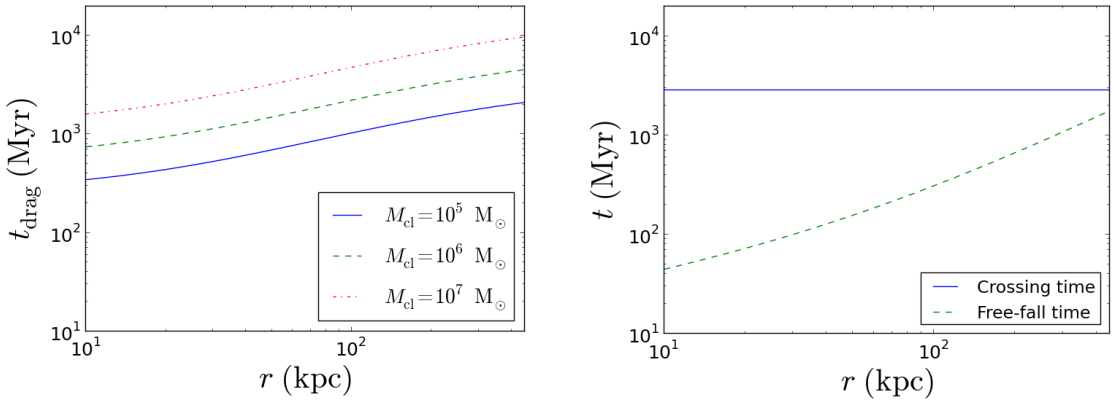

Figure 3.5: Left, radial profiles of the drag time as functions of the galactocentric radius, with three different assumptions fot the cloud mass: $M_{\rm cl} = 10^5, 10^6, 10^7$ M$_\odot$. Right, profiles of the free fall time (green line) and the crossing time (blue line) as functions of the galactocentric radius.

The drag time increases with the cloud mass, as shown in the left panel of Figure 3.5.

[1]Here $\mu = 0.58$ and $n = 0.52 n_e$.

Therefore, more massive clouds are less affected by the interactions with the hot corona. For very massive absorbers ($M_{\rm cl} = 10^7$ M$_\odot$), the drag time is about 10 Gyr at galactocentric radii close to the virial radius of the model (red line in the right panel of Figure 3.5). In general, in the external regions, at ~ 300 kpc, $t_{\rm drag} \gtrsim 2$ Gyr.
To estimate the influence of the coronal gas on the motion of the clouds, we have however to compare the drag time with the dynamical time of the system. We define two different dynamical times for this system, the free-fall time and the crossing time, and we compare them to the drag time. The free-fall time is the time that a particle needs, under the influence of the gravitational potential of the system, to reach the centre of the galaxy and it is defined as (Binney et al., 2009):

$$t_{\rm ff} = \frac{\pi}{2} \frac{r^{3/2}}{\sqrt{GM(r)}} \ , \tag{3.8}$$

where $M(r)$ is the dynamical mass profile of the system, described in Section 2.3.1.
The crossing time is instead defined as:

$$t_{\rm cross} = \frac{r_{\rm vir}}{v} \ , \tag{3.9}$$

and it is the time that a cloud needs to cross the system (from $r = r_{\rm vir}$, to $r = 0$) with its typical velocity v (we use here 153 km s^{-1}). We show these two timescales in the right panel of Figure 3.5.
The comparison between the two panels of Figure 3.5 shows that, while the free-fall time is generally shorter, the crossing time has a value comparable to the drag-time. In particular, the drag time is larger than $t_{\rm cross}$ for clouds with high masses and in the external regions, where the hot corona is more diffuse and the clouds larger.
This analysis leads us to conclude that, if the CGM clouds have high masses ($\gtrsim 10^6$ M$_\odot$) and our assumptions on the pressure equilibrium and the coronal mass are valid, in the external regions of the halos the hot gas has a small influence on the motion of the clouds. Therefore, at least in these regions, it could be fair to treat the CGM absorbers as collisionless. Generally, $t_{\rm cross} \sim t_{\rm drag}$, thus the condition of weak interactions with the hot gas is marginally satisfied. In the following sections we explore the drag effects of the corona on the CGM, focusing on the differences between the internal and the external regions of the halos, where there are different values of the drag time, even for clouds of the same masses, as shown in Figure 3.5 (left).

3.3 Numerical simulations

In order to have a more clear understanding of the physical state of the CGM clouds, we show in this section the results obtained from a set of hydrodynamical simulations. We are interested in the behaviour of cold clouds in the halos of galaxies, in particular

in their interactions with the hot corona. The aim of this study is to investigate the conditions for the survival of cold CGM clouds to the interaction with the hot corona. We will compare numerical results with the simple analytical estimates of the previous section, which suggested that, if the CGM clouds are massive enough, the interactions with the corona are weak in the external regions, while they are stronger at low galactocentric radii, where the clouds are smaller and the hot gas denser.
To perform the simulations we use *ATHENA* (Stone et al., 2008), a grid based, parallel and multidimensional hydrodynamic code, which integrates numerically the Euler equations. In the next sections, we briefly describe the main chacarchteristics of this hydrodynamical code (Section 3.3.1), we outline the setup of our simulations (Section 3.3.2) and we show our results (Section 3.3.3).

3.3.1 The ATHENA code

Here we briefly summarize how the numerical code which we used for our simulations works. This is only a brief overview of the equations solved by ATHENA and not a complete description of the code. An exhaustive characterization of ATHENA can be found in Stone et al. (2008). The code implements algorithms that are built on high-order Godunov methods (Godunov, 1959), based on conservative finite-volume discretization, to integrate numerically the Euler equations.

Solution of the Euler equations

The Euler equations are commonly used to describe collisional gas systems and consist of a set of conservation laws (conservation of mass, momentum and energy), which can be written as:

$$\frac{\partial \rho}{\partial t} + \nabla \cdot (\rho \mathbf{v}) = 0 \tag{3.10}$$

$$\frac{\partial \rho \mathbf{v}}{\partial t} + \nabla \cdot (\rho \mathbf{v} \otimes \mathbf{v} + \mathbf{P}) = 0 \tag{3.11}$$

$$\frac{\partial e}{\partial t} + \nabla \cdot [(e + P)\mathbf{v}] = 0 \tag{3.12}$$

where ρ is the mass density, $\mathbf{v}$ the velocity vector, $\mathbf{P}$ is a diagonal tensor with components equal to the gas pressure P and e the total gas energy per unit volume. Equation (3.12) changes with the implementation of radiative cooling and heating. (see next section). In the case of an ideal fluid it is possible to express the volumetric total energy as the sum of the volumetric internal and kinetic energies:

$$e = \frac{P}{\gamma - 1} + \frac{1}{2}\rho ||\mathbf{v}||^2 \ , \tag{3.13}$$

where γ is the adiabatic index assumed to be 5/3 in this analysis.
The ATHENA code integrates these equations on a regular, three-dimensional Cartesian grid. It works by integrating the system (3.10) – (3.12) over the finite volume of each grid cell and over a discrete time-step Δt, after application of the divergence theorem. The maximum stable allowed time-step Δt is fixed by the *CFL* (Courant-Friedrics-Lewy) condition as explained and defined in Stone et al. (2008).

Radiative cooling and heating

Radiative cooling and heating are added as source term in equation (3.12):

$$\frac{\partial e}{\partial t} + \nabla \cdot [(e + P)\mathbf{v}] = \rho^2 \Lambda_{net}(T, Z, n_H) \ , \tag{3.14}$$

where $\rho^2 \Lambda_{net}$ is the net rate of energy lost by the gas per unit volume [erg cm^{-3} s^{-1}] due to radiative processes, and Λ_{net} is the net cooling rate normalized to the square of the total gas density [erg cm^3 s^{-1}]. $\Lambda_{net} = \Lambda - H$, where Λ and H are, respectively, the gas cooling and heating rates. In the presence of the cooling term, to avoid possible problems in regions where the radiative cooling is very effective, the time step is a fraction of the cooling time, defined as:

$$t_{\rm cool} = \frac{P}{(\gamma - 1)\rho^2 \Lambda_{net}(T, Z, n_H)} \tag{3.15}$$

In our simulations we assume the collisional ionization equilibrium (CIE): the gas is optically thin and external radiation fields that may affect the ionisation balance are absent. Then, the radiative heating is null ($H = 0$) and $\Lambda_{net}(T, Z, n_H) = \Lambda(T, Z)$, called cooling function, which only depends on the temperature T and the metallicity Z of the gas. We used in particular the cooling function from Sutherland & Dopita (1993). Also thermal conduction is not implemented in our simulations.

3.3.2 Simulations setup

We performed a set of 2-D simulations that model a cold and metal-rich cloud that travels through a hot, uniform and static coronal gas with a given initial velocity, as in Marinacci et al. (2010, 2011) and Armillotta et al. (2016). In particular we change the densities of the hot gas and of the cold cloud (related each other by the pressure equilibrium) and the radius of the cloud, in order to explore the behaviour of clouds with different masses and moving at different galcocentric radii, where the corona and the cold gas have different conditions (see Section 3.2). For the hot gas, we assume $T = 10^7$ K and different densities, associated to inner or outer regions of a halo, as explained in Section 3.2, while for CGM clouds we consider $T = 2 \times 10^4$ K and two

different masses ($\sim 10^6$ $M_\odot$, $\sim 10^5$ $M_\odot$). To infer the densities of the hot and the cold gas, and the radii of the clouds, we use the plots in Figures 3.2 and 3.4. The metallicity of the hot gas is $0.1Z_\odot$, while the cold gas has $Z = 0.3Z_\odot$ in all simulations. The initial velocity of the cloud is always 150 km s^{-1} along the x-axis, in agreement with the observed value (see equation (2.5)), while it is null along the y-axis. All the simulations have a grid resolution of 8 pc and run for 100 Myr. The parameters of all simulations are listed in Table 3.1.

Sim.	$M_{\rm cl}$ ($M_\odot$)	n_{cor} (cm^{-3})	n_{cl} (cm^{-3})	R_{cl} (kpc)	x_{grid} (kpc)	y_{grid} (kpc)	Cooling
1	7×10^5	2×10^{-5}	0.01	1	20	6	ON
2	7×10^5	2×10^{-5}	0.01	1	20	6	OFF
3	8×10^4	2×10^{-5}	0.01	0.5	18	5	ON
4	7×10^5	3×10^{-3}	1.35	0.2	15	4	ON
5	7×10^5	3×10^{-3}	1.35	0.2	15	4	OFF
6	8×10^4	3×10^{-3}	1.35	0.1	15	4	ON

Table 3.1: List of the parameters of the performed simulations. Simulations 1, 2 and 3 are representative of the external regions, while simulations 4, 5 and 6 are representative of the internal regions. We varied the cloud mass from $\sim 10^6$ $M_\odot$ (simulations 1, 2, 4 and 5), to $\sim 10^5$ $M_\odot$ (simulations 3 and 6). The density of the cold cloud is defined by the pressure equilibrium with a hot corona with the density described by equation (3.4). In simulations 2 and 5 the radiative cooling is not implemented.

3.3.3 Results

We divide the results of the simulations in two main groups: the external (simulations 1, 2 and 3, which simulate a cold cloud moving at ~ 300 kpc from the galaxy centre) and the internal (simulations 4, 5 and 6, which simulate a cold cloud moving at ~ 10 kpc from the galaxy centre) regions of the galaxies halos. We are interested in fact in the behaviour of the clouds in these two different environments.

External regions

In Figures 3.6 and 3.7 we show the result obtained with simulations 1 and 2, which model the motion of a cloud with $M \sim 10^6$ $M_\odot$ in the external regions of our ETGs halos. In the first simulation we also implement the radiative cooling, while it is absent in the second, to make a comparison.

The left and right panels of Figure 3.6 show respectively the evolution with time of the cold ($T < 10^5$ K) mass and of the cloud velocity. The time evolution of the mass of cold gas is a tracer of the survival or desruption of the cold CGM cloud as a consequence of its interaction with the hot corona. We show also the analytic prediction for the velocity of a cloud subject to drag, calculated using the equation (Marinacci et al., 2011):

$$v(t) = \frac{v_0}{1 + t/t_{\rm drag}} \ , \tag{3.16}$$

where v_0 is the initial velocity of the cloud and $t_{\rm drag}$ is the drag time (equation (3.7)). Both the evolutions of the cold mass and the velocity are nearly constant with time and the behaviours with or without cooling are quite similar. Therefore, it seems that the influence of the coronal gas on clouds with this mass is small.

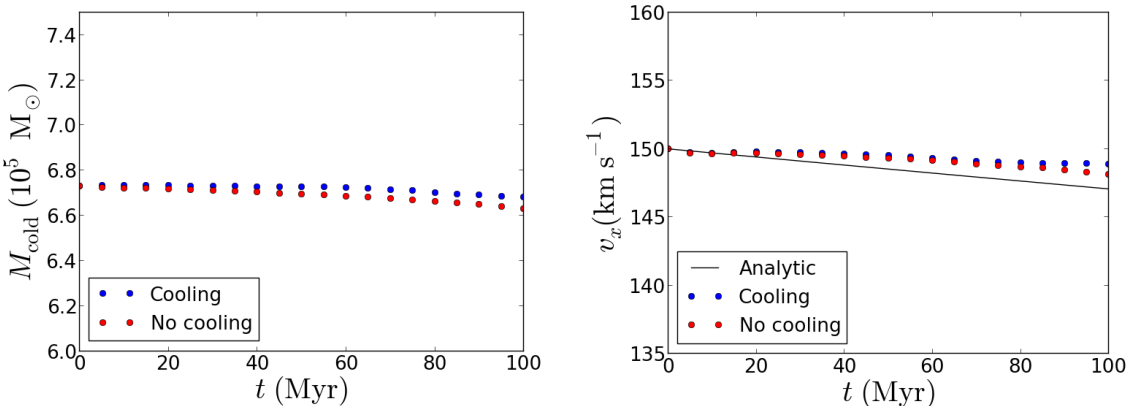

Figure 3.6: Results of simulations 1 (with cooling, blue points) and 2 (without cooling, red points) Evolutions with time of the cold gas mass (left) and of the velocity (right), for a cloud with $M_{\rm cl} \sim 10^6$ M$_\odot$ moving at large galactocentric distances. The black line in the right panel shows the analytic prediction for the velocity.

Figure 3.7 shows instead the temperature maps of the simulations.
The first and the second panels of Figure 3.7 show two snapshots at 20 and 100 Myr for the first simulations (with radiative cooling), while the third and the the fourth panels show the same snapshots for the second simulation (without cooling). The difference between the two simulations is that the first two panels show that the cloud becomes smaller with time. This is due to the radiative cooling, because the decrease of the temperature leads the clouds to become smaller, in order to increase its density and mantain the pressure equilibrium with the hot gas. This effect is not present in the simulation without cooling. However, in both cases the maps show that, after 100 Myr, the clouds are not destroyed by the hot gas. Almost all the cold gas remains within the cloud and is not stripped by the hot gas, as shown by the white contours at $T = 10^5$ K.

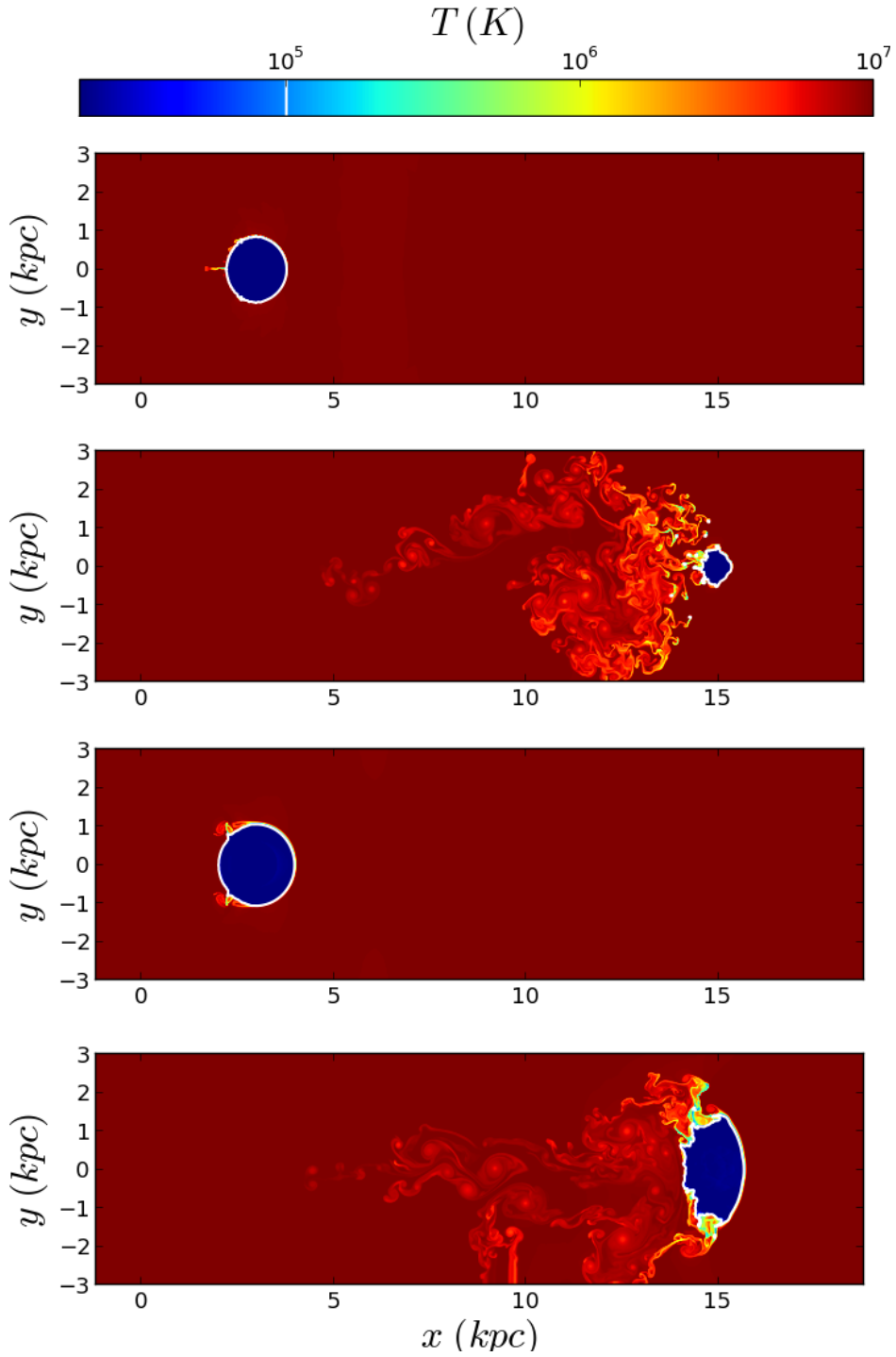

Figure 3.7: First and second panels: temperature maps of simulation 1 respectively after 20 and 100 Myr. Third and fourth panels: temperature maps of simulation 2 respectively after 20 and 100 Myr. The white contours are located in all snapshots at $T = 10^5$ K.

In Figures 3.8 and 3.9 instead, we report the results of the third simulation, which simulates a cloud with $M \sim 10^5\ M_\odot$, with the radiative cooling implemented. The evolutions of the cold gas mass and of the cloud velocity are similar to the previous one: apart from a somewhat shallower decrease with time of the two quantities, there is no significant difference with the results obtained for the more massive cloud.

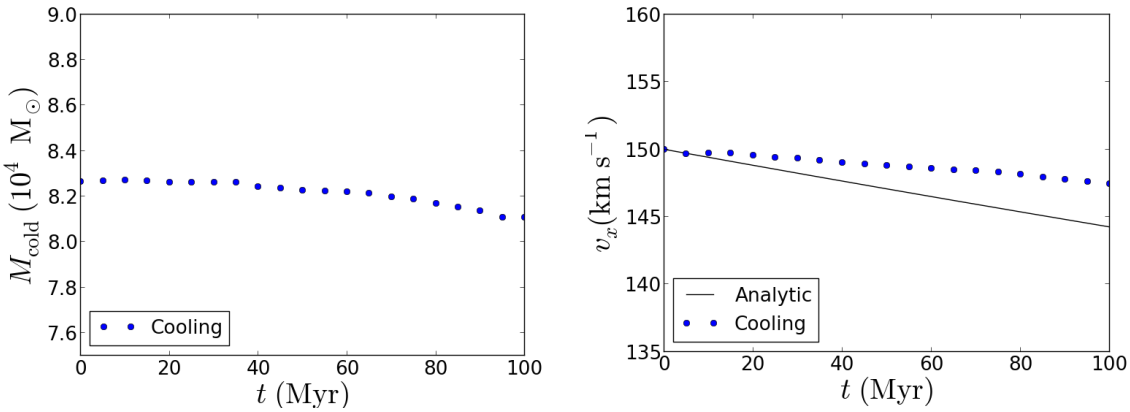

Figure 3.8: Similar to Figure 3.6, but for simulation 3, with a smaller mass of the cloud ($M_{\rm cl} \sim 10^5$ M$_\odot$), and including the effects of cooling.

However, the temperature maps in Figure 3.9 show that in this case the interactions with the hot corona are stronger that in the previous case. In fact, in the last snapshot, at 100 Myr, a significant fraction of the cold gas has been stripped from the cloud by the hot gas, due to Kelvin-Helmholtz instabilities. Therefore, the motion of this cloud cannot be treated as collisionless, because the interactions with the corona are not negligible.

Internal regions

With simulations 4, 5 and 6 we investigate the behaviour of the cloud in the internal regions of the halos. Figures 3.10 and 3.12 show our results obtained for a cloud with $M \sim 10^6$ M$_\odot$ (simulations 4 and 5), while in Figures 3.11 and 3.13 we report the results of the simulation 6, which models the motion of a cloud with $M \sim 10^5$ M$_\odot$. In contrast with the previous simulations, the velocity (shown in the right panels of Figures 3.10 and 3.11) has a clear decrease with time, especially for the less massive cloud. The reason is that the effects of the coronal gas are quite imortant for the motion of the cloud (the drag time is shorter, as shown in the left panel of Figure 3.5).

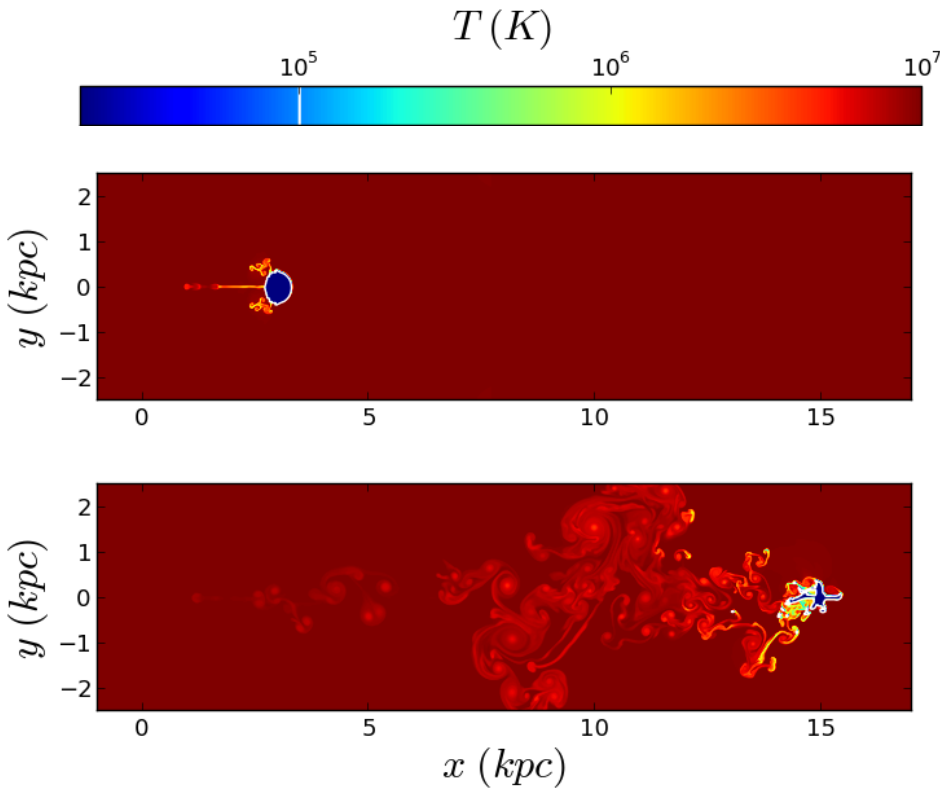

Figure 3.9: Upper panel: Temperature map of simulation 3 after 20 Myr. Bottom panel: temperature map of simulation 3 after 100 Myr. The white contours are located in the two snapshots at $T = 10^5$ K.

Looking at the temperature maps (Figures 3.12 and 3.13), we can see that the cloud, in both cases ($M_{\rm cl} \sim 10^6, 10^5$ M$_\odot$), is destroyed by the interactions with the coronal gas. The evolution of the mass of cold gas (left panels of Figures 3.10 and 3.11) is very different between simulations with or without cooling: if the radiative cooling is implemented, there is an increase of the mass of cold gas, while the opposite happens in the simulation without cooling. This behaviour is due to the high densities of the hot gas in these simulations (see Table 3.1). The cooling time in fact is inversely proportional to the square of the gas density (equation (3.15)), therefore it becomes quite low in these simulations and the cooling, when implemented, is very efficient. The temperature maps of Figures 3.12 and 3.13 show that a lot of gas is stripped from the cloud and there is mixing with the hot corona. In the presence of the radiative cooling, there is the condensation of the mixed material, that cool fast and increases the total mass of cold gas (Marinacci et al., 2010; Armillotta et al., 2016). The evolution of the cold gas mass however would be significantly different with the implementation of any heating sources and of the thermal conduction. Without cooling instead the mass of

the cold gas strongly decreases with time.

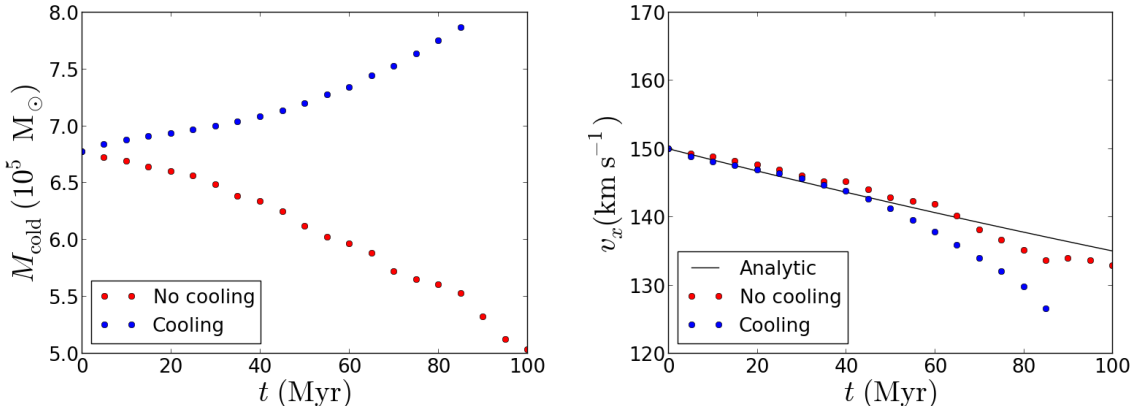

Figure 3.10: Similar to Figure 3.6, but for a cloud of $M_{\rm cl} \sim 10^6$ M$_\odot$ moving in the inner region of the halo, where the coronal density is higher (simulations 4 and 5). We show the results of simulation 4 only after 85 Myr, because it crashed after this time for a technical problem.

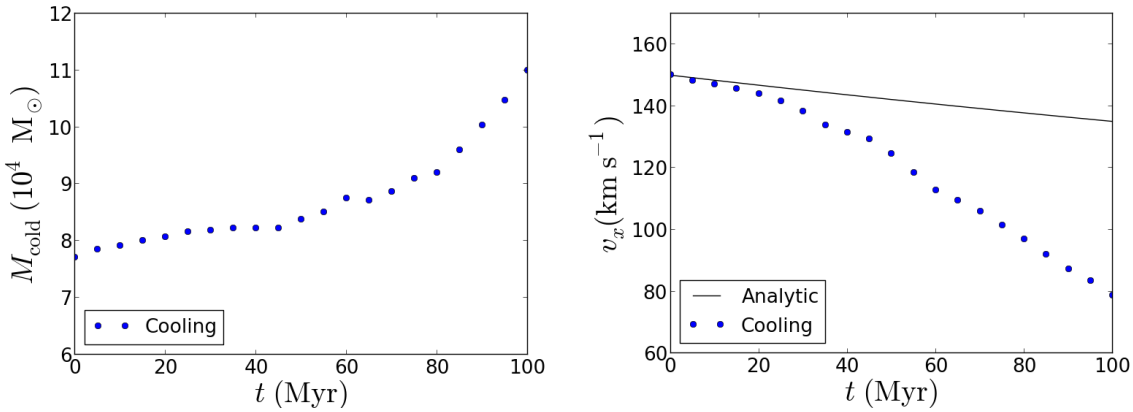

Figure 3.11: Similar to Figure 3.10, but for a lower mass of the cloud ($M_{\rm cl} \sim 10^5$ M$_\odot$), in the presence of cooling (simulation 6).

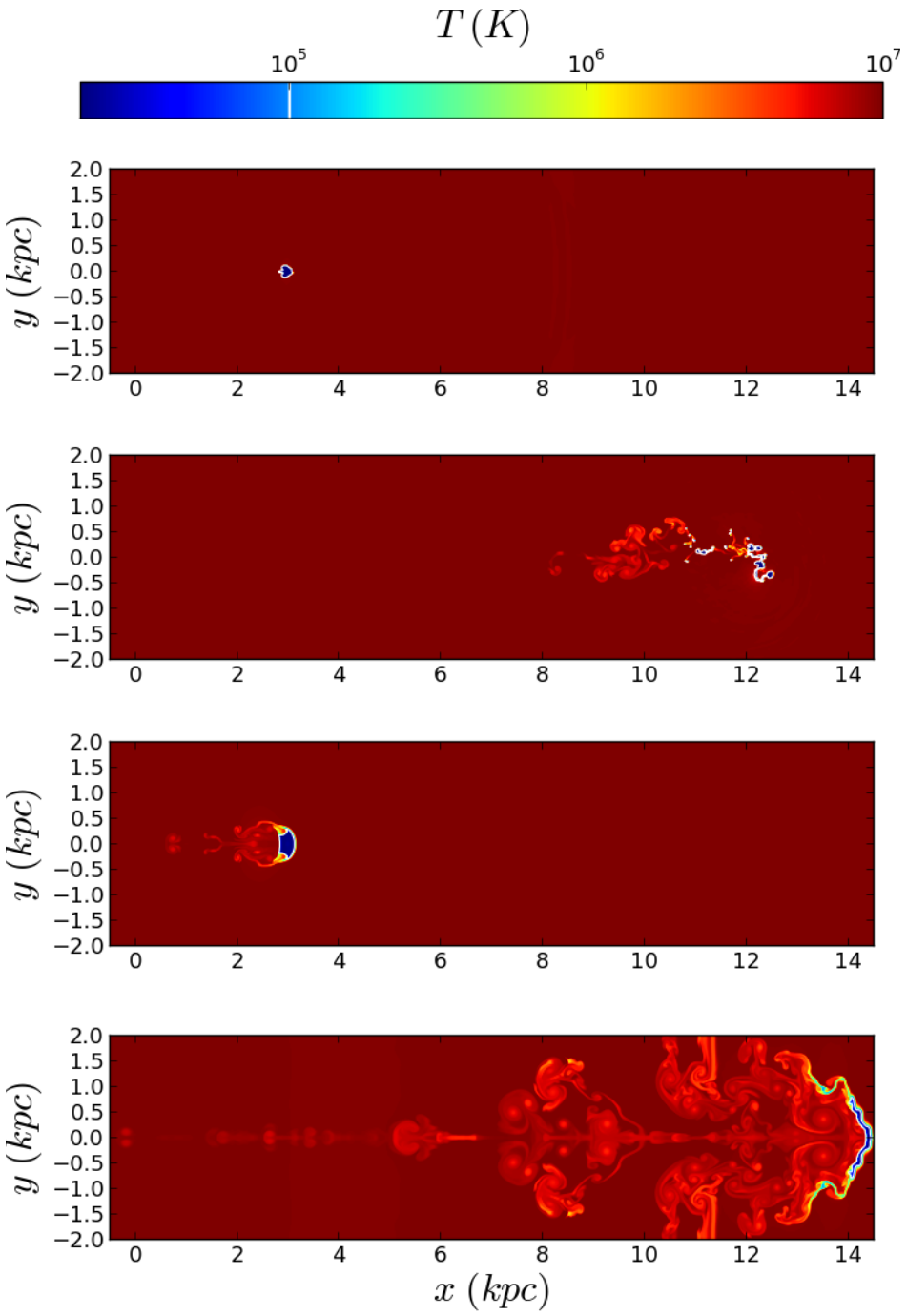

Figure 3.12: First and second panels: temperature maps of simulation 4 respectively after 20 and 85 Myr. Third and fourth panels: temperature maps of simulation 5 respectively after 20 and 100 Myr. The white contours are located in all snapshots at $T = 10^5$ K.

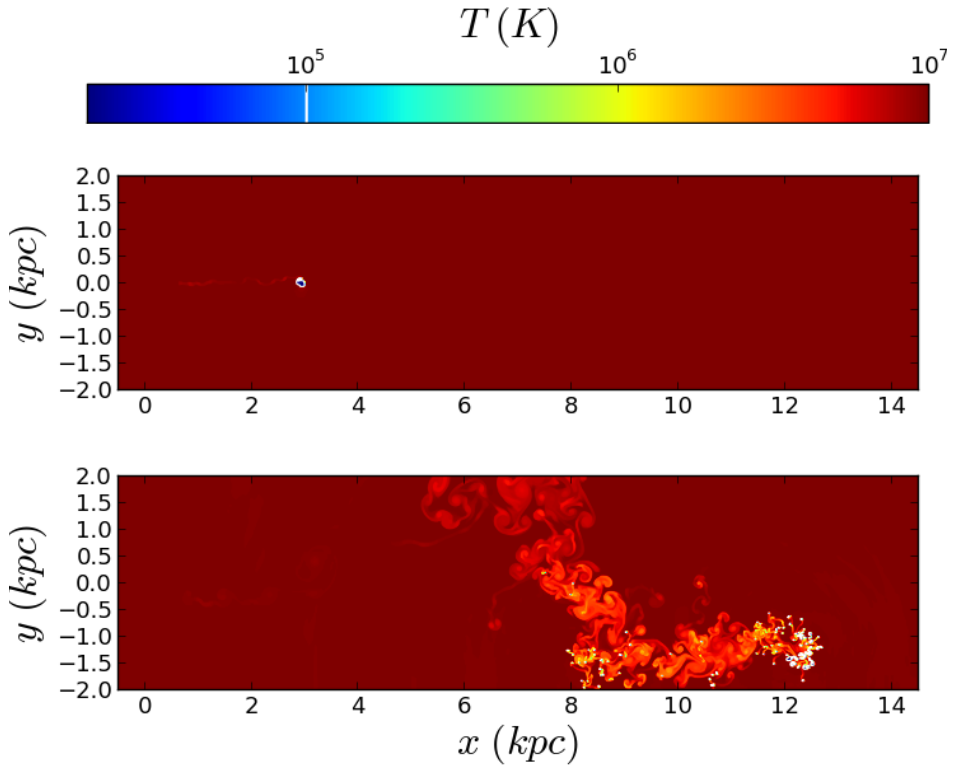

Figure 3.13: Upper panel: Temperature map of simulation 6 after 20 Myr. Bottom panel: temperature map of simulation 6 after 100 Myr. The white contours are located in the two snapshots at $T = 10^5$ K.

3.4 Discussions and conclusions

In this chapter we have studied the physical state of the cold CGM clouds, using analytic calculations and hydrodynamical 2-D simulations. We have found that typical CGM clouds are not self-gravitating and must therefore be pressure-confined by a surrounding hot corona. We have also found, however, that the condition of pressure equilibrium with the corona is in tension with observational estimates of the density of the cold CGM, unless the clouds are mostly confined in the external regions of galaxy halos. We have also seen that the drag time is very large in these regions, allowing clouds of cold gas to survive to hydrodynamical interactions with the corona for several dynamical times, while it is shorter at low radii due to the increase of the hot gas density. We also performed and discussed hydrodynamical simulations, which confirm that at the low coronal densities of the external regions the motion of massive clouds is unaffected by the interactions with the hot gas. This leads us to conclude that the clouds in these region behave like bullets and their motion can be considered nearly ballistic. Nevertheless, the simulations run for only 100 Myr and to have more definitive

results we would have to simulate the motion of the cloud for a longer time. We have also found, both analytically and with simulations, that more massive clouds are more likely to survive to coronal interactions than less massive ones. The simulations of the internal regions instead, show that the clouds are destroyed by the interactions with the coronal gas. We have also found, however, that, in the presence of cooling, the total mass of cold gas can increase with time due to partial condensation of coronal gas. This picture, however, could be modified by the inclusion of heating and thermal conduction.

In summary, we have found that the survival of the CGM clouds is strongly connected to the ambient medium in which they are embedded. If the clouds are located in the external regions, the hot corona is diffuse and does not influence much the cloud motion, while in the internal regions, the drag force acted by the high-density hot gas and Kelvin-Helmholtz instabilities can destroy the clouds.

Chapter 4

Equilibrium models

In this chapter we present and discuss models of collisionless dynamical equilibrium which try to reproduce the observed properties of the CGM of nearby ETGs (see Chapter 2) and in particular the observed values for the column density and of the velocity dispersion (see Section 2.3). In Section 4.1 we introduce the Jeans equation. In section 4.2 we present a variety of isotropic models and we show that they are inconsistent with observations, unless very special assumptions are made. In Section 4.3 we consider more general anisotropic models and we discuss in which conditions they can give account for the observed properties of the CGM in ETGs. Finally, in Section 4.5 we discuss our results and we outline our conclusions.

4.1 The Jeans equation

As a starting point for our collisionless equilibrium models of the CGM in ETGs, we assume spherical symmetry and we make use of the Jeans Equation (e.g. Binney and Tremaine, 1987):

$$\frac{d\rho(r)\sigma_r^2(r)}{dr} + \frac{2\beta(r)\rho(r)\sigma_r^2(r)}{r} = -\rho(r)\frac{GM(r)}{r^2} \tag{4.1}$$

where $\sigma_r(r)$ and $\rho(r)$ are the radial velocity dispersion and the density distribution of the tracer population (here the CGM clouds), $M(r)$ is the dynamical mass profile of the system, which we approximate with a Navarro Frenk White (NFW) profile (Section 2.3.1), and β is the anisotropy, which is defined as:

$$\beta(r) = 1 - \frac{\sigma_\theta^2(r)}{\sigma_r^2(r)} \ , \tag{4.2}$$

where σ_θ^2 is the tangential velocity dispersion. Note, from equation (4.2), that the anisotropy parameter is bound to obey the inequality:

$$\beta \leq 1 \tag{4.3}$$

We will make use of the condition (4.3) in Section 4.3 to discriminate between physical and unphysical models. For isotropic models, $\sigma_r^2 = \sigma_\theta^2$, therefore $\beta = 0$.
The density distribution in equation (4.1) is:

$$\rho(r) = n_{\rm cl} M_{\rm cl} \tag{4.4}$$

where $n_{\rm cl}$ is the number of clouds per unit volume and $M_{\rm cl}$ is the mass of each cloud. From the density distribution described in (4.4), we can obtain the projected column density using the following equation:

$$N_H(R) = \frac{2}{\mu m_{\rm p}} \int_R^{r_{\rm vir}} \frac{\rho(r) r}{\sqrt{r^2 - R^2}} dr \ , \tag{4.5}$$

where R is the projected radius, $r_{\rm vir}$ is the virial radius which we assume equal to 451 kpc, the typical virial radius for ETGs in our sample (see Section 2.3.1), μ is the mean molecular weight of the gas and $m_{\rm p}$ is the proton mass.

4.2 Isotropic models

In this section we explore the models with an isotropic velocity dispersion tensor. As we have already pointed out, the anisotropy parameter β vanishes in this case and equation (4.1) simplifies to:

$$\frac{d\rho(r)\sigma_r^2}{dr} = -\rho(r)\frac{GM(r)}{r^2} \ . \tag{4.6}$$

Solutions for equation (4.6) can be found following two different strategies. One possibility is to assume a velocity dispersion profile σ_r and solve equation (4.6) for the density $\rho(r)$. We will follow this route in Sections 4.2.1 and 4.2.2. Conversely, one can assume a density profile $\rho(r)$ and solve the equation for the velocity dispersion, which we will do in Sections 4.2.3 and 4.2.4.

4.2.1 Models with a constant velocity dispersion

We first consider a simple model in which the velocity dispersion of the clouds is constant with radius and equal to the observed value of 153 km s^{-1} (equation (2.5)). Under this assumption the density distribution, obtained integrating equation (4.6) is:

$$\rho(r) = \rho(r_{\rm vir}) \exp\left(\frac{1}{\sigma_r^2} \int_r^{r_{\rm vir}} \frac{GM(r)}{r^2} dr\right) \ , \tag{4.7}$$

where $M(r)$ is the dynamical mass profile, which we approximate to a NFW (see Section 2.3.1). In the left hand-panel of Figure 4.1, we show the resulting density profile, normalized to $\rho(r_{\rm vir})$. We see that if the CGM absorbers have a constant velocity dispersion, the Jeans Equation forces the clouds to concentrate in the inner regions of the halos, close to the galaxies, with a very centrally peaked density profile.

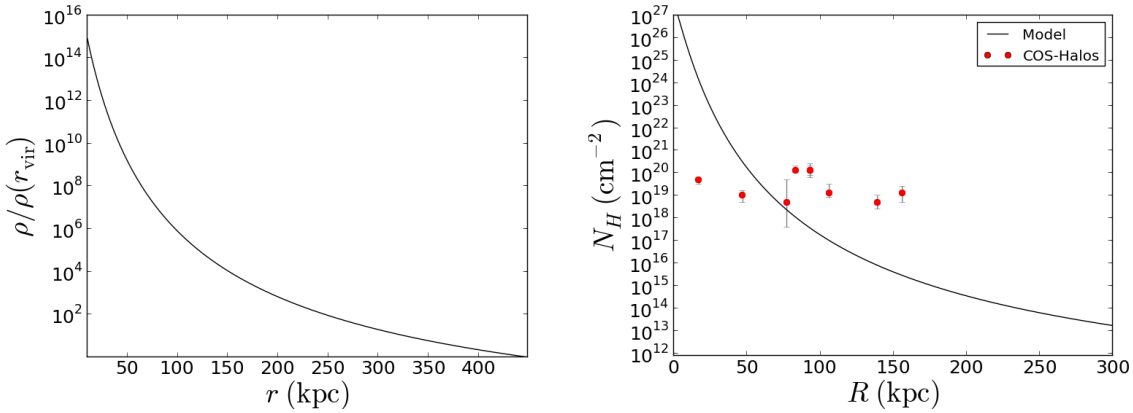

Figure 4.1: Left, density profile obtained solving the Jeans Equation with a velocity dispersion constant with radius and equal to the observed value of 153 km s^{-1}. Right, projected column density profile, compared with COS Halos observations.

In the right-hand panel of Figure 4.1 we show how this model compares with observations for the column density of the CGM (see Section 2.3). To compute the model column density profile, we have used equation (4.5) and we have chosen the normalization $\rho(r_{\rm vir})$ in order to maxime the agreement with the data. Even in this way, we clearly see that the model and the data are inconsistent with each others. This indicates that an isotropic model with a constant velocity dispersion is not a correct description of the CGM kinematics. In particular, the data points have a distribution which is nearly flat with the galactocentric radius, while the surface density curve of our model has a very steep gradient between the internal and the external regions, with differences of more than ten orders of magnitude.

4.2.2 Models with a radial variation of the velocity dispersion

We have seen that a model with a constant dispersion is not a good description of the CGM of ETGs. For this reason, we explore here models with a radially varying velocity dispersion. First, we consider models with a linear radial variation of the velocity dispersion:

$$\sigma_r(r) = Ar + B \ , \tag{4.8}$$

where $A = \frac{\sigma_2 - \sigma_1}{r_2 - r_1}$, and $B = -r_1 \frac{\sigma_2 - \sigma_1}{r_2 - r_1} + \sigma_1$, while $\sigma_1 = \sigma(r_1)$, $\sigma_2 = \sigma(r_2)$, where r_1 and r_2 are two reference radii. In the following, we adopt $r_1 = 1$ kpc and $r_2 = r_{\rm vir}$.
Then we explore models where the velocity dispersion profile is described by a power-law:

$$\sigma_r(r) = \sigma_0 \left(\frac{r}{r_0} \right)^{\alpha} , \tag{4.9}$$

where we fix $r_0 = 10$ kpc and $\sigma_0 = \sigma_r(r_0)$. In both cases the solution depends on two parameters.
The solution of the Jeans Equation using a radially varying velocity dispersion is given by:

$$\rho(r) = \rho(r_{\rm vir}) \exp \left(\int_r^{r_{\rm vir}} \frac{1}{\sigma_r^2(r)} \left(\frac{GM(r)}{r^2} + \frac{d\sigma_r^2(r)}{dr} \right) dr \right) , \tag{4.10}$$

where, as in Section 4.2.1, the normalization $\rho(r_{\rm vir})$ will be calibrated a posteriori to obtain the best match with the observed column densities. Then, we calculated the line-of-sight velocity dispersion, using equation (Binney and Tremaine, 1987; equation (4-57)):

$$\sigma_{los}^2(R) = \frac{2}{\Sigma(R)} \int_R^{r_{\rm vir}} \frac{\sigma_r^2(r) \rho(r) r}{\sqrt{r^2 - R^2}} dr , \tag{4.11}$$

where $\Sigma(R) = N_H(R) \mu m_{\rm p}$. We calculated then, for every models, the mean line-of-sight velocity dispersion, weihgted with the surface density:

$$\bar{\sigma}_{los} = \frac{\sum_{i=1}^{N} \sigma_{\rm los}(R_i) \Sigma(R_i)}{\sum_{i=1}^{N} \Sigma(R_i)} , \tag{4.12}$$

where R_i are the projected radii of the observations (see Table 2.1). To make a quantitative comparison with observations, we associate to each of our models the quantity:

$$\Delta\sigma_{\rm obs} = \frac{|\bar{\sigma}_{los} - \sigma_{obs}|}{\delta_\sigma} , \tag{4.13}$$

where $\sigma_{\rm obs} = 153$ km s^{-1} and $\delta_\sigma = 16$ km s^{-1} are the observed value and the uncertainty on the velocity dispersion of CGM clouds, as discussed in Section 2.3 (see equations (2.5) and (2.6)).
Similarly, for a quantitative comparison of models with the observed column densities, we define the reduced chi square:

$$\chi^2_{N_H} = \frac{1}{N-2} \sum_{i=1}^{N} \frac{(N_{H_i} - N_{H_i,obs})^2}{\delta^2_{N_{H,i}}} \tag{4.14}$$

where N_{H_i} and $N_{H_i,obs}$ are respectively the model and observed column density at $R = R_i$, $\delta_{N_{H,i}}$ are the errors on the observations and $(N-2)$ is the number of degrees of freedom (there are two free parameters for each model).

Results for the linear models

In Figure 4.2 we show the two diagnostics of our models, $\Delta\sigma_{\rm obs}$ and $\chi^2_{N_H}$, defined respectively in equations (4.13) and (4.14), as a function of the free parameters σ_1 and σ_2 (the radial velocity dispersion respectively at 1 kpc and at the virial radius), for the linear model described in equation (4.8). We explore the parameter plane varying σ_1 and σ_2 from 40 to 450 km s^{-1}. The contours mark the regions where the results of our models are in the best agreement with the observations, where the values of the diagnostics are minimized. Looking at the left panel, note that the models with a velocity dispersion more similar to the observed one are in the region of the plane with $140 < \sigma_1 < 150$ km s^{-1}, while there is a low dependence on the value of σ_2. From the right panel instead, we see that the models in agreement with the observed column densities have $\sigma_1 \gtrsim 300$ km s^{-1}. The comparison between the two map therefore leads us to conclude that no one of the models with a linear velocity dispersion can describe simultaneously the two constraints given by the observations.

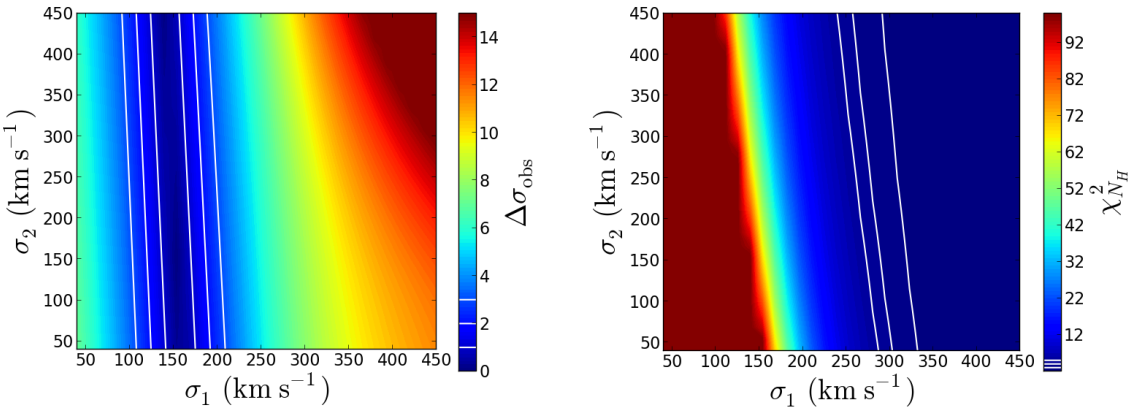

Figure 4.2: Quantitative comparison between model predictions and observed properties of the CGM of ETGs, in terms of velocity dispersion (left, see equation (4.13)) and column density (right, see equation (4.14)), for a model of collisionless isotropic equilibrium with a linearly varying velocity dispersion (equation (4.8)). The contours are placed at 1, 2 and 3 in the left panel and at 3, 4 and 5 in the right panel.

To better illustrate our finding, we briefly describe in some more detail the behaviour of a couple of models, choosen to be representative examples. We first consider a model with $\sigma_1 = 160$ km s^{-1} and $\sigma_2 = 110$ km s^{-1}, which, on the basis of Figure 4.2, is formally favoured in terms of velocity dispersion but disfavoured in terms of column

densities. As shown in Figure 4.3, in this model the line-of-sight velocity dispersion (left) lies within the observed range in the whole radial domain, but the column density (right) is discrepant with observations by several orders of magnitudes especially in the inner regions. We then inspect the results of a model with $\sigma_1 = 400$ km s^{-1} and $\sigma_2 = 50$ km s^{-1}, which is, conversely, favoured in terms of the column densities but not in terms of the velocity dispersion. Looking at Figure 4.4, we can see that the column density has a nearly flat profile, in agreement with the observations, but the line-of-sight velocity dispersion has values much higher than the observed one.

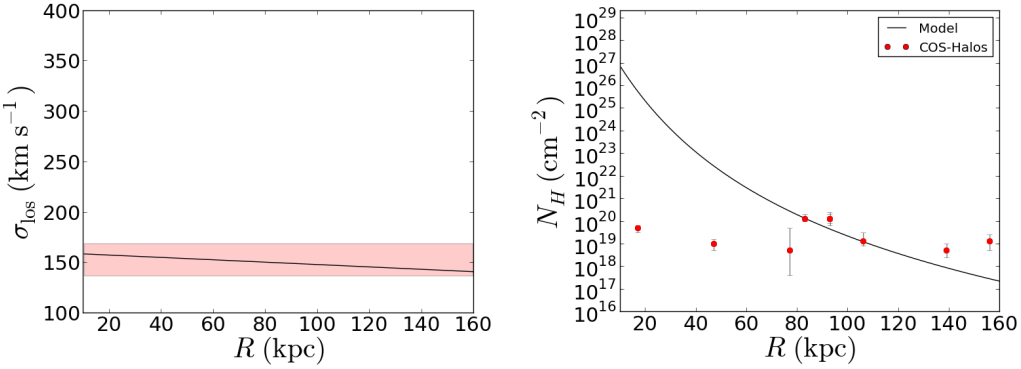

Figure 4.3: Projected profiles of a collisionless model with a linearly varying velocity dispersion (equation (4.8)) with $\sigma_1 = 160$ km s^{-1} and $\sigma_2 = 110$ km s^{-1}. Left, line-of-sight velocity dispersion; right, column density. The orizhontal band in the left panel and the points in the right panel represent the observed values.

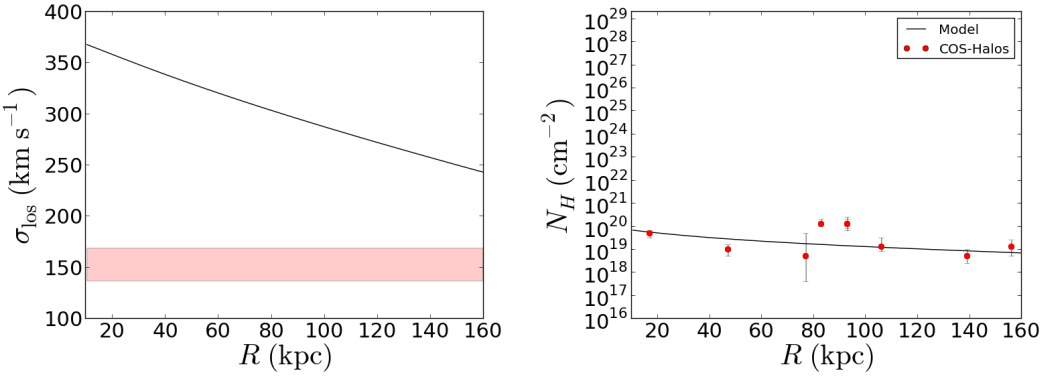

Figure 4.4: Similar to Figure 4.3, but for a model with $\sigma_1 = 400$ km s^{-1} and $\sigma_2 = 50$ km s^{-1}.

Results for the power-law models

Let us now consider the results of the models where the radial velocity dispersion is described by a power law profile, described by equation (4.9). We explored models with positive and negative power-law indices α varying from -0.5 to 0.9, while σ_0 (the radial velocity dispersion at $r_0 = 10$ kpc) was allowed to vary from 120 to 350 km s^{-1}.

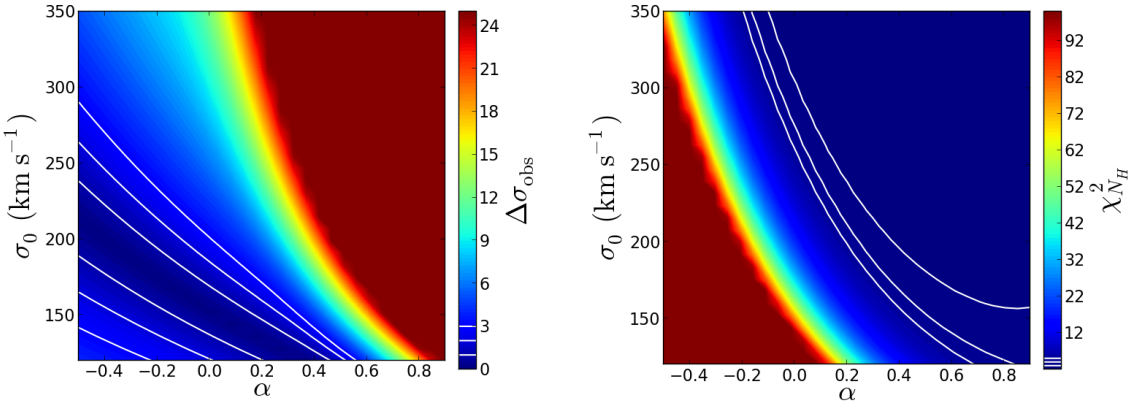

Figure 4.5: Similar to Figure 4.2, but for a model with a power-law velocity dispersion, described by equation (4.9).

In Figure 4.5 we show the results of the power-law models for the velocity dispersion (left panel) and for the colmn density (right panel). We can see that, as for the linear models, the region of the parameter plane where our models have a velocity dispersion in agreement with the observed one is not consistent with the region of the plane where the models have the best results for the column densities. Therefore, also with a power-law velocity dispersion, our models are not able to reproduce at the same time the two observational constraints. In the region of the parameter plane that we have inspected, the best models in reproducing both the constraints have $120 \lesssim \sigma_0 \lesssim 150$ km s^{-1} and $0.2 \lesssim \alpha \lesssim 0.4$. An example is shown in Figure 4.6, where we show the projected density profile for a model with $\sigma_0 = 120$ km s^{-1} and $\alpha = 0.4$. This model, on the basis of Figure 4.5, has a line-of-sight velocity dispersion in agreement with the observed one, because it is in the region of the parameter plane where $\Delta\sigma_{\rm obs}$ is minimized. Regarding the projected densities, the plot in Figure 4.6 shows that the model profile matches quite well most of the observed points, but in the central regions, there are three orders of magnitude between the model and the observed column density. Therefore, even our best models have problems to reproduce simultaneously the observed velocity dispersion and column densities and we conclude that this is a not good description of the CGM in early-type galaxies.

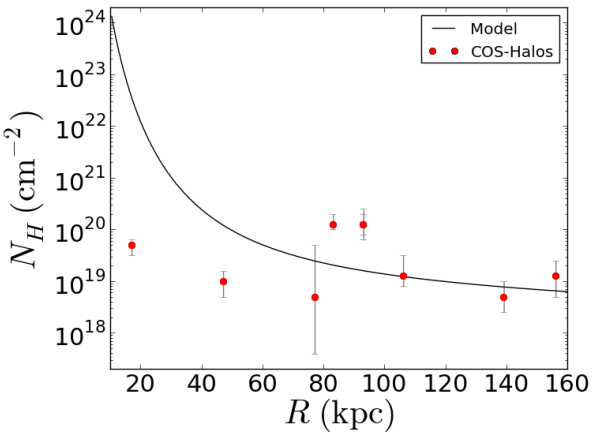

Figure 4.6: Column density profile of a collisionless model with the velocity dispersion described by a power-law (see equation 4.9) with $\sigma_0 = 120$ km s^{-1} and $\alpha = 0.4$. The points represent the observed column densities.

4.2.3 Models with the density described by a power law

As explained at the beginning of Section 4.2, an alternative approach to the solution of the Jeans equation (4.6) is to assume a density profile and solve the equation for the velocity dispersion. In this section, we explore this approach, assuming that the density profile is described by a power law:

$$\rho(r) = \rho_0 \left(\frac{r}{r_0} \right)^{\alpha} , \tag{4.15}$$

with $r_0 = 1$ kpc and $\rho_0 = \rho(r_0)$.
The solution of the equation (4.6) is:

$$\sigma_r^2(r) = \frac{1}{\rho(r)} \left(\int_r^{r_{\rm vir}} \rho(r) \frac{GM(r)}{r^2} dr + \rho(r_{\rm vir}) \sigma_r^2(r_{\rm vir}) \right) , \tag{4.16}$$

where $\sigma_r(r_{\rm vir})$ is the radial velocity dispersion at the virial radius. Note that the normalization of the density profile does not affect the solution (the constant quantity $\rho_0 \cdot r_0^{\alpha}$ cancels out in the numerator and the denominator), so in these models we have again two free parameters: α and $\sigma_r(r_{\rm vir})$.

Results

Similar to the results shown in Section 4.2.2 for the models with a linear and a radial variation of the velocity dispersion, we show in Figure 4.7 the results of the models

with the density describe by a power-law, varying α from -10 to 10 and $\sigma_r(r_{\rm vir})$ from 1 to 150 km s^{-1}. From the left-hand panel, we see that $\Delta\sigma$ is independent on $\sigma_r(r_{\rm vir})$ and that, in order for the velocity dispersion to be consistent with observations, a very steeply declining density profile ($\alpha \lesssim -8$) is required. On the other hand, from the right-hand panel we see that the $\chi^2_{N_H}$ is again not dependent on $\sigma_r(r_{\rm vir})$ (this is obvious because the density profile does not depend on this parameter, see equation (4.15)), but the best models in reproducing the observations have $\alpha \gtrsim -2$. Once again, the two regions are incompatible with each others.

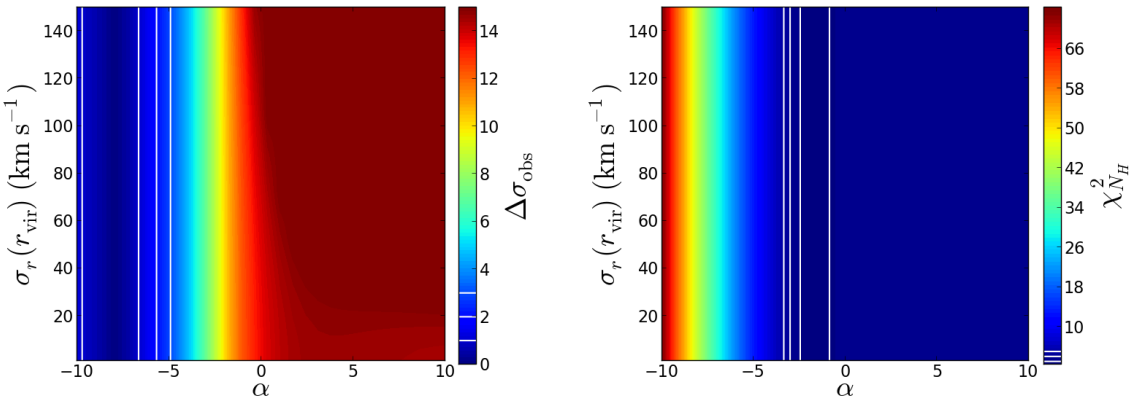

Figure 4.7: Similar to Figure 4.2, but for a model with the density described a power-law (equation 4.15).

An interesting property of Figure 4.7 is that models with a radially increasing density profile perform well in reproducing the observed column density profile, irrespective of the precise value of the slope α. This fact, which is better illustrated in Figure 4.8, demonstrates the potential importance of projection effects: in most of these models, the majority of the clouds is physically located in the outskirts of the halo, but contribute to the column density at smaller radii because of projection. The problem of models with positive α is however that they lead to velocity dispersions much higher than the observed one, as shown by the left map of Figure 4.7. This means that even these power-law density models do not reproduce the observations. Thus, we are not able to explain the kinematics of the CGM clouds with this kind of solutions.
To conclude, in sections 4.2.2 and 4.2.3 we have explored different collisionless isotropic models to describe the CGM kinematics and densities in early-type galaxies, but they all fail in reproduce simultaneously the observed velocity dispersion and column densities. If the absorbers have the requested low velocity dispersion, their density distribution is forced to fall by orders of magnitude from the internal to the external regions; vice versa, to have a radially constant projected density, as COS-Halos observations indicate, the velocity dispersion must be much higher than the observed one. This

conclusion is not dependent to the choice of the free parameters of the explored models and therefore we have to study alternative models to describe the CGM kinematics.

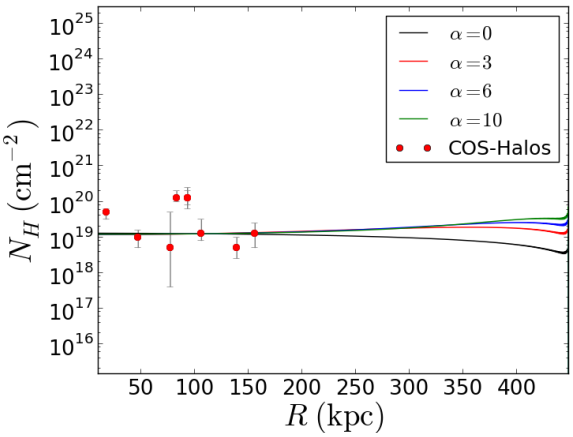

Figure 4.8: Column density profiles of collisionless models with the denisty described by a power law (equation (4.15)), with $\alpha = 0, 3, 6, 10$, compared to the COS-Halos observations.

4.2.4 Models with the absorbers confined to the outer regions

As pointed out in the previous section, it is possible that the CGM clouds are located in the outskirts of galaxy haloes and that they occupy a large range of radii only in projection. To explore this possibility in more detail, we add to our last models one additional parameter: an internal radius ($r_{\rm int}$), corresponding to the intrinsic radius beyond which the CGM clouds are confined. In other words, we cut the distribution of the clouds at the internal radius. This scenario is represented in the diagram of Figure 4.9. It is also interesting to recall that the external regions of a halo are also those where the collisionless equilibrium formalism is most appropriate, because the drag time is larger than the dynamical time, and thus the interactions with the ambient hot gas are negligible. With this configuration, equations 4.5 and 4.11 become:

$$\Sigma(R) = 2 \int_{R_{\rm i}}^{r_{\rm vir}} \frac{\rho(r) r}{\sqrt{r^2 - R^2}} dr \ , \tag{4.17}$$

$$\sigma^2_{los}(R) = \frac{2}{\Sigma(R)} \int_{R_{\rm i}}^{r_{\rm vir}} \frac{\sigma^2_r(r) \rho(r) r}{\sqrt{r^2 - R^2}} dr \ , \tag{4.18}$$

where:

$$R_{\rm i} = \begin{cases} r_{\rm int} & \text{if } R \leq r_{\rm int} \\ R & \text{if } R > r_{\rm int} \end{cases}$$

The lower limits of the integrals are due to the fact that the absorbers are located only beyond $r_{\rm int}$.

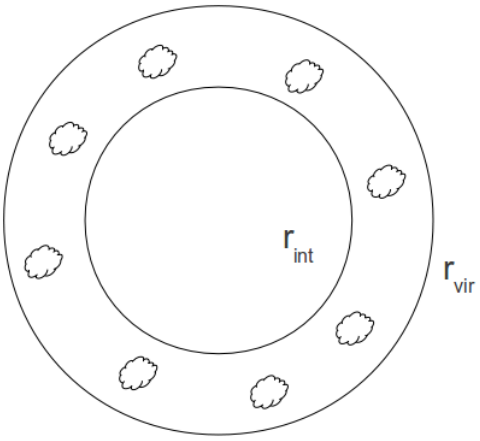

Figure 4.9: Simple diagram that explains the configuration of models with confined clouds. The absorbers are only located in an external shell between $r_{\rm int}$ and $r_{\rm vir}$.

Results and discussions

In Figure 4.10 we show the results obtained from the comparison with the observations of the models with the internal radius and the density described by a power-law (equation (4.15)), varying α from -10 to 10 and $r_{\rm int}$ from 100 to 400 kpc, and fixing to 10 km s^{-1} th velocity dispersion at the virial radius. We obtained similar results also for the other kinds of models (the one of Section 4.2.2). Looking at the left panel, we see that in this case also models with positive α have a velocity dispersion in agreement with the observed one. Moving to the right panel, it shows that all the explored models lead to low values of $\chi^2_{N_H}$ and have therefore a column densities in agreement with the observations. Indeed, with large internal radii, the projected density is flat in the internal regions and matches quite well the observations. An example is shown in Figure 4.11, where we report the column density of a model with $\alpha = -9$ and $r_{\rm int} = 300$ kpc. Our first conclusion is therefore that we can explain the CGM observations, with different radial profiles for the density or the velocity dispersion, if the population of absorbers is concentrated in an external shell of the halo.

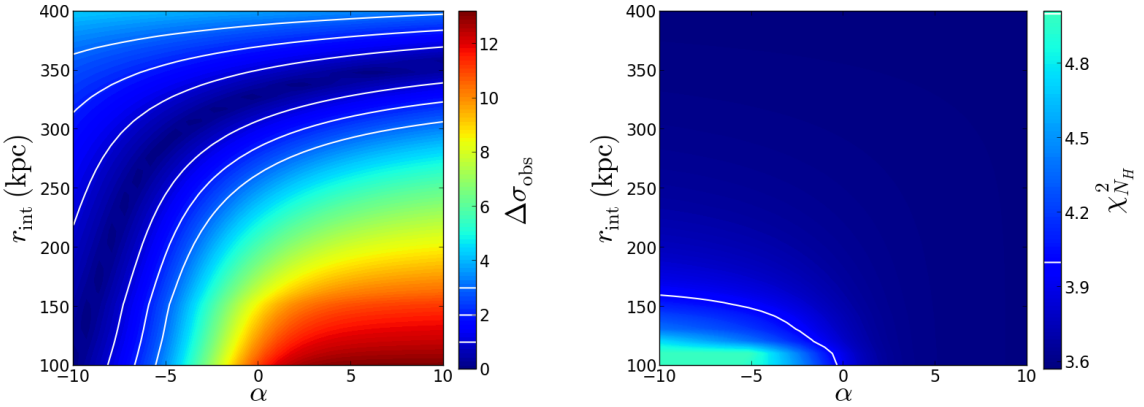

Figure 4.10: Similar to Figure 4.2, but for a model with the density described by a power-law (equation (4.15)) and with the introduction of the internal radius $r_{\rm int}$ as additional parameter of the model

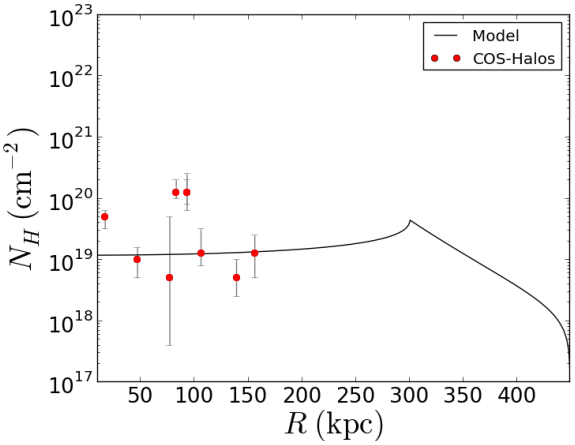

Figure 4.11: Column density profile of a collisionless model with the density described by a power law and with the absorbers confined to the outer regions, with $\alpha = -9$ and $r_{\rm int} = 300$ kpc, compared to the COS-Halos observations.

Even though these models are good at reproducing the observations, their physical interpretation in unclear. It is not clear, in fact, why an internal radius for the CGM should exist at all, in a scenario described by isotropic collisionless models. We try to find an answer to this question in the next section.

4.3 Anisotropic models

In Section 4.2 we have explored several models with an isotropic velocity dispersion tensor, which means that the anisotropy parameter β, defined in equation (4.2), is equal to zero. In a more general scenario the velocity dispersion is not isotropic and the anisotropy parameter assumes a value different from zero: we assess this possibility in this section. The reason why we expect anisotropic models to be interesting is that, if the clouds have orbits which are enough tangentially biased, then they may be naturally confined in the outer regions of the halo by the centrifugal force, with the advantages that we have discussed in Section 4.2.4, without the disadvantage of artificially defining an inner radius for the CGM. For this reason, we will focus most of the time on models with tangentially biased orbits ($\beta < 0$). In the following, we solve equation (4.1), assuming different density profiles (either a power law or a gaussian). For each of these we consider two sets of models: in one we assume a constant anisotropy parameter and we compute a radial velocity dispersion profile from equation 4.19, while in the other we assume a constant radial velocity dispersion, and we compute a radial profile of β from equation (4.21). In a more realistic scenario, both the anisotropy and the radial velocity dispersion could be functions of the radius. However, given the lack of constraints, we explore here two extreme cases. The real behaviour of the solutions will be something intermediate between these two possibilities.
Assuming a constant value for β, equation 4.1 leads, after some algebra, to:

$$\frac{d\sigma_r^2(r)}{dr} = -\sigma_r^2(r)\left(\frac{2\beta}{r} + \frac{1}{\rho(r)}\frac{d\rho(r)}{dr} + \frac{1}{\sigma_r^2(r)}\frac{GM(r)}{r^2}\right) \ . \tag{4.19}$$

This equation is an Ordinary Differential Equation (ODE) of the form $\frac{dy}{dr} = f(y, r)$. We solved it numerically, using *scipy.integrate.odeint* from python, which solves ordinary differential equations using *lsoda* from the FORTRAN library odepack. The line-of-sight velocity dispersion profile with $\beta \neq 0$ is (Binney and Tremaine, 1987; equation (4-60)):

$$\sigma_{los}^2(R) = \frac{2}{\Sigma(R)}\int_R^{r_{\rm vir}}\left(1 - \beta\frac{R^2}{r^2}\right)\frac{\rho(r)\sigma_r^2(r)r}{\sqrt{r^2 - R^2}}dr \ , \tag{4.20}$$

which reduces to equation (4.11) for the isotropic case.

In the second approach, which assumes a constant value of the radial velocity dispersion we find the radial profile of β through the following equation:

$$\beta(r) = -\frac{r}{2\rho(r)}\frac{d\rho(r)}{dr} - \frac{GM(r)}{2r\sigma_r^2} \ , \tag{4.21}$$

which is obtained inverting equation (4.1).

4.3.1 Power law models

We first explore power law anisotropic models, with the density decsribed by equation (4.15), using the two different methods explained above. We first assume a constant β, while in a second moment we assume a constant radial velocity dispersion.

Results for constant β

We first focus on the models with a radially constant anisotropy. We explore the parameter plane varying β from -80 to 0 and α from -10 to 5. In Figure 4.12 we show our results obtained from the comparison with the velocity dispersion (left panel) and with the column densities (right panel). The comparison between the two panel reveals that models with a positive α can reproduce simultaneosly the two observational constraints, because both the diagnostics ($\Delta\sigma_{\rm obs}$ and $\chi^2_{N_H}$) are minimized. We conclude thus that tangentially anisotropic models can explain the COS-Halos observations.

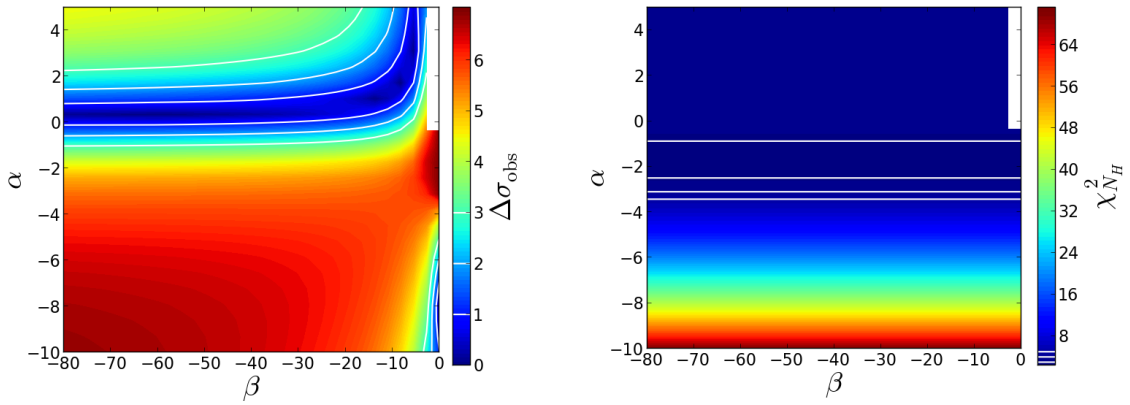

Figure 4.12: Similar to Figure 4.7, but assuming a non-vanishing constant anisotropy.

The white region in Figure 4.12 ($\beta \sim 0$ and $\alpha > 0$) marks models which we identified as physically unacceptable because they implyied unphysically large velocity dispersions. n Figure 4.13 (left) an example is shown drawn out of this region ($\alpha = 4$ and $\beta = -1$): at small radii, the velocity dispersion reaches absurdely large values. We conservatively

excluded from our analysis all models reaching dispersions larger than 2000 km/s. In the right panel of the same figure we show instead, as a comparison, a plot of the radial velocity dispersion of one of our best models, with $\alpha = 1$ and $\beta = -10$. In Figure 4.14 we show instead the plots of the tangential velocity dispersion σ_θ, for the same two models explored in Figure 4.13. We calculate this quantity using the following equation:

$$\sigma_\theta^2 = (1 - \beta)\sigma_r^2 \ , \tag{4.22}$$

obtained inverting equation (4.2). The two panels of Figure 4.14 show that the models in the white region of the parameter plane of Figure 4.12 have also unacceptable tangential velocity dispersions, which have unphysically high values in the outer regions of the halo.

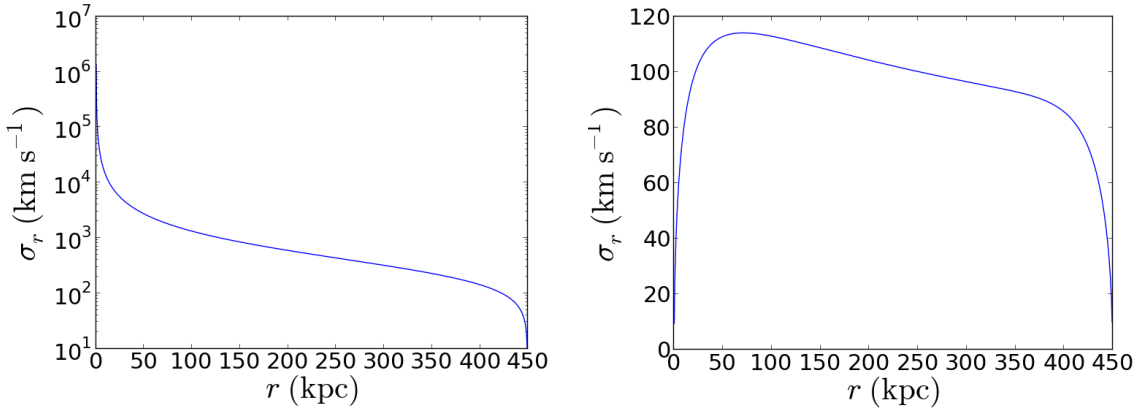

Figure 4.13: Radial velocity dispersion profiles for two anisotropic power-law models with $\alpha = 4$ and $\beta = -1$ (left panel), and with $\alpha = 1$ and $\beta = -10$ (right panel).

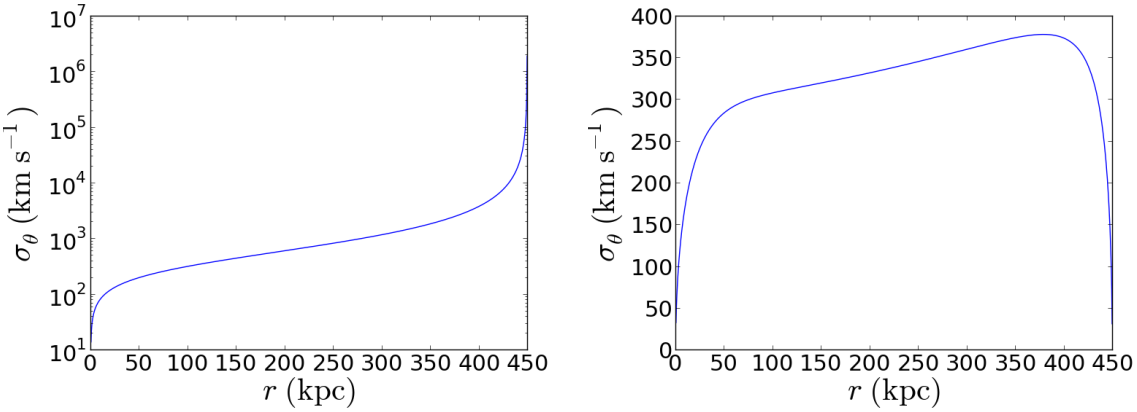

Figure 4.14: Similar to Figure 4.13, but tangential velocity dispersion profiles

Results for constant σ_r

Let us now move to the power-law models with a constant radial velocity dispersion and a radial profile of the anisotropy parameter, obtained with equation 4.21. In Figure 4.15 we show the results for the velocity dispersion, obtained varying α from -10 to 10 and σ_r from 1 to 150 km s^{-1}. The map for the column density is the same shown in Figure 4.12, because the column density depends only on α. We can see that, for $\alpha > 0$, also this kind of models can reproduce well both the velocity dispersion and the column densities.

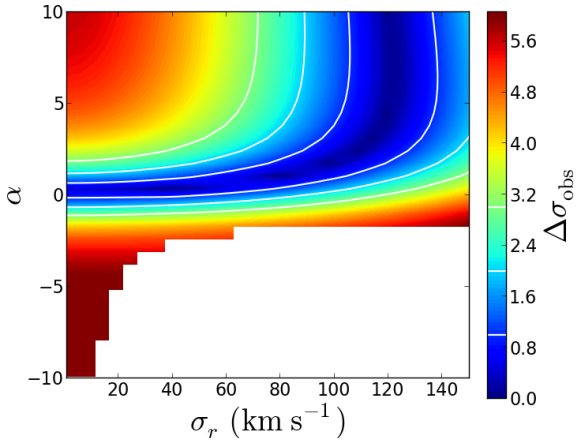

Figure 4.15: Similar to Figure 4.7, but for anisotropic models with a constant radial velocity dispersion.

Again, the white region in the parameter plane of Figure 4.15 marks the models with solutions that are not acceptable. These parameters lead to values of β higher than 1, that is a physical limit for this quantity, as we have seen in Section 4.1. In Figure 4.16 (left) we show as an example the solution of one of these models, with $\sigma_r = 100$ km s^{-1} and $\alpha = -6$. In the internal regions the anisotropy parameter reaches unphysical values. As a comparison, in the right panel of Figure 4.16, we show an example of the radial profile of β for an acceptable model ($\sigma_r = 120$ km s^{-1} and $\alpha = 2$).
From these results we conclude that the kinematics of the CGM clouds could be described by the Jeans Equation, if the clouds are concentrated in the external regions of the halo (power-laws with positive indices) and if their orbits are tangentially anisotropic. This conclusion is not dependent to the radial profile of the anisotropy parameter, because we have found similar results with a constant or a variable β.

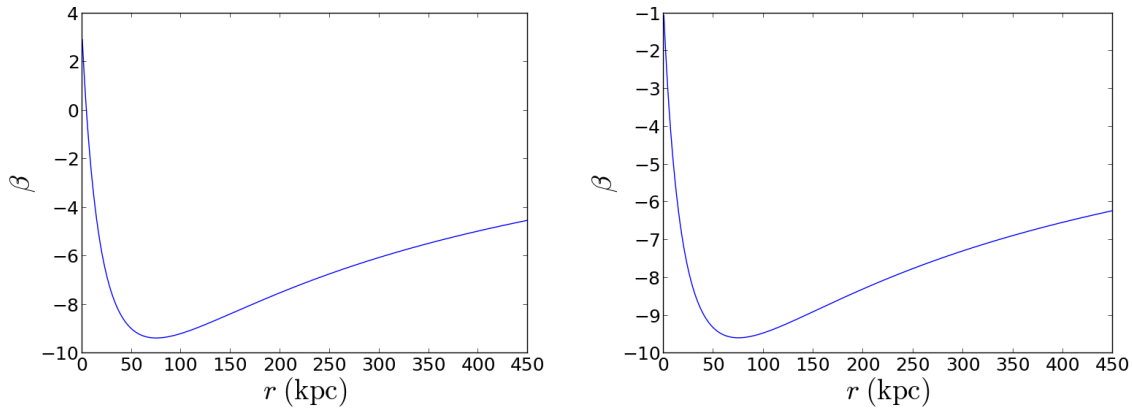

Figure 4.16: Radial profiles of the anisotropy parameter for a model with $\alpha = -6$ and $\sigma_r = 100$ km s^{-1} (left panel), and a model with $\alpha = 2$ and $\sigma_r = 120$ km s^{-1} (right panel).

4.3.2 Gaussian models

The results of the previous section are in line with what we have seen in Section 4.2.4, where we studied models with the absorbers confined in the external regions of the halos. We have found that also with the introduction of anisotropy, the only way to obtain results consistent with the observations is by adopting an increasing density profile, which means that the CGM clouds must be concentrated in the external regions. In this section we explore a different view of the same scenario, by adopting a gaussian density distribution for the absorbers. This type of distribution means indeed that the clouds are confined in an external shell of the halo, similar to what is represented in Figure 4.9. In this scenario however there is not a sharp cut in the density profile and thus the distribution is more physical. This distribution is described by:

$$\rho(r) = \rho_0 \exp\left(-\frac{(r-\bar{r})^2}{2\bar{d}^2}\right) , \tag{4.23}$$

where $\bar{d}$ is the width of the gaussian, $\bar{r}$ is the mean radius of the distribution and the normalization ρ_0 is fixed a posteriori, as usual, by a comparison with the observed column densities. As an example, we show in Figure 4.17, the radial profiles for the density (left) and the column density (right) of a model with $\bar{r} = 300$ kpc and $\bar{d} = 50$ kpc. Note that the column density profile is flat in the internal regions, in agreement with the observations. To have only one free parameter in the density distribution, we fixed the mean radius of the distribution with the equation:

$$\bar{r} = r_{\rm vir} - 2\bar{d} , \tag{4.24}$$

in this way, the width of the gaussian defines also its distance from the centre.

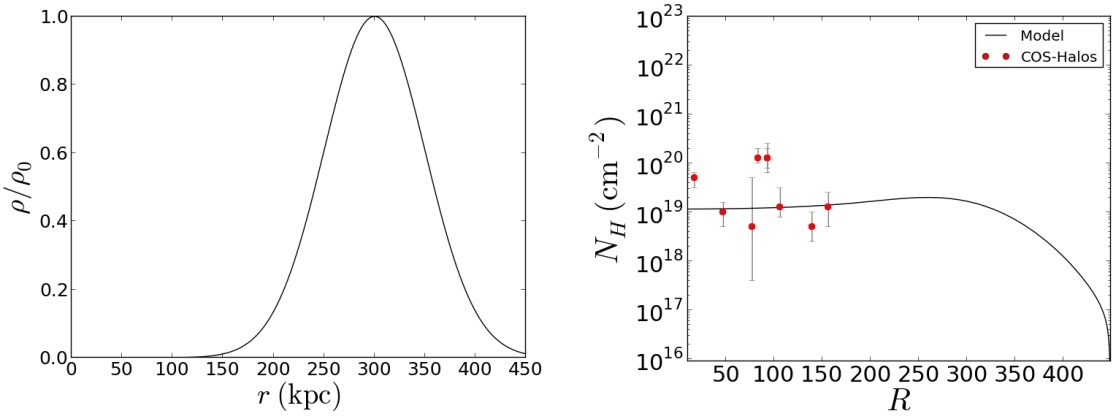

Figure 4.17: Profile of the density (left panel) and of the projected column density (right panel) for a gaussian distribution with $\bar{r} = 300$ kpc and $\bar{d} = 50$ kpc. The points in the right panel depict the COS-Halos observations.

Results for constant β

In Figure 4.18 we show the results of our diagnostics for the velocity dispersion ($\Delta\sigma_{\rm obs}$) and the column density ($\chi^2_{N_H}$), exploring the parameter plane in the region $-80 < \beta < 0$ and $50 < \bar{d} < 200$ kpc, with the $\bar{d}$ and $\bar{r}$ related by equation (4.24). From the comparison between the two panels we can see that there is a region where our models satisfy simultaneosly the two observational constraints, for strongly negative β and $\bar{r}$ between 80 and 120 kpc. Therefore these anisotropic models with the clouds confined to external regions are in well agreement with the COS-Halos observations.

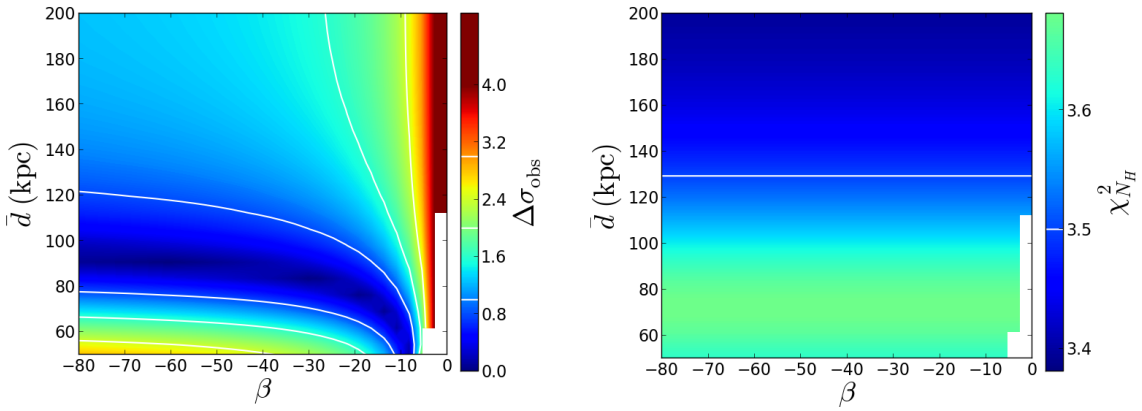

Figure 4.18: Similar to Figure 4.2, but for a model with a non vanishing constant anisotropy and the density described by a gaussian, using equation (4.23). The width $\bar{d}$ and the mean radius $\bar{r}$ are related with each others by equation (4.24).

The region in white of the parameter plane of Figure 4.18 marks also in this case models with unacceptable solutions, because the resulting radial and tangential velocity dispersion profiles are similar to the one shown in the left panels of Figures 4.13 and 4.14. Note the large values of $\Delta\sigma_{\rm obs}$ associated with $\beta = 0$, which imply that isotropic models are not acceptable, confirming what we have already found in Section 4.2.

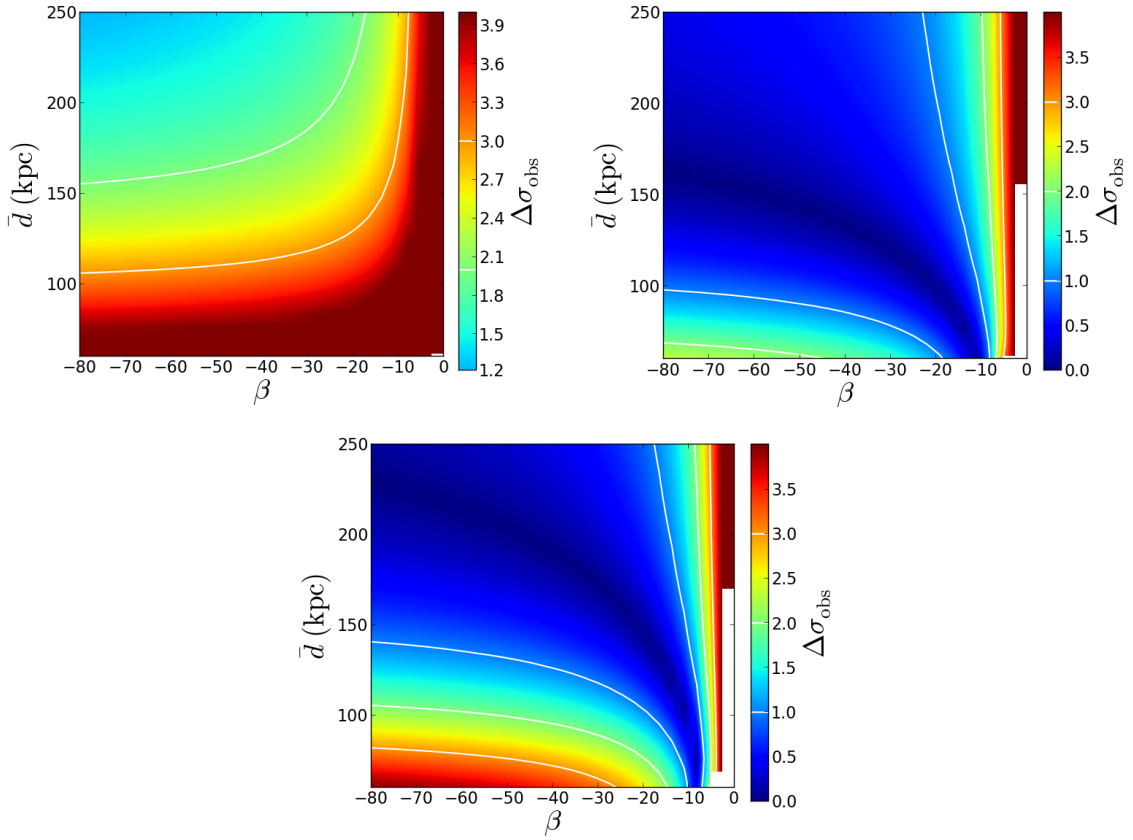

Figure 4.19: Similar to the left panel of Figure 4.18, but with the mean radius fixed at 100 (upper left panel), 300 (upper right panel) and 400 kpc (bottom panel).

For a better analysis of these gaussian models, we show in Figure 4.19 the results of models without the condition expressed by equation 4.24. In these models, we fixed $\bar{r}$ at a specifi radii (100, 300 or 400 kpc) and we allowed $\bar{d}$ to vary between 60 and 250 kpc. The comparison between the three panels allows us to appreciate the effect of the distance from the galaxy center of the gaussian distribution. If the shell of clouds is not far enough from the galaxy, we cannot find satisfactory models, for whatever value of β and $\bar{\sigma}$, while if clouds are located at large galactocentric distances, there are several models that reproduce the observed velocity dispersion, even for gaussian distributions with large widths. This is the most important result of this section: anisotropic Jeans

models can explain the observations if the CGM clouds lie in the outer regions of the galaxy halos.

Results for constant σ_r

To give more robustness to the statement above, we explored also a scenario with a radial variation of the anisotropy parameter and a costant radial velocity dispersion. Using different values of $\bar{\sigma}$ and σ_r we solve equation (4.21) with a density distribution described by equation (4.23), to obtain the β radial profile. We explore the parameter plane in the range $1 < \sigma_r < 200$ km rms^{-1} and $120 < \bar{d} < 280$ kpc and in Figure 4.20 we show our results, obtained with different assumptions for $\bar{r}$.

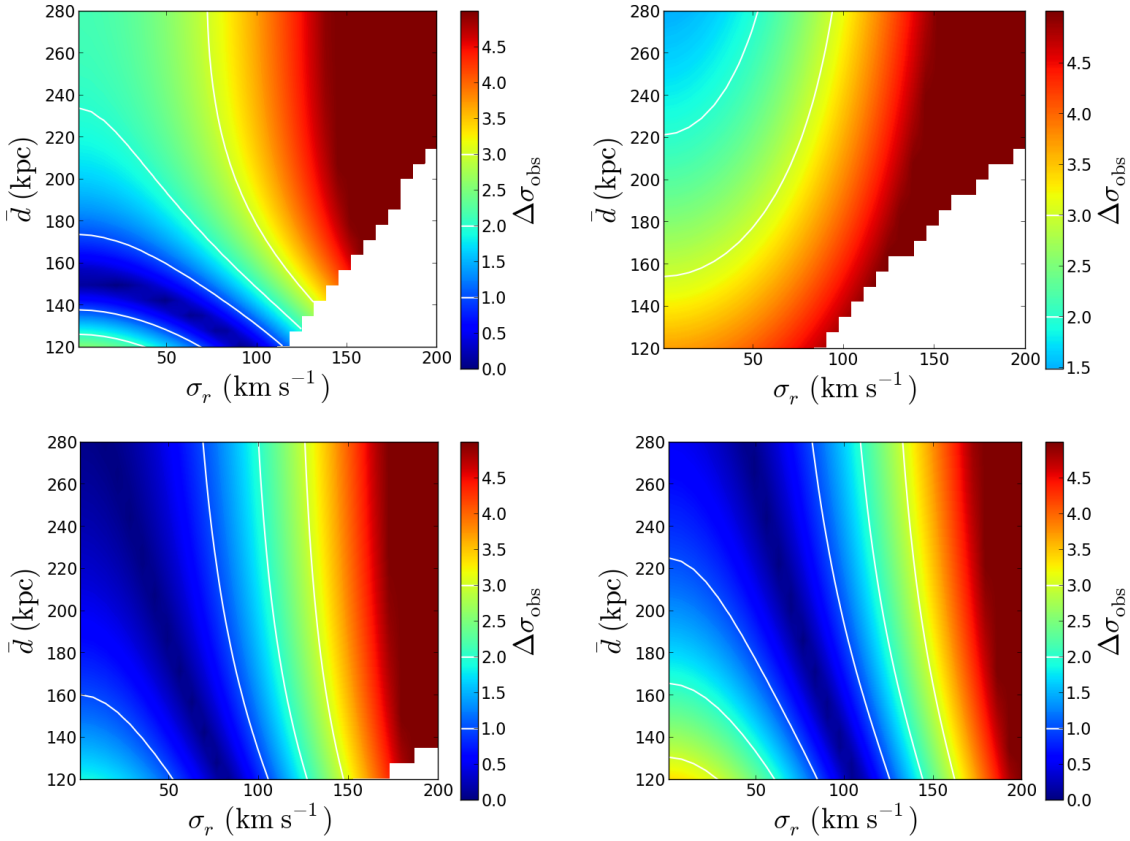

Figure 4.20: Similar to Figure 4.19, but for anisotropic models with a constant radial velocity dispersion and four different assumptions for the the mean radius $\bar{r}$: it is related with the gaussian width by equation (4.24) in the upper left panel, while in the other panels it is fixed at 100 (upper right), 300 (bottom left) and 400 kpc (bottom right).

In the upper left panel of Figure 4.20 the mean radius of the density distribution is related to $\bar{\sigma}$ by equation (4.24). In the other three panels instead we fixed $\bar{r}$ at 100, 300 and 400 kpc. The colormaps show the same behaviour of the previous scenario: there is a region of the plane that is consistent with the observations, and the models with the larger mean radius are the ones that allow the wider shell of clouds. As in Figure 4.18, the white masks represent the regions of the plane that are not acceptable because β assumes values larger than 1. Figure 4.21 shows an example solution of equation 4.21 with $\sigma_r = 190$ km s^{-1} and $\bar{d} = 120$ kpc, which is a white point in the upper right map of Figure 4.20: in this case the anisotropy parameter reaches unphysical values in the external regions.

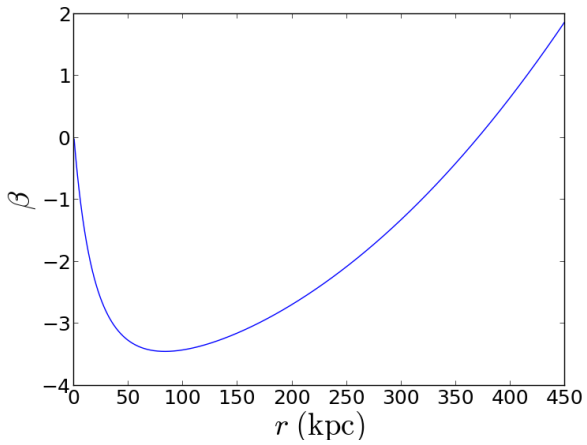

Figure 4.21: Radial profile of the anisotropy parameter for a model with $\bar{d} = 120$ kpc and $\sigma_r = 190$ km s^{-1}.

4.4 Comparison between isotropic and anisotropic models

To understand the influence of the anisotropy on our models, we show here an example of the different line-of-sight velocity dispersion profiles of the same model with or without anisotropy. Figure 4.22 represents the resultant profiles for the same gaussian distribution, with $\bar{r} = 300$ kpc and $\bar{d} = 50$ kpc: in the left panel the velocity dispersion tensor is isotropic, while in the right panel $\beta = -10$. The effect of the tangential anisotropy is to shift at larger radii the peak of the observed dispersion. In fact, a negative anisotropy means that the orbits are nearly circular around the galaxy (though not all with the same rotation axis or sense of rotation, so that the total angular momentum is zero), and so we see the higher velocity component when we

observe the external regions, where the shell of absorbers is located. The COS-Halos observations are instead in the range between 10 and 160 kpc ($0.023 - 0.36\ r_{\rm vir}$): then, with a strong anisotropy, the higher velocities are not observed and the low value of the velocity dispersion is explained. A prediction of this model is that larger velocity dispersions, close to the virial speed (equation (2.10)), should be observed at larger projected radii. This prediction, as the prediction of our column density profiles at large radii (see the end of Section 4.2.3 and Figure 4.8), can be verified or discarded by observations that extend to larger radii than the COS-Halos one (we discuss this in Chapter 6).

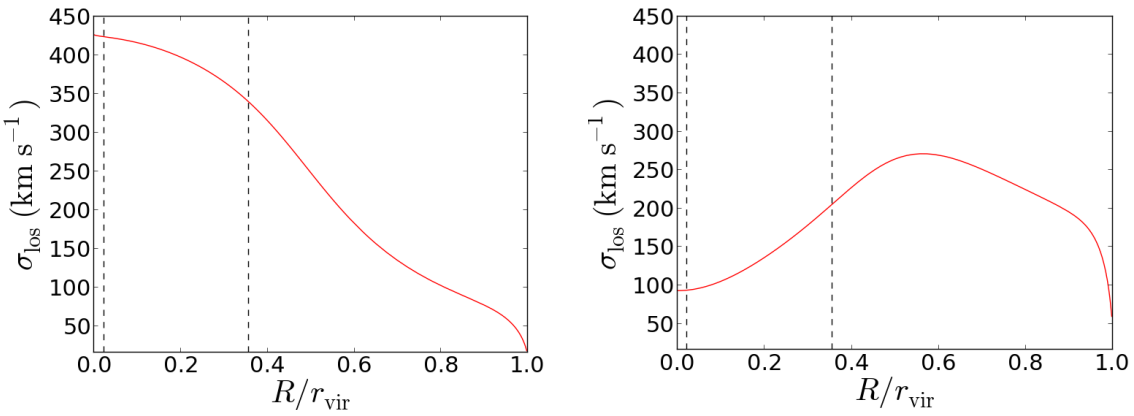

Figure 4.22: Line-of-sight velocity dispersion profiles for a model with the density described by a gaussian distribution with $\bar{r} = 300$ kpc and $\bar{d} = 50$ kpc. In the left panel $\beta = 0$, while in the right panel $\beta = -10$. The vertical dashed-lines represent the minimum and the maximum projected distances of the COS-Halos observations.

4.5 Conclusions

In this chapter we have explored some different collisionless equilibrium models, with the aim of explaining the CGM kinematics and densities of early-type galaxies, as traced by the COS-Halos absorption features. Our first conclusion is that to reach results that are consistent with observations, anisotropic models are preferred. In particular, the models which give the best results have a large tangential anisotropy and clouds concentrated in the external regions of the halo. We have explored models with very different assumptions for the density distribution of the CGM absorbers and we have investigated a large range of parameters. All our investigations lead to the same result that the clouds have to be confined to the outer regions, and this result is in agreement with our finding of Chapter 3, where we have seen that in these regions

the drag time is large and there are weak interactions between massive clouds and hot coronal gas. Thus, these are also the regions where the collisionless formalism is most appropriate, under the assumption of clouds with large masses.
We conclude that the kinematics of the circumgalactic medium is succesfully described by collisionless models of clouds with orbits with a large tangential anisotropy.

Chapter 5

Non-equilibrium models

In this chapter we investigate non-equilibrium models to explain the COS-Halos observations of the cold CGM in the early-type galaxies, focusing on the observed velocity dispersion and total hydrogen column densities (see Section 2.3). In Chapter 4 we considered equilibrium models to explain the CGM velocity dispersion and densities in ETGs. We have found that the only physically satisfactory models that are able to reproduce these observational constraints have a high tangential anisotropy, with the absorbers concentrated in the external regions of the halos. We have seen however in Chapter 3 that the assumption of the CGM as a collisonless system is not completely justified, because the dynamical time of this system is of the order of the drag time. In this chapter we investigate a different scenario to explain the observed CGM densities and kinematics: clouds in a non-equilibrium state. We focus in particular on models which describe a global inflow from the IGM to the galaxies. The outflow scenario is not considered, because the outflow of material with the observed temperature is not expected in these early type galaxies, due to the low observed star formation rates and the absence of AGN features.
In Section 5.1 we explore the scenario of clouds falling toward the galaxy under the sole influence of the gravitational force of the halo, while in section 5.2 we also consider the drag force due to the interaction with the hot gas (corona) of the ETGs. For both scenarios we create a velocity distribution to compare with the observed one and we find that it is difficult to reconcile these models with the observations. We outline our conclusions in Section 5.3.

5.1 Ballistic Models

In the collisionless models of Chapter 4 the CGM absorbers were supported by their velocity dispersion which mantained them in equilibrium into the halos. In the following scenario instead, there is no support for the clouds, which fall from the intergalac-

tic medium towards the centre of the galaxy, due to the gravitational force. In this section we neglect for simplicity the drag effects of the coronal gas and we focus on ballistic models. We first assume that the clouds come from infinity, where they have zero velocity. In this case, the infall velocity at each radius is equal to the escape speed:

$$v_e(r) = \sqrt{2|\Phi(r)|} \ , \tag{5.1}$$

where $\Phi(r)$ is the Dark Matter halo gravitational potential, described by the NFW profile seen in Section 2.3.1. The usual convention is to assume the velocity positive if it has an outward direction: the velocity of an infalling motion would therefore have a negative sign. In the rest of this chapter, we assume then that the velocity is negative, and we usually plot its absolute value, defined as $|v|$. This radial profile is shown in Figure 5.1 (green line).
In a more realistic scenario instead, the clouds are not coming from the infinity, but from a finite radius. If they have $v = 0$ at $r = r_{\rm vir}$ ($r_{\rm vir} = 451$ kpc as shown in Section 2.3.1), then the energy conservation equation becomes:

$$\frac{1}{2}mv(r)^2 = m(\Phi(r) - \Phi(r_{\rm vir})) \ , \tag{5.2}$$

which leads to:

$$v_{\rm fall}(r) = \sqrt{2|\Phi(r) - \Phi(r_{\rm vir})|} \ . \tag{5.3}$$

The velocity profile obtained with this assumption is also shown in Figure 5.1 (blue line).

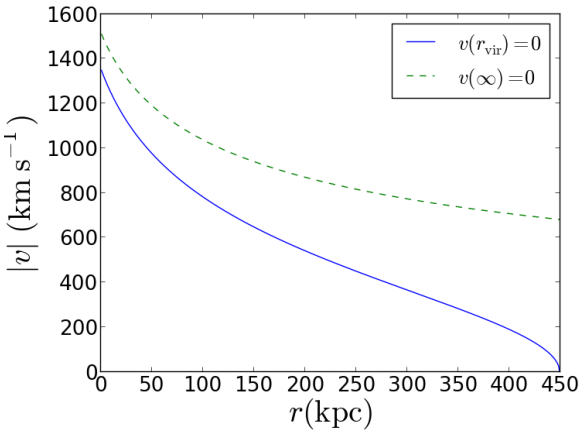

Figure 5.1: Infall velocities, assuming that the velocity vanishes at infinity (green line) or at the virial radius (blue line).

Figure 5.1 shows the two extreme cases of this scenario: if the CGM clouds have an origin external to the Dark Matter halo of the galaxy, their falling velocity will be described by a profile enclosed between the green and the blue lines. The closer to the virial radius is the starting point of the clouds, the lower the infalling velocities. Note that the case $v(\infty) = 0$ predicts velocities that are at least four times larger than the observed dispersion (153 km s^{-1}, equation 2.5) in the entire radial range. For this reason, it is very unlikely to be consistent with observations and we will discard it in our analysis in the following sections.
In both cases, we calculated the infall time of the absorbers, shown in Figure 5.2, using the equation:

$$t_{fall}(r) = \int_r^0 \frac{dr}{v(r)} \tag{5.4}$$

Figure 5.2 shows that obviously the infall time increases with decreasing of the radius where the velocity goes to zero. Even with the lower velocities allowed by our models, the clouds fall to the centre in about 1.3 Gyr.

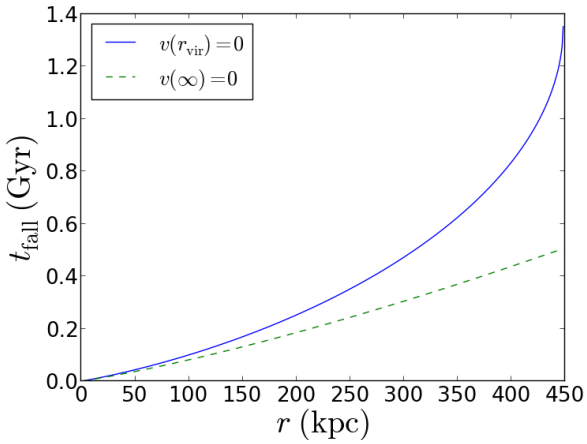

Figure 5.2: Infall times of the CGM clouds as a function of radius, assuming that the velocity vanishes at infinity (green line) or at the virial radius (blue line)

5.1.1 Mass flux conservation

As for the collisionless models of Chapter 4 there are essentially two properties of the CGM clouds that we wish our models to reproduce. The first is their velocity dispersion, the second is the density profile. In particular we are interested in reproducing the column densities of Figure 2.11. In the case of a population of infalling clouds we

can find their distribution through the continuity equation, imposing that the mass flux is constant with radius:

$$4\pi r^2 \rho(r) v(r) = const \ . \tag{5.5}$$

Then, the density profile can be obtained from the equation:

$$\rho(r) = \frac{r_0^2 \rho(r_0) v(r_0)}{r^2 v(r)} \ , \tag{5.6}$$

where r_0 is an arbitrary reference radius. The average particle number density of the model is plotted in the left panel of Figure 5.3. The projected density profile is found then through equation (4.5) and is shown in the right panel of the same figure. The normalization of the two profiles is calculated to better reproduce the observed colum densities, as explained in more detail in Chapter 4.

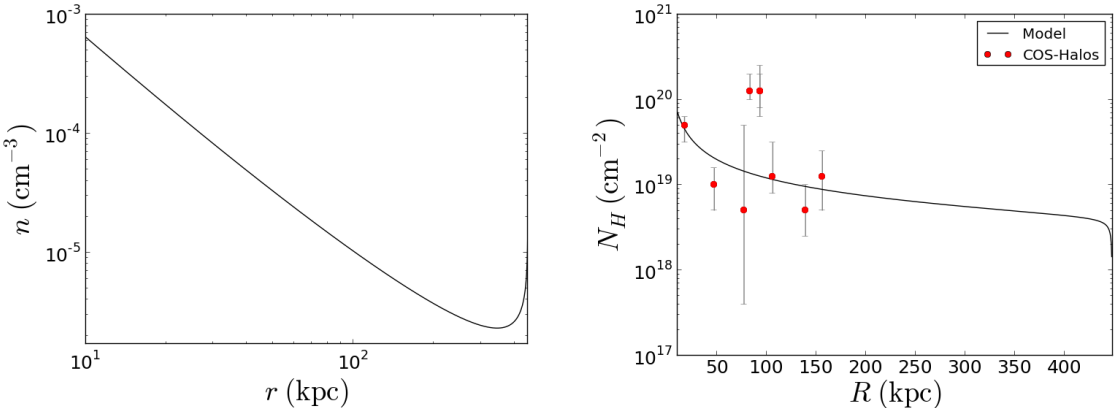

Figure 5.3: Left, CGM density, calculated using the continuity equation. Right, resulting projected density, compared with the COS-Halos observations.

The left panel of Figure 5.3 shows that if the CGM gas is made up by a population of clouds falling towards the centre, due to the continuity equation, the density is higher in the inner regions. The comparison of the observed column densities with our model (right panel) tells us that there is very good agreement between the model and observations. A population of infalling clouds has a projected density profile that is consistent with the observations, with $\chi^2_{N_H} = 2.5$.

5.1.2 Creation of the velocity distribution

In Chapter 4 we have performed several comparisons between the observed velocity dispersion and those derived from our models. The solutions of the Jeans equation, in fact, lead us to know only the velocity dispersion σ, without other information about the velocities of individual clouds. For this reason, in those models we have not considered the shape of the velocity distributions and we have focused only on the velocity dispersion. The situation changes for the infalling models presented in this chapter. In this case, our models predict the exact orbits of the clouds and in particular the radial profile of the infall velocity, given by equation (5.3). Therefore, we can make a more accurate comparison with the observations, by building "observed" velocity distributions from our models.
In order to "observe" our models we do not need the intrinsic velocity of a cloud, but its projection along the line of sight. The line-of-sight velocity of a cloud is related to the radial velocity by the equation:

$$v_{\rm los}(R) = v_r(r) \cdot \sin(\varphi) \ , \tag{5.7}$$

where φ is the angle shown in Figure 5.5 and $R = r \cdot \cos(\varphi)$.
The velocity profile is a function of the radius (see Figure 5.1), therefore, given a cloud at a specific intrinsic radius we know its velocity. To create the distribution of the line-of-sight velocities, associated to a given projected radius, we have to know how many clouds we expect at a specific intrinsic radius, as a function of the projected radius. If we observe along a specific line of sight, the probability to observe a cloud between two intrinsic radii r_1 and r_2 is given by the column density calculated between r_1 and r_2, divided by the total column density (the semi-column density, because we focus on the semi-interval, due to the simmetry of the system) at that projected radius. If we calculate it for every intrinsic radius, we obtain the following equation:

$$PDF(r) = \frac{\frac{\rho(r)r}{\sqrt{r^2-R^2}}}{I} \ , \tag{5.8}$$

where:

$$I = \int_R^{r_{\rm vir}} \frac{\rho(r)r}{\sqrt{r^2-R^2}} dr \ , \tag{5.9}$$

while *PDF* is the *Probability Density Function*, which describes the probability that a cloud is at a specific intrinsic radius, along a specific line of sight. We use this function to create random populations of clouds, represented in the left panel of Figure 5.4 by the blue histogram. The relative number of clouds at the different intrinsic radii is

given by the *PDF* (green line).

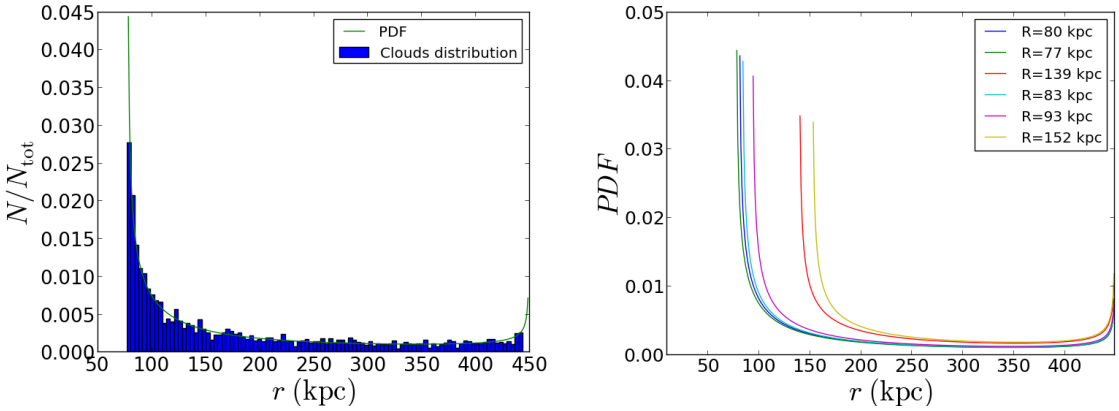

Figure 5.4: Left, the blue histogram represent a random population of clouds created for the line of sight correspondent to $R = 77$ kpc. The green line shows the PDF of this line of sight, calculated using equation (5.8). Right, the coloured lines represents the different *PDFs* calculated for 6 sightlines.

We create random populations of clouds as described above for the 12 projected radii corresponding to the observed radii (see Table 2.1). The probability distribution functions of some of the projected radii are shown in the right panel of Figure 5.4. The form of these curves is strongly dependent on the density distribution of our infall models, described by equation (5.6) and shown in the left panel of Figure 5.3. From the comparison of the *PDFs* in the right panel of Figure 5.4, we can see that, with this density distribution, when we observe a cloud along a projected radius, it is very likely that it is located at the same intrinsic radius, because the *PDF* assumes the highest values at this radius.
Finally, we put together all these clouds populations, weighted with the observed column densities, and since for each cloud we now know both the intrinsic and the projected radii, we can associate to each cloud a line-of-sight velocity, calculated using equation (5.7). For each line of sight, we created with the method described above two random populations of clouds, associating positive line-of-sight velocities to the first population and negative to the second, in order to simulate the approaching and the receeding motion of the infalling absorbers, as shown in Figure 5.5. The final result of this analysis is the line-of-sight velocity distribution of the model.

We applied the procedure described above to a variety of infall models, which are schematically summarized in Table 5.1 and which we will describe in more detail in the rest of this Chapter.

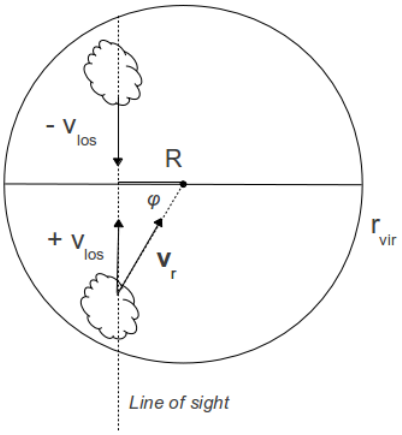

Figure 5.5: Simple diagram that explains the relation between the radial and the line of sight velocities.

Model		Drag	$M_{\rm cl}$ ($M_\odot$)	$M_{\rm cor}$ $M_{\rm bar}$	Pressure equilibrium	$r_{\rm ext}$	$r_{\rm int}$ (kpc)
Pure infall	1	OFF	/	/	/	$r_{\rm vir}$	0
	2	OFF	/	/	/	$r_{\rm vir}$	250
	3	OFF	/	/	/	160 kpc	0
Infall with drag	4	ON	10^8	0.5	OFF	$r_{\rm vir}$	150
	5	ON	5×10^6	0.1	OFF	$r_{\rm vir}$	220
	6	ON	3×10^6	0.1	OFF	$r_{\rm vir}$	10
	7	ON	10^6	0.1	ON	$r_{\rm vir}$	250
	8	ON	10^2	0.1	ON	$r_{\rm vir}$	10

Table 5.1: List of the parameters of our infall models. In particular we divide between pure infall models and models with drag, the latter being explored in Section 5.2.

5.1.3 Results

We first explore the results of model 1, describing a pure infall (i.e. due to the sole gravitational force) of the clouds from the virial radius towards the central galaxy. In this case the projected density profile is the one shown in the right panel of Figure 5.3 and is in agreement with the observed column densities. Therefore the first main constraint given by the COS-Halos observations is reproduced by this simple model. From this model, using the anlaysis described in Section 5.1.2 we obtained the velocity distribution in the right panel of Figure 5.6. This should be compared with the observed distribution, shown in the left panel. In the observations, $\Delta v_{\rm los}$ is the difference between the velocity of the clouds and the systemic velocity of the galaxy. In our models, it corresponds to the line-of-sight infall velocity.

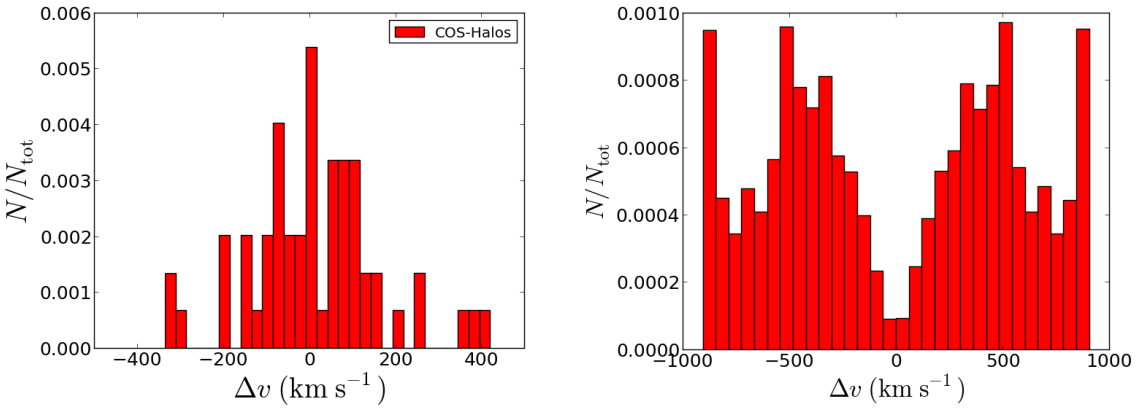

Figure 5.6: Left, observed velocity distribution. Right, velocity distribution of the CGM absorbers for the pure infall model 1.

We find a velocity distribution (right panel of Figure 5.6) with very high velocity values, spanning from -1000 km s^{-1} to 1000 km s^{-1}. From the observed distribution (left panel of Figure 5.6) we can see that the CGM clouds have lower velocities than what we expect from this model. More quantitatively, the model distribution has a standard deviation of 560 km s^{-1}, definitely inconsistent with the observed value $\sigma_{\rm obs} = 153$ km s^{-1} (the error on this value is $\delta_\sigma = 16$ km s^{-1}). Moreover, the shape of the two distributions in Figure 5.6 is completely different. The observed distribution has a symmetric and nearly gaussian form, while the distribution obtained with our model has a bimodal shape due to the lack of line-of-sight velocities with near-zero values. This can be understood on geometrical grounds, as illustrated in the left-hand panel of Figure 5.9. In the scenario considered here, clouds can only have a vanishing line-of-sight velocity if they are located at large projected radii ($R \sim r_{\rm vir}$). These large projected radii are however excluded here, because our model is tailored on COS-Halos

observations, which probed only much smaller projected galactocentric distances. On the other hand, we see several clouds with high line-of-sight velocities (blueshifted and redshifted) because their radial velocity forms a small angle with the line of sight. From the comparison between the two velocity distributions of Figure 5.6, we conclude that this simple pure infall model cannot explain the kinematics of the CGM in early-type galaxies, because its results are not in agreement with the observations.
To make an even more detailed assessment, in the two panels of Figure 5.7 we compare the line of sight velocities of the observations and of model 1, as a function of the projected radius. The two scatter plots are significantly different and in particular the model velocities (right panel) span, at each projected radius, a range of values much larger than the observations. We point out, hovewer, that for each line of sight we have a very low number of observed velocities and therefore this comparison may be not robust, due to the statistiscal fluctuactions. We also noticed that he observed line-of sight velocities in the left panel of Figure 5.7 also show an apparent trend with the projected radius. For low radii only positive velocities are observed, while the velocities at large radii are almost all negative. However, again due to low statistics, we cannot make firm claims about this trend.

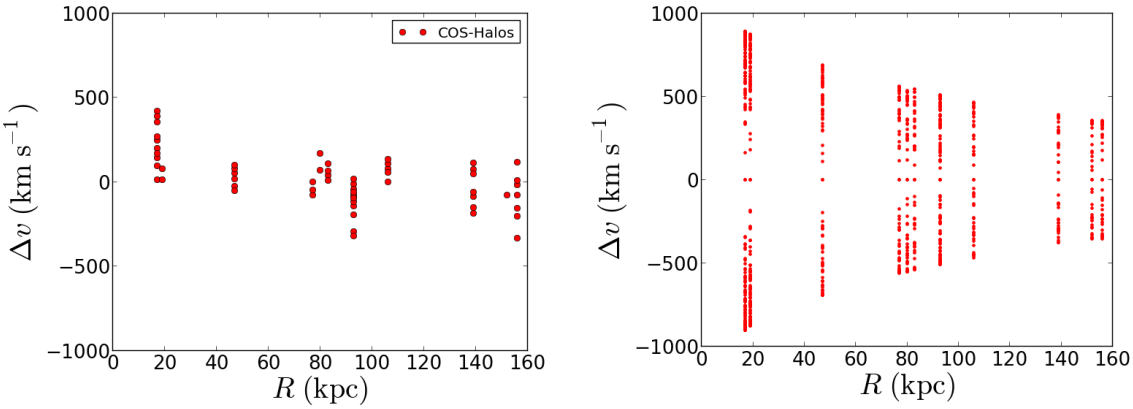

Figure 5.7: Line-of-sight velocities as a function of the projected radius. Left, observed velocities. Right, line-of-sight velocity of the pure infall model 1.

With the aim of finding a solution in better agreement with the observations, we probed, as we have done for the equilibrium models, the possibility that the absorbers do not fill the whole halo volume, but are confined to a specific region of the halo. This condition can change the velocity distribution of the system, making it more similar to the observed one.
We first explored models with an internal radius below which there are no absorbers: this could be due to the effects of the corona, as discuss in Chapter 3. We recall in fact that in the internal regions the drag time is small, due to the high densities of the hot

gas, and the interactions between the hot gas and the cold clouds are not negligible. In these regions, Kelvin-Helmoltz instabilities can destroy the cold absorbers, which is also supported by the results of our hydrodynamical simulations, as described in Section 3.3. We will treat with more accuracy the effects of the hot gas on the cloud infall motion in next section, introducing the drag force in the equation of motion.
In the left panel of Figure 5.8 we show the velocity distribution that we obtained for the pure infall model 2, in which the clouds fall from the virial radius towards the centre and disapear at 250 kpc. The projected density of this model is very similar to the one shown in Figure 4.11 of Chapter 4. With a large internal radius the projected density profile is nearly flat in the internal regions and in agreement with the observed densities. By comparing Figure 5.8 with Figures 5.7 and 5.6, we can notice that the effect of the internal radius is to decrease the range of observed velocities. The reason is that, in an infall model, the radial velocity assumes the highest values in the inner regions, as shown in Figure 5.1.

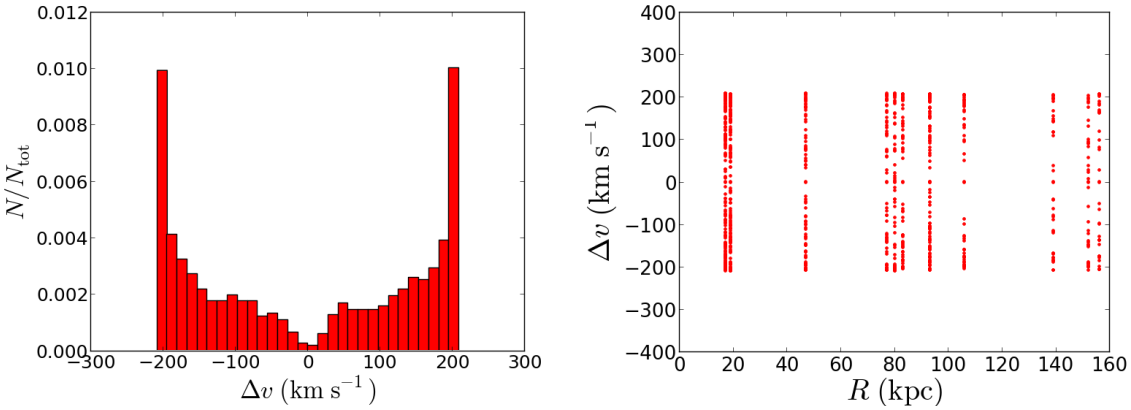

Figure 5.8: Left, line-of-sight velocity distrubtion for the pure infall model 2. Right, line-of-sight velocities of the same model plotted as a function of the projected radius.

The velocity distribution of pure infall model 2, shown in the left panel of Figure 5.8, has a standard deviation equal to 157 km s^{-1}, in agreement with $\sigma_{\rm obs}$. However, also in this case the distribution has a bimodal shape, completely different from the observed one (left panel of Figure 5.6), due to the same reasons explained above for model 1. In this case, the form is even worse (completely different from the observed one) than the previous one, because there is now only an external shell of infalling clouds, and we miss almost all the low line-of-sight velocities, as illustrated in right panel of Figure 5.9. In the right panel of Figure 5.8 we show also the model line-of-sight velocities as a function of the projected radius, to be compared with the observed velocities in the left panel of Figure 5.7 and we see that also these two distributions are different.

The incompatibility between the pure infall model 2 and the observed distribution led us to reject also this scenario. The observational constraints cannot be explained by a system of infalling clouds that disappear at a given radius.

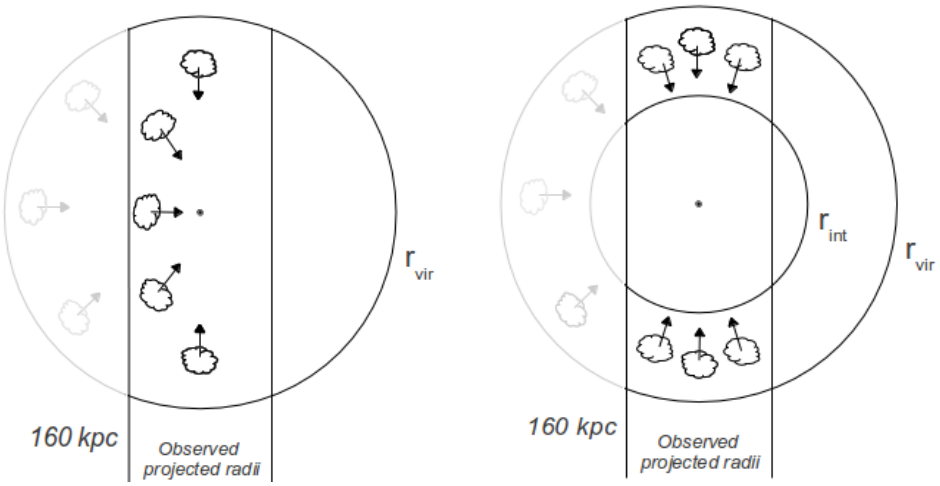

Figure 5.9: Simple diagrams that explain the bimodal shape of the velocity distributions of models 1 and 2, reported in Figures 5.6 and 5.8.

Finally, we explored the last possibility: CGM clouds could be created within the galaxy halo, at a radius smaller than the virial radius. In the previous models we were assumed the CGM to be accreted from the IGM and the cold clouds originated beyond $r_{\rm vir}$. However, cold clouds in ETG halos could form also from thermal instabilities of the hot gas (Field, 1965; Maller and Bullock, 2004). Binney et al. (2009) have shown that HI high velocity clouds could form, at radii larger than 100 kpc, by condensation of an isentropic galactic corona via thermal instability. In this scenario, we can expect cold clouds forming at large radii from the corona instabilities and then falling into the galaxy centre.
We simulated this possibility with the pure infall model 3, imposing that the clouds start falling with $v_{fall} = 0$ at a specific radius smaller than $r_{\rm vir}$. We adopted 160 kpc, which is the lowest possible choice, since we have observations out to this projected radius. This is an extreme case: the models where the clouds originated at radii between the virial radius and 160 kpc will have an intermediate behaviour between the distributions obtained from models 1 and 3 (Figure 5.10 and 5.6). Looking at the left panel of Figure 5.10 we note that the resulting velocity distribution of model 3 does not have a bimodal shape but rather a form more similar to the observed distribution. However, this is due to this specific choice of the external radius. This is because now, by constructions, clouds close to the observed edge have a vanishing line-of-sight velocity. If the external radius is larger than 160 kpc, the resulting velocity distribution

has again a bimodal shape. However, the standard deviation of the distribution in the left panel of Figure 5.10 is $\sim$ 400 km s^{-1}, much larger than the observed velocity dispersion. Moreover, the right panel of Figure 5.10 shows that model 3 predicts a stronger trend of the line of sight velocities with the projected radius than is present in the observations (Figure 5.7, left panel).
The above analysis shows that, with pure infall models with the only influence of the gravitational force of the halo, we cannot explain the CGM kinematics and densities constrained by the COS-Halos observations. Therefore we conclude that this is not a good description of the motion of the CGM clouds in early-type galaxies.

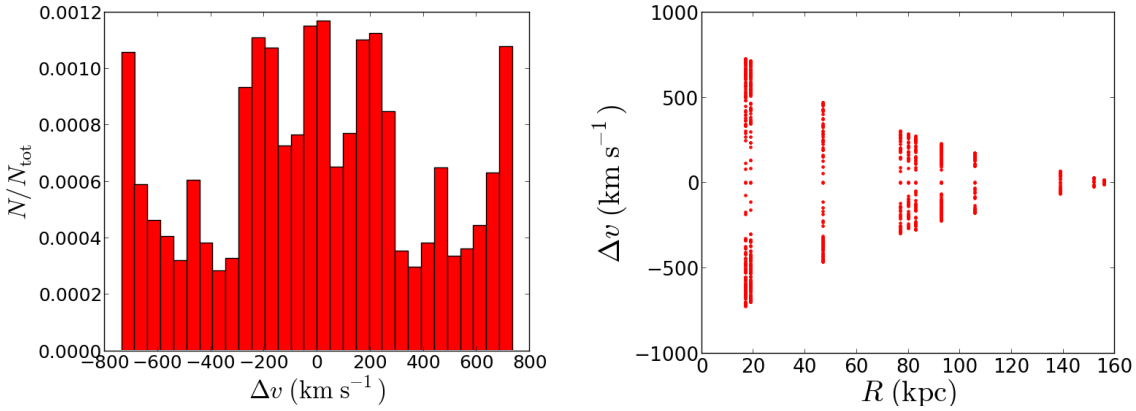

Figure 5.10: Left, line-of-sight velocity distrubtion for the pure infall model 3. Right, line-of-sight velocities of the same model plotted as a function of the projected radius.

5.2 Models with drag

In section 5.1 we have shown that, with the only influence of the gravitational force, infalling models are not able to reproduce the observed velocity distribution of the CGM clouds. In this section we improve our analysis by introducing the effect of the drag force: if the clouds are falling towards the centre of the halos they must be affected by the presence of the hot coronal gas. The interaction with the external medium changes the motion of the clouds. In particular the drag force will make the velocities lower than for the ballistic case, potentially reconciling them with observations.
To address this problem, we have solved the equation of motion of the clouds including the accelerations due to both the gravitational and the drag force. The latter acceleration term has the following form (Marinacci et al., 2011):

$$\dot{v}_{\rm drag} = \frac{A\rho_{\rm hot}v^2}{M_{\rm cl}} \ , \tag{5.10}$$

where $A = \pi R_{\rm cl}^2$ represents the cross section of a cloud, $M_{\rm cl}$ its mass, v the infall velocity and $\rho_{\rm hot}$ the density of the corona. For the coronal gas we used the same model described in Chapter 3 by equation (3.4).
The equation that we solved is:

$$\frac{dv}{dt} = -\frac{GM(r)}{r^2} + \frac{A\rho_{\rm hot}(r)}{M_{\rm cl}}v^2 \ , \tag{5.11}$$

where the first term in the second member is the gravitational force and $M(r)$ is the NFW profile described in Section 2.3.1.
Our goal is to find the velocity profile as a function of radius. Multiplying both members of equation 5.11 by $\frac{dt}{dr}$ we obtained:

$$\frac{dt}{dr}\frac{dv}{dt} = -\frac{dt}{dr}\frac{GM(r)}{r^2} + \frac{dt}{dr}\frac{A\rho_{\rm hot}(r)}{M_{\rm cl}}v^2 \ , \tag{5.12}$$

which leads to:

$$\frac{dv}{dr} = -\frac{1}{v(r)}\frac{GM(r)}{r^2} + \frac{A\rho_{\rm hot}(r)}{M_{\rm cl}}v(r) \ . \tag{5.13}$$

We solved this Ordinary Differential Equation numerically, using *scipy.integrate.odeint* from python, obtaining a radial velocity profile. As in section 5.1, we found the density distribution using the continuity equation and we created a line-of-sight velocity distribution using the same procedure described in Section 5.1.2.
We made this analysis for two sets of models, with two different assumptions. First we assumed that all the clouds have the same radius and density, equal to the observed values described in Chapter 3. In our second scenario we assumed instead pressure equilibrium between the clouds and the hot gas, with the densities and the radii of the clouds described by equation (3.5) and (3.6). Also in this second case all the clouds have the same mass. We investigated these two different scenarios becuase the physical state of the CGM absorbers is not very well observationally constrained (see Chapter 3) and we explored several models varying the cloud mass over a wide range, due to the large uncertainties on the cloud radii and densities (see Chapter 2). Moreover, we introduced also the internal radius as an additional parameter, because in Chapter 3 we have seen that the CGM clouds are destroyed by the interaction with the hot gas in the internal regions, by effects that are not included in the solution of equation (5.13) (e.g. Kelvin Helmholtz istabilities and thermal conduction). We created therefore several models varying the cloud mass and the internal radius.
For simplicity, we do not show here the dependence of our results on the variation of the

starting point for the clouds. For the following models, $r_{\rm ext} = r_{\rm vir}$, to investigate models with the clouds accreting from the IGM. Indeed, although COS-Halos observations have $R < 160$ kpc by construction, other works have found cold CGM absorptions out to the virial radius (see Chapter 6). Therefore we argue that it is not much justified to assume an external radius smaller than the galaxy virial radius. Moreover, we found that our results did not depend much on the variation of this parameter.

5.2.1 Drag models with observed densities

We show in this section the results obtained for the motion of the infalling clouds with a constant density equal to the observed value. With this assumption, using equation (3.6) to relate the radius and the mass of the clouds, we can rewrite equation (5.13) as:

$$\frac{dv}{dr} = -\frac{1}{v(r)}\frac{GM(r)}{r^2} + \left(\frac{3}{4\rho_{\rm cl}}\right)^{2/3} \pi^{-1/3} M_{\rm cl}^{-1/3} \rho_{\rm hot}(r) v(r) \ . \tag{5.14}$$

where $\rho_{\rm cl} = 1.4 n_H m_{\rm p}$, with $n_H \sim 7 \times 10^{-4}$ cm^{-3}, is the constant observed cold CGM density (see Section 3.1). We consider two different types of coronae, both described by equation (3.4), but with a total mass equal to either 10 % or 50 % of the total theoretical baryonic mass associated with the halo (see Section 3.2).
We investigate models with different assumptions of the clouds mass, to assess the effects of the drag on clouds with different properties. We explore models with clouds masses that vary from 10^2 to 10^8 M$_\odot$, imposing in this way a variation of the clouds radius from 0.1 to 10 kpc (see Figure 5.11).

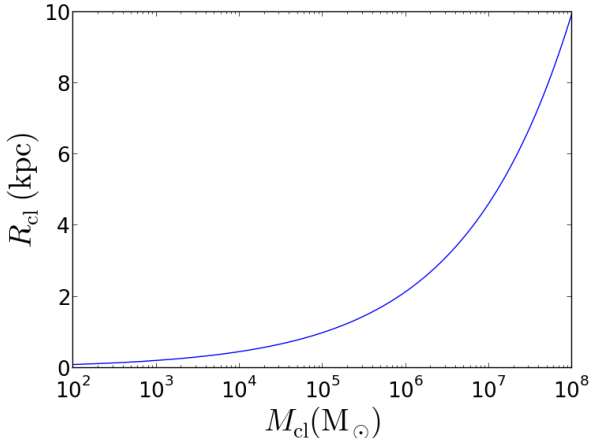

Figure 5.11: Cloud radius plotted as a function of the cloud mass.

We vary also the internal radius $r_{\rm int}$. We assume that these clouds cannot survive for the entire infall time towards the halo centre (see Chapter 3), which is particularly likely assuming very low densities, which are out of pressure equilibrium with the corona.

Results

In Figure 5.12 we report the two colormaps for our first main diagnostic $\Delta\sigma_{\rm obs}$ (see Chapter 4) as a function of the cloud mass and the internal radius, for a corona with $M = 0.1 M_{bar}$ (left map) and $M = 0.5 M_{bar}$ (right map). To evaluate $\Delta\sigma_{obs}$ we calculate the standard deviation of the final velocity distribution (see Section 5.1.2) of each model. The maps of Figure 5.12 show that if the clouds mass is too low, the variance obtained from our models is not consistent with the observed one, for every choice of the internal radius. The drag influence of the hot gas is in stronger on clouds with low masses, with the result that they are slowed down by the drag force to velocities that are too small compared with the observed ones. This effect is even more evident in the right map, where a more massive and therefore denser corona is considered. In this model, to obtain a velocity dispersion consistent with observations, the mass of the clouds must be larger than 10^7 $M_\odot$. In the left map, instead, where we evaluate the effects of a more diffuse corona, we have the best results for clouds with $M > 10^5$ $M_\odot$. Regarding the internal radius, we obtained values of $\Delta\sigma_{obs}$ lower than 3 with $r_{\rm int} < 300$ kpc. Therefore, the clouds must survive at least until they reach that radius for the results to be compatible with the observations.

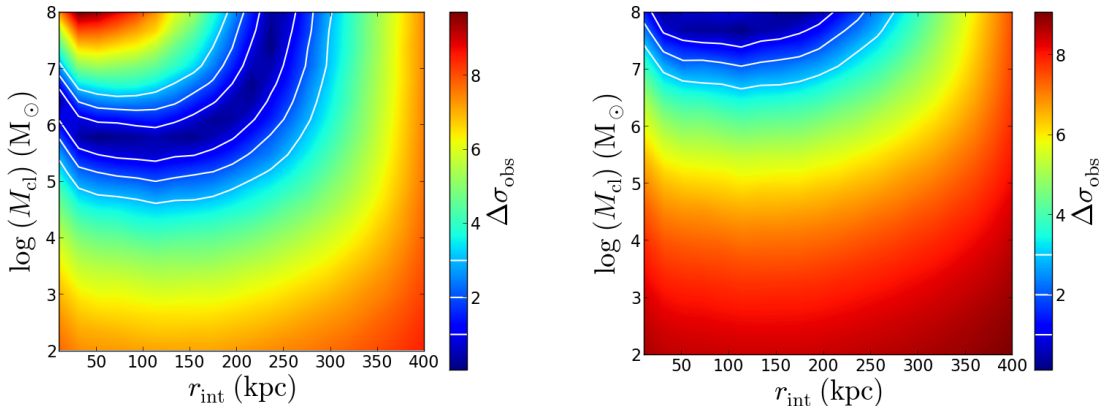

Figure 5.12: Quantitative comparison between model predictions and observed properties of the CGM of ETGs, in terms of velocity dispersion (see equation (4.13) in Chapter 4) for a model describing the infall of clouds with the observed densities towards the central galaxy, with the influence of the drag acted by a hot corona with mass $M_{\rm cor} = 0.1 M_{\rm bar}$ (left panel) and $M_{\rm cor} = 0.5 M_{\rm bar}$ (right panel). The contours are placed at 1, 2 and 3.

In addition to the maps of Figure 5.12, in the two panels of Figure 5.13 we show the

different effects of the drag (with the two assumptions for the mass of the corona) on the infall velocity radial profiles of the clouds. As for the colormaps, high mass clouds show the larger velocities and the influence of the corona isstronger if the hot gas is denser. In these plots, the internal radius is marked by the vertical dashed-line.

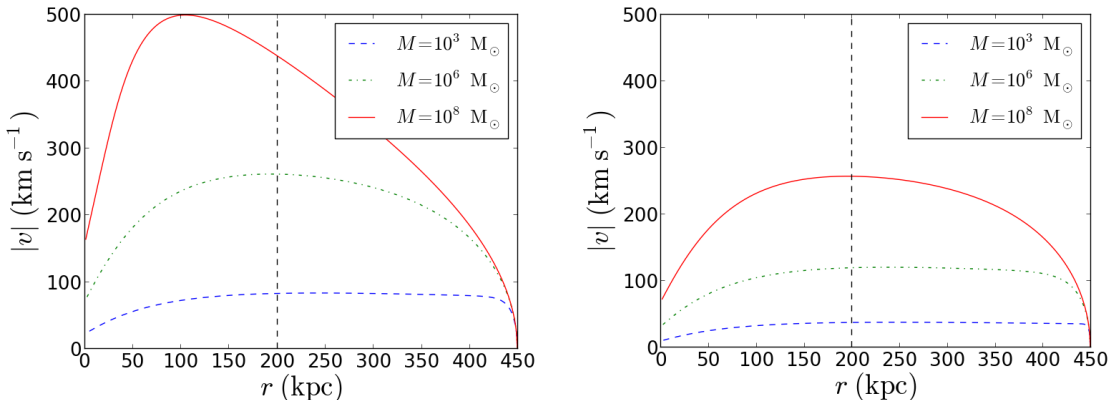

Figure 5.13: Radial profiles of the infall velocities for models with drag and clouds with a constant density, using three different assumption for the cloud mass: $M_{\rm cl} = 10^3, 10^6, 10^8$ M$_\odot$. Left, with $M_{\rm cor} = 0.1 M_{\rm bar}$. Right, with $M_{\rm cor} = 0.5 M_{\rm bar}$. The vertical dashed-line marks $r_{\rm int} = 200$ kpc

The analysis of the standard deviations of the velocity distributions shows that there are models in agreement with the observations. Remarkably, these models also reproduce the projected density profiles. This is shown by Figure 5.14, where we evaluate our second main diagnostic for the goodness of our models, χ^2_{NH} (equation 4.14). The value of the reduced chi square is about 3 in the whole parameter space and therefore the densities of our models are always roughly consistent with observations.

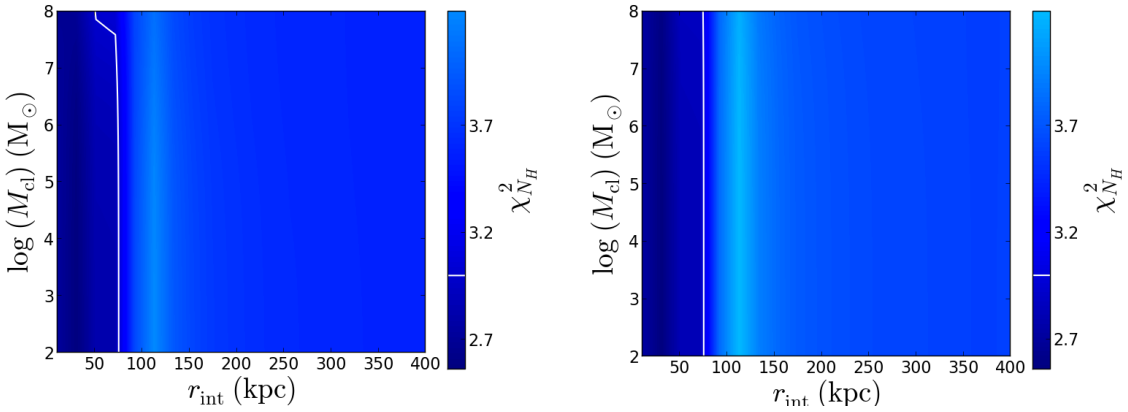

Figure 5.14: Similar to Figure 5.12, but in terms of the column density (see equation (4.14)). The countours are placed at $\chi^2_{NH} = 3$.

Finally, using equation (5.4), we calculate the infall time, with the inferior and the superior limits of the integral given respectively by $r_{\rm vir}$ and $r_{\rm int}$. The two maps obtained are shown in Figure 5.15. The contours are located at 2 and 3 Gyr. Through the comparison with the maps of Figure 5.12 we see that, in all the satisfying models, the clouds fall from the virial to the internal radius in less than 3 Gyr.

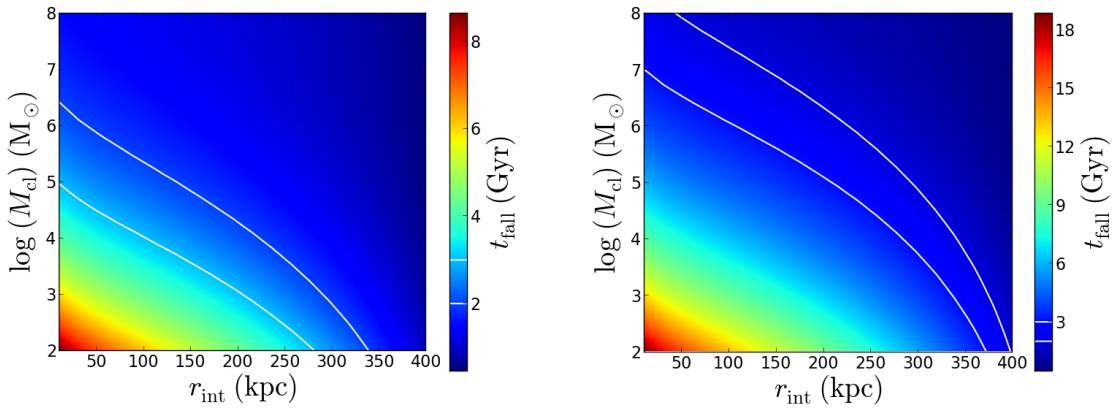

Figure 5.15: Similar to Figure 5.12, but in terms of the infall time (equation (**??**). The countours are placed at 2 and 3 Gyr.

Let us now investigate three of the models with the expected standard deviation, with values within the error δ_σ from the observed velocity dispersion ($\sigma_{\rm obs} = 153$ km s^{-1}). These are the models 4, 5 and 6 described in Table 5.1. In Figure 5.16 we report the line-of-sight velocity disributions of the models 4 and 5, with $M_{\rm cl} = 10^8$ M$_\odot$, $r_{\rm int} = 150$ kpc and $M_{\rm cor} = 0.5 M_{\rm bar}$ (left panel), and with $M_{\rm cl} = 5 \times 10^6$ M$_\odot$, $r_{\rm int} = 220$ kpc and $M_{\rm cor} = 0.1 M_{\rm bar}$ (right panel). The two distributions reveal that the predictions of these two models are not consistent with the observations. As for the ballistic models, there is indeed a lack of velocities with near-zero values and the two distributions are completely different from the observed one, shown in the left panel of Figure 5.6. If there is a large internal radius, the infall models with drag (and clouds with constant densities) lead to a velocity distribution not consistent with the observations.
In the left panel of Figure 5.17 instead we show the resultant velocity distribution of model 6, with $M_{\rm cl} = 3 \times 10^6$ M$_\odot$, $r_{\rm int} = 10$ kpc and $M_{\rm cor} = 0.1 M_{\rm bar}$, which minimizes again the value of $\Delta\sigma_{\rm obs}$, but has a small internal radius, different to the two previous models. In this case the velocity distribution reveals a shape different from the one of Figure 5.16. It is in fact more similar to the observed velocity distribution and the only clear difference is represented by the central hole at very low line-of-sight velocities. Without the central hole, this distribution would be consistent with the observed one. A possible explanation for to this lack of small velocities could be related to our implementation of the internal radius. Indeed, we are considering with our models

that the clouds suddenly disappear when they pass through the internal radius and this extreme approximation of the cloud destruction influences also the final velocity distribution. In a more realistic scenario, the velocity of the clouds is strongly reduced before their destruction. Therefore, the low velocities missing in our distribution could be recreated by a more thorough analysis.

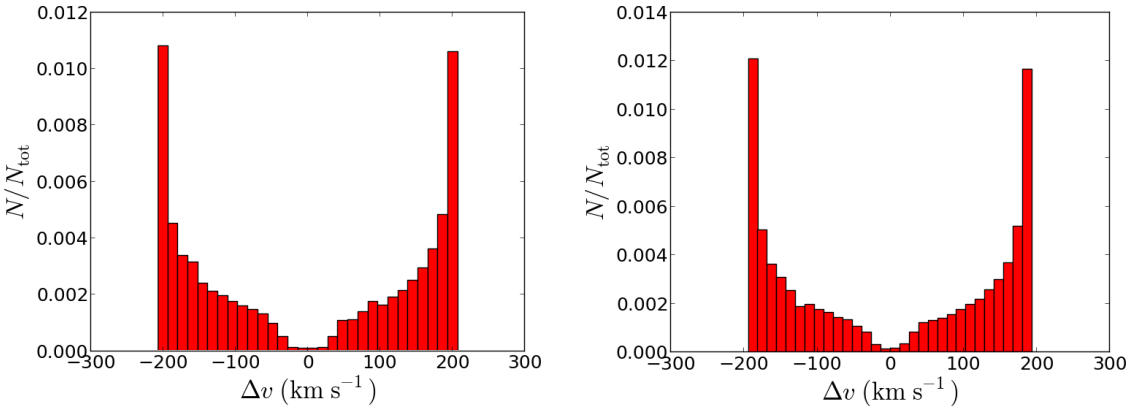

Figure 5.16: Line-of-sight velocity distributions resulting from models 4 (left panel) and 5 (right panel)

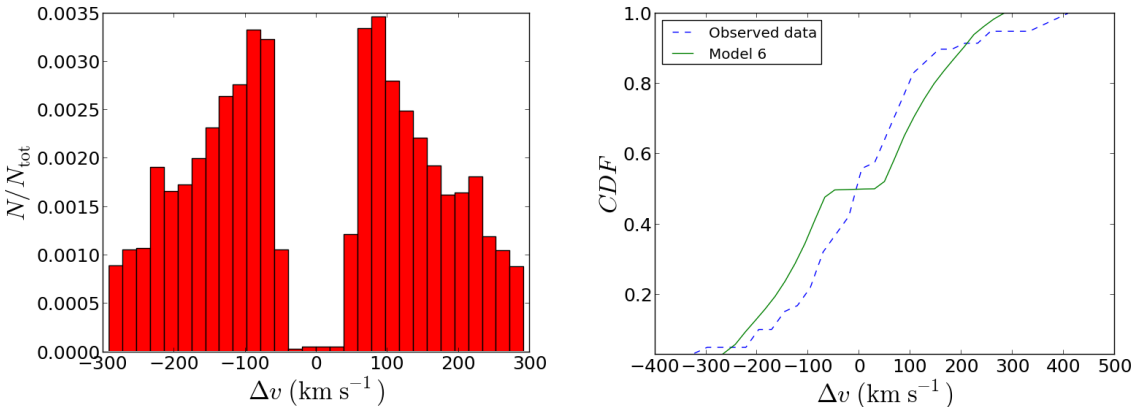

Figure 5.17: Left, line-of-sight velocity distribution resulting from model 6. Right, comparison of the cumulative distribution function of the the same model with the observed one.

In order to make a more rigorous comparison between the distribution shown in the left panel of Figure 5.17 with the observed one, we performed a Kolmogorov-Smirnov test, which compares the two *Cumulative Distribution Functions*, shown in the right

panel of Figure 5.17. This test gave us an extremely low value, which means that the two distributions are not consistent whith each other[1]. Nevertheless, due to the considerations above, we consider the model 6 our preferred one in reproducing the COS-Halos observations of the cold CGM. With a more rigoruos characterization of the clouds destruction, an infall model with drag could explain the kinematics of the CGM clouds in early-type galaxies.

5.2.2 Drag models with pressure equilibrium

In this section we show how our results change if we assume the presssure equilibrium between the CGM clouds and the hot corona. Indeed, a cloud out of pressure equilibrium, as the one studied in the previous section, is not pressure supported and its fate is then to contract in a crossing time, to reach the pressure equilibrium with the ambient medium (McCourt et al., 2016). We can estimate the crossing time of a typical CGM cloud through equation:

$$t_{\rm cross,cl} = \frac{R_{\rm cl}}{c_{\rm s,cl}} \ , \tag{5.15}$$

where $R_{\rm cl}$ is the cloud radius and $c_{\rm s,cl}$ is the sound speed of the cloud (see equation (3.2)).

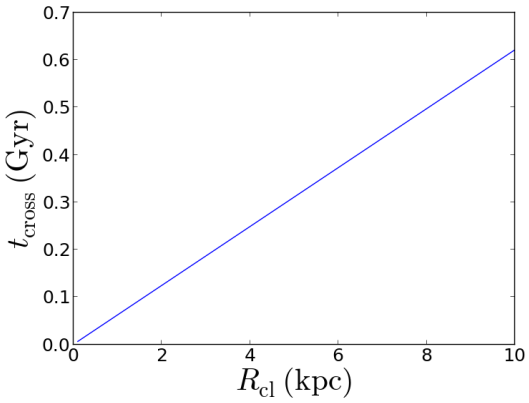

Figure 5.18: Variation of the cloud crossing time as a function of the cloud radius.

In Figure 5.18 we show the variation of the cloud crossing time with the cloud radius, exploring the same range of radii investigated in the previous section (from 0.1 to 10 kpc). Note that the crossing time is always less than 0.7 Gyr, even for the largest

[1]We obtained the same result for all the infall models of this chapter. The K-S test rejects all our models.

cloud. By the comparison of Figures 5.12 and 5.15 instead, we can see that in our satisfactory models the clouds usually reach the internal radius in their infall motion in ~ 2 Gyr. Therefore, we conclude that the clouds likely reach the pressure equilibrium during their infall towards the central galaxy and that it is useful to investigate also this scenario.
In this section we use in particular the same assumptions made in Section 3.2 of Chapter 3. All the clouds have therefore the same mass and their densities and radii are described respectively by equations (3.5) and (3.6). With these conditions, we can rewrite equation (5.13) as:

$$\frac{dv}{dr} = -\frac{1}{v(r)}\frac{GM(r)}{r^2} + \pi^{-1/3}\left(\frac{3T_{\rm cl}}{4T_{\rm hot}}\right)^{2/3} M_{\rm cl}^{-1/3}\rho_{\rm hot}^{-1/3}(r)v(r)\ . \tag{5.16}$$

where $T_{\rm cl} = 2 \times 10^4$ K and $T_{\rm hot} = 10^7$ K, are respectively the cold CGM and the corona temperatures. In this scenario, we assume a hot gas mass equal to 10 % of the total baryonic mass, consistent with our discussion of Chapter 3. We have seen indeed that with a diffuse corona, if the absorbers are concentrated in the external regions of the halos, the densities inferred by the pressure equilibrium with the hot gas can be comparable to the observed ones. We explore models in the same parameter space described in the previous section, varying the clouds mass and the internal radius. The variation of the cloud radii depends on the cloud mass and the galactocentric radius and it can be seen in Figure 3.4. The physical reason for the existence of an internal radius derives from the conclusions of Section 3.3: in the internal regions, where the corona is denser, the clouds are destroyed by the interactions with the hot gas, by effects that are not described by our analytic models (e.g. Kelvin-Helmholtz instability and thermal conduction).

Results

In Figure 5.19 we report the maps for our two main diagnostics: $\Delta\sigma_{\rm obs}$, which evaluates the dicrepancy between the observed velocity dispersion and the standard deviation of the model distribution (left panel) and $\chi^2_{N_H}$, which evaluates the goodness of a model in terms of the projected densities (right panel). The right map reveals that, as for the previous models, the projected densities are in good agreement with the observations in the whole parameter space. The left map instead shows that, at variance with the models of the previous section, there are models in agreement with the observed variance with any choice of the cloud mass, depending on the internal radius. Models with small cloud masses have low values of $\Delta\sigma_{obs}$ for small internal radii, while if the cloud mass is larger than $\sim 10^5$ $M_\odot$, the internal radius has to be at least ~ 200 kpc.

The left panel of Figure 5.20 shows the difference between the radial velocity profiles of

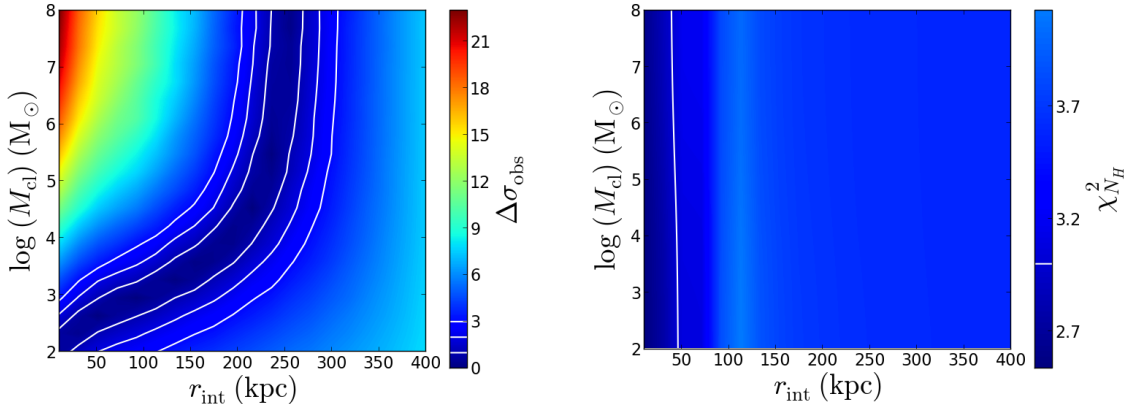

Figure 5.19: Similar to Figure 5.12, but in terms of the velocity dispersion (left panel, see equation (4.13)) and of the column density (right, panel, see equation (4.14)), for an infall model with drag and the clouds in pressure equilibrium with the hot corona.

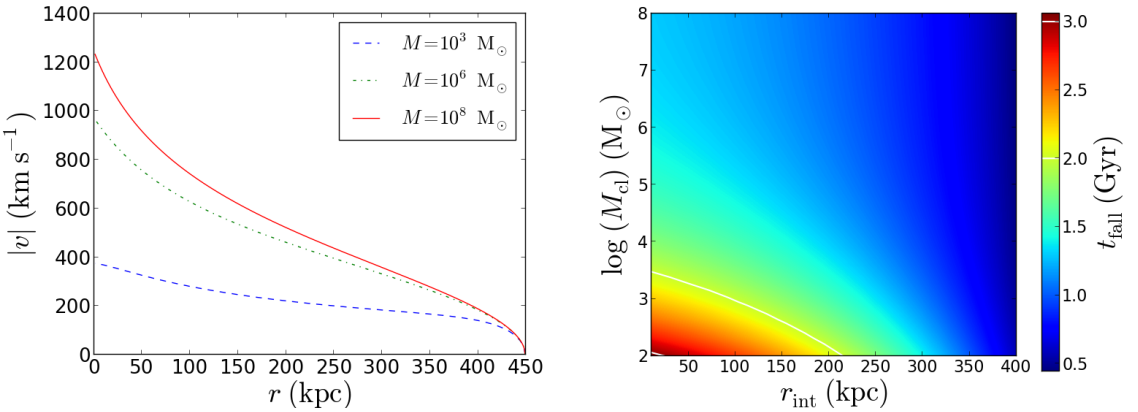

Figure 5.20: Left, radial profiles of the infall velocities for models with drag and the pressure-equilibrium assumption, using three different assumption for the cloud mass: $M_{\rm cl} = 10^3, 10^6, 10^8$ $M_\odot$. Right, similar to Figure 5.19, but in terms of the infall time (eqaution (5.4)).

clouds with different masses. The velocities decrease for small masses, as in Figure 5.13. However with the assumption of pressure equilibrium the velocities do not decrease in the internal regions. This is because the cold gas density also increases in these regions, as for the hot gas (see the left panel of Figure 3.2). Therefore, for clouds of any mass, the velocity increases with decreasing galactocentric radius. In the right panel of Figure 5.20 we report instead the colormap of the infall times: also in this case, for almost all our models the clouds fall from the virial to the internal radius in less than 3 Gyr.
As for the previous models with drag and clouds with a constant density, we analyse more in detail the velocity distribution of models with the expected dispersion. We show in Figure 5.21 the final line-of-sight velocity distributions of models 7 and 8 of Table 5.1, with $M_{\rm cl} = 10^6$ M$_\odot$ and $r_{\rm int} = 250$ kpc (left panel), and with $M_{\rm cl} = 10^2$ M$_\odot$ and $r_{\rm int} = 10$ kpc (right panel). The two distributions also in this case have a bimodal shape and are different from the observed one, shown in Figure 5.6 (left), in particular the distribution of model 7, which has a large internal radius. Also for the results of these models the considerations made at the end of Section 5.2.1 on the destruction of the clouds are valid. With a more accurate description of this phenomenon, the final velocity distribution might change. In particular the distribution of model 8 is relatively more similar to the observed one. However, as we have seen in Chapter 3, with the pressure-equilibrium assumption the clouds have to be confined in the external regions to reproduce densities consistent with the observations. Therefore, with this assumption, it is unlikely that the clouds reach small internal radii with their infall motion.

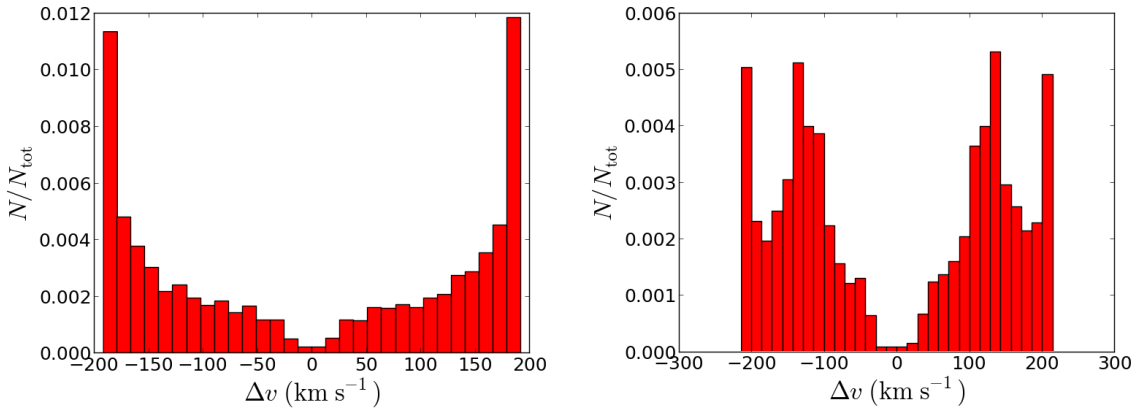

Figure 5.21: Line-of-sight velocity distributions resulting from models 7 (left panel) and 8 (right panel)

We conclude that also our model with drag and pressure equilibrium does not reproduce the COS-Halos observations, although we do not exclude that better results will be

obtained with future work, with the implementation of a more thorough description of the cloud destruction.

5.3 Conclusions

In this chapter we studied the kinematics of the CGM in early-type galaxies under the assumption that the clouds are falling in the halos of the galaxies either coming from the IGM or being formed in the hot halo by thermal instabilities. We analysed in detail a wide variety of models, considering very different physical assumptions and exploring a large range of parameters. Comparing the results with the observations of the COS-Halos collaboration, we find that no one of our models satisfactory reproduces the observational features. In particular, a population of clouds that is falling into the centre of the galaxies is not able to reproduce all the details of the observed velocity distribution, even if the effects of the drag force on the dynamics of clouds are taken into account. However we still cannot entirely discard infall models and we identified some subtle hydrodynamical effects which could potentially lead to improvements in future investigations. Our most promising result is found for clouds infalling from the IGM down to the central galaxy, with a constant density close to values suggested by observations that fall from the virial radius to small internal radii and are progressively slowed down by the effect of the drag. A more thorough assessment of this model, however, would require a detailed modeling of the kinematics of clouds just before disruption, which is left for future investigation.

Chapter 6

Discussion and conclusions

In this thesis, we have investigated the kinematics of the cold CGM clouds in early-type galaxies, whose properties have been estimated by the COS-Halos collaboration (Tumlinson et al., 2013; Werk et al., 2013; Werk et al., 2014). In this final chapter, we discuss some fundamental points of our work and we summarize our main conclusions. In particular, in Section 6.1 we focus on the comparison between our results and current observations of the CGM at large radii, obtained by other teams. In Section 6.2 we discuss the physical assumptions of our models, with some implications of our results regarding the cloud origin and survival. Finally, in Section 6.3 we outline our main conclusions and our future perspectives.

6.1 Comparison with other data

Throughout this Thesis we have compared the results of our models with the observations of the COS-Halos collaboration (explained in detail in Chapter 2) for the cold CGM in early-type galaxies. In particular, we have focused on the velocity distribution of the absorbers and on the trend of the total hydrogen column densities. A characteristic of the COS-Halos observations is that the considered impact parameters (the projected distance of the quasar sightline from the associated galaxy) are, by construction, always smaller than 160 kpc. Therefore we have focused in particular on the results of our models in this range of projected radii. However, in Chapter 4 we have seen that our equilibrium models make predictions also for the CGM density out to the virial radius. All our satisfactory models have their clouds confined in the outer regions of the halo and produce, under projection, a flat column density profile, in agreement with COS-Halos observations in the considered range of projected radii. These profiles remain flat also out to larger projected radii, as shown by Figures 4.8 or 4.17 (left) and it would be very useful to compare them to data extending out to the virial radius. Moreover, all the acceptable models have a strong tangental anisotropy, which results

in distinct predictions on the line-of-sight velocity dispersion profile. From the comparison of the two panels of Figure 4.22 we have seen that the anisotropic models have the largest line-of-sight velocity dispersions at large projected radii, which could be probed only by observations reaching projected radii as large as the virial radius. The aim of this section is to compare these predictions with some observational indications in this radial range.
Huang et al. (2016) observed chemically enriched cold gas around massive quiescent galaxies, through detections of MgII absorption features. Their results are based on a survey of 37 621 luminous red galaxy (LRG)-QSO pairs in SDSS DR12 with projected separation $d < 500$ kpc. Therefore, this study is a potentially important source of information about the cold CGM in early-type galaxies out to the virial radius. The 13% of the whole sample is composed by galaxies that show OII emission, indicating star formation processes. Here we do not consider this subsample and we focus only on the observations of the passive galaxies. In Figure 6.1 we report two of the main results of this work.

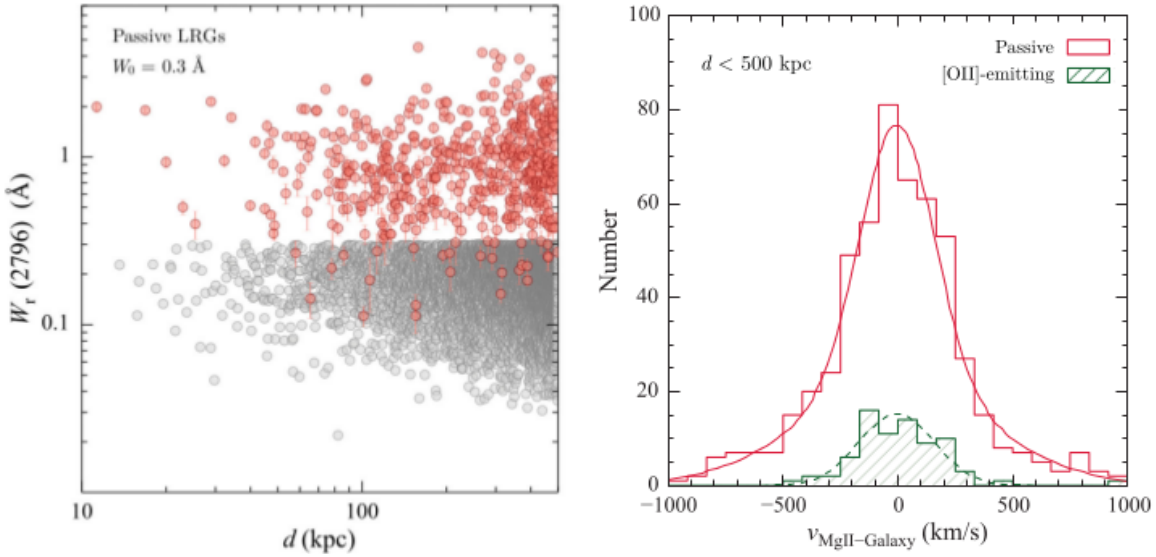

Figure 6.1: Left, rest-frame absorption equivalent width of the 2796 Ä member of the MgII absorber, as a function of the projected distance. LRGs with detected MgII absorbers are shown in filled circles with error bars representing measurement uncertainties. The grey circles indicate the 2σ upper limits of the non detections. Right, velocity distributions of MgII absorbers with respect to the systemic velocity of the LRG. In green is shown the velocity distribution of the OII emitting galaxies, correspondent to the 13% of the total galaxy sample (from Huang et al., 2016).

In the left panel of Figure 6.1 the rest-frame absorption equivalent width of the MgII absorbers is shown as a function of the projected radius. Note that there is a strong

presence of absorbers also at large radii and that the value of the measured equivalent width remains nearly constant with radius. This trend could be consistent with our findings for the CGM column density at large radii. On the other hand, Zhu et al. (2014), who analysed stacked spectra of QSOs to look for absorption lines of the cold CGM around luminous red galaxies, found a decreasing profile of the mean absorption equivalent width (and of the MgII surface density) with the projected radius[1]. Therefore, from this comparison, it is not clear whether our model predictions for the column densities could be consistent or not with observations at large radii.
The right panel of Figure 6.1 shows in red the relative line-of-sight velocity distribution of the MgII absorbers around the passive galaxies in the sample of Huang et al. (2016), with respect to the galaxy systemic velocity. This distribution has extended high-velocity wings and is best represented by a double gaussian, with a narrow component having $\sigma = 163$ km s^{-1} and a broad component having $\sigma = 415$ km s^{-1}, with the 12% of the total number of absorbers having $|\Delta v| > 500$ km s^{-1}. Note that the σ of the narrow component is consistent with the value found in Section 2.3 for the dispersion of the velocity distribution of the COS-Halos CGM absorbers in ETGs (153 ± 16 km s^{-1}). This is the value reproduced by our satisfactory collisionless models. Moreover, the detection of a number of absorbers at high velocity could be consistent with the predictions of our anisotropic models. Indeed, we have seen (Figure 4.22, right) that these models predict high line-of-sight velocities at large radii, because of the effect of the tangential anisotropy.
Therefore, from this first comparison, we can conclude that our equilibrium models could be in agreement also with observations at large projected radii. Our future perspectives are to build-up more thorough models with the implementation of these additional observational constraints and also compare these with our non-equilibrium models.

6.2 Origin and survival of the CGM clouds

6.2.1 Cloud origin

With our work, we have investigated dynamical and hydrodynamical models to explain the behaviour of cold CGM clouds in early-type galaxies. There are two possibility for the formation of the clouds that are both consistent with our findings. First, the CGM clouds could have an external origin and be accreted from the IGM. In this scenario the clouds could assume an equilibrium configuration after they enter into the galaxy haloes (described by the equilibrium models of Chapter 4), or could fall towards the central galaxy until they are destroyed by the interactions with the hot

[1] Chen (2016) pointed out that the difference between the two results could be due to the fact that Huang et al. (2016) observe single absorbers, while Zhu et al. (2014) used stacked spectra.

gas. In a second scenario, the clouds could originate at large galactocentric radii from the thermal instabilities and condensation of the hot coronal gas (Maller and Bullock, 2004; Binney et al., 2009) and then either fall towards the centre or arrange themselves in a dynamical equilibrium state, subject to the constraints described in Chapters 4 and 5. Therefore, we conclude that with our work we cannot exclude none of these two possibilities for the origin of the cold CGM in early-type galaxies. Further clues may however come from the comparison of our models with extended samples like the one described in Section 6.1

6.2.2 Cloud survival

In Chapter 3 we have investigated, using hydrodynamical simulations, the survival of cold clouds in the hot haloes of early-type galaxies. We have explored the cloud motion in the internal and in the external regions of these haloes, assuming different densities for the hot coronal gas. We have found that the cold CGM absorbers behave like bullets in the outer regions, where the hot gas is diffuse and has a small influence on the cloud motion. Instead, we have found that in the internal regions the clouds are destroyed by the interaction with the denser corona. Our collisionless models, described in Chapter 4, are in agreement with these findings. Indeed we have found that to satisfactorily reproduce the observations the clouds must be concentrated in the external regions, naturally confined by their tangentially biased orbits. To include cloud destruction in our analytic non-equilibrium models instead, in Chapter 5 we have introduced as an additional parameter an internal radius, below which clouds are unable to penetrate. Thus, it appears that an internal region devoid of clouds is very likely present in ETGs.
The existence of an internal radius would also solve the paradox of the large accretion rate from the IGM versus a negligible star formation rate in the central galaxy. We can give an estimate of this accretion rate, using the value found by Werk et al. (2014) for the CGM mass ($M_{\rm CGM} = 1.2 \times 10^{11}$ M$_\odot$) and our estimate of the infall time (in Chapter 5 we have found that in all the models that reproduce the observations, the infall time is less than 3 Gyr), through equation:

$$\dot{M}_{\rm CGM} = \frac{M_{\rm CGM}}{t_{\rm fall}} = \frac{1.2 \times 10^{11}\ {\rm M}_\odot}{3\ {\rm Gyr}} = 40\ {\rm M}_\odot\ {\rm yr}^{-1}\ . \tag{6.1}$$

In general, early-type galaxies are nearly devoid of cold gas and we consider $\sim 10^9$ M$_\odot$ an upper limit on its mass (Davis et al., 2011; Young et al., 2011; Serra et al., 2012). If the large reservoir of cold CGM were accreted and accumulated at the estimated rate in the central galaxy, the observed value of cold gas would have been reached in less than 30 Myr. Therefore we exclude the possibility of accumulation of cold gas in the central galaxy. Another possibility is that all the accreted cold gas fuels star formation

in the galaxy. However, the observed star formation rate of passive early-type galaxies (see Table 2.1 in Chapter 2) is much lower than our estimated rate from equation (6.1). We conclude that the cold CGM clouds cannot reach the central ETGs, because this would be inconsistent with observations. Therefore, cloud destruction is necessary for infall models to be consistent with the observed properties of ETGs.

6.3 Conclusions and Future perspectives

In this Thesis work we have investigated cold CGM clouds in early-type galaxies with a wide variety of models, in order to describe their physical state and kinematics and improve the current understanding of this elusive gas phase. Here we summarize our main results:

1. we have found that cold clouds ($T < 10^5$ K) can survive to interactions with their environment only in the outer regions of galaxy haloes, while they are destroyed in the internal regions due to the hydrodynamical interaction with the hot coronal gas. Moreover, in the external regions the motion of massive clouds can be treated as nearly ballistic, because the drag time is larger than the dynamical time of the system and the interactions between hot gas and cold clouds are weak (Chapter 3);

2. we have found that collisionless isotropic equilibrium models cannot simultaneously reproduce the kinematics and the densities observed by the COS-Halos collaboration (see Chapter 2). We have found, however, that collisionless anisotropic models can succesfully describe both observational constraints. In particular our satisfactory models require the clouds to be confined to the external regions of the halo, at hundreds of kiloparsecs from the central galaxy, with tangentially biased orbits (Chapter 4);

3. finally, we have investigated non-equilibrium models that describe the inflow of cold clouds accreted from the IGM or produced in the outer corona via thermal instabilities. We have explored several models, considering very different physical assumptions and parameters, and we have found that the most successful models in reproducing the observations are constituted by infalling clouds with densities consistent with observations (non in pressure equilibrium with the corona), slowed down by the effect of the drag (Chapter 5).

To conclude, with this thesis work we have found some kinematics models that succesfully explain the motion and the physical state of the CGM absorbers in early-type galaxies. We plan however to improve these results with future investigations, as explained throughout this thesis. In particular, we aim to focus on two main points that will be critical to confirm our results and conclusions:

- compare our models with new observations at larger projected galactocentric distances (see Section 6.1), in order to confirm our predictions close to the virial radii of galaxy haloes;
- improve our modelling of cloud infall, interaction of the corona and cloud disruption with the implementation of more complex hydrodynamical effects that we have neglected for simplicity in our models of Chapter 5.

Finally, we plan to extend our analysis to the CGM of the star-forming galaxies. In conclusion, with this work we have found different scenarios to describe in a coherent way the kinematics and densities of the circumgalactic medium and we plan to also improve our results with future investigations, in order to understand the origin and fate of the CGM, that is one of the most important challenges of the modern astrophysics.

Bibliography

C. Allende Prieto, P. S. Barklem, M. Asplund, and B. Ruiz Cobo. Chemical Abundances from Inversions of Stellar Spectra: Analysis of Solar-Type Stars with Homogeneous and Static Model Atmospheres. *Astrophysical Journal*, 558:830–851, September 2001.

M. E. Anderson and J. N. Bregman. Detection of a Hot Gaseous Halo around the Giant Spiral Galaxy NGC 1961. *Astrophysical Journal*, 737:22, August 2011.

M. E. Anderson, J. N. Bregman, and X. Dai. Extended Hot Halos around Isolated Galaxies Observed in the ROSAT All-Sky Survey. *Astrophysical Journal*, 762:106, January 2013.

L. Armillotta, F. Fraternali, and F. Marinacci. Efficiency of gas cooling and accretion at the disc-corona interface. *Monthly Notices of the RAS*, 462:4157–4170, November 2016.

M. Asplund, N. Grevesse, A. J. Sauval, and P. Scott. The Chemical Composition of the Sun. *Annual Review of Astron and Astrophys*, 47:481–522, September 2009.

J. Binney. The physics of dissipational galaxy formation. *Astrophysical Journal*, 215: 483–491, July 1977.

J. Binney and S. Tremaine. *Galactic dynamics*. 1987.

J. Binney, C. Nipoti, and F. Fraternali. Do high-velocity clouds form by thermal instability? *Monthly Notices of the RAS*, 397:1804–1815, August 2009.

Y. Birnboim and A. Dekel. Virial shocks in galactic haloes? *Monthly Notices of the RAS*, 345:349–364, October 2003.

M. R. Blanton, D. W. Hogg, N. A. Bahcall, J. Brinkmann, M. Britton, A. J. Connolly, I. Csabai, M. Fukugita, J. Loveday, A. Meiksin, J. A. Munn, R. C. Nichol, S. Okamura, T. Quinn, D. P. Schneider, K. Shimasaku, M. A. Strauss, M. Tegmark, M. S. Vogeley, and D. H. Weinberg. The Galaxy Luminosity Function and Luminosity Density at Redshift z = 0.1. *Astrophysical Journal*, 592:819–838, August 2003.

Á. Bogdán and M. Gilfanov. Unresolved and diffuse components of X-ray emission and X-ray-to-K-band luminosity ratios in nearby early-type and late-type galaxies. *Monthly Notices of the RAS*, 418:1901–1912, December 2011.

Á. Bogdán, W. R. Forman, M. Vogelsberger, H. Bourdin, D. Sijacki, P. Mazzotta, R. P. Kraft, C. Jones, M. Gilfanov, E. Churazov, and L. P. David. Hot X-Ray Coronae around Massive Spiral Galaxies: A Unique Probe of Structure Formation Models. *Astrophysical Journal*, 772:97, August 2013.

A. D. Bolatto, S. R. Warren, A. K. Leroy, F. Walter, S. Veilleux, E. C. Ostriker, J. Ott, M. Zwaan, D. B. Fisher, A. Weiss, E. Rosolowsky, and J. Hodge. Suppression of star formation in the galaxy NGC 253 by a starburst-driven molecular wind. *Nature*, 499:450–453, July 2013.

H.-W. Chen. The Circumgalactic Medium in Massive Halos. *ArXiv e-prints*, December 2016.

R. A. Crain, I. G. McCarthy, C. S. Frenk, T. Theuns, and J. Schaye. X-ray coronae in simulations of disc galaxy formation. *Monthly Notices of the RAS*, 407:1403–1422, September 2010.

N. H. M. Crighton, J. F. Hennawi, and J. X. Prochaska. Metal-poor, Cool Gas in the Circumgalactic Medium of a z = 2.4 Star-forming Galaxy: Direct Evidence for Cold Accretion? *Astrophysical Journal, Letters*, 776:L18, October 2013.

X. Dai, M. E. Anderson, J. N. Bregman, and J. M. Miller. XMM-Newton Detects a Hot Gaseous Halo in the Fastest Rotating Spiral Galaxy UGC 12591. *Astrophysical Journal*, 755:107, August 2012.

T. A. Davis, K. Alatalo, M. Sarzi, M. Bureau, L. M. Young, L. Blitz, P. Serra, A. F. Crocker, D. Krajnović, R. M. McDermid, M. Bois, F. Bournaud, M. Cappellari, R. L. Davies, P.-A. Duc, P. T. de Zeeuw, E. Emsellem, S. Khochfar, H. Kuntschner, P.-Y. Lablanche, R. Morganti, T. Naab, T. Oosterloo, N. Scott, and A.-M. Weijmans. The ATLAS^{3D} project - X. On the origin of the molecular and ionized gas in early-type galaxies. *Monthly Notices of the RAS*, 417:882–899, October 2011.

A. Dekel and Y. Birnboim. Galaxy bimodality due to cold flows and shock heating. *Monthly Notices of the RAS*, 368:2–20, May 2006.

G. J. Ferland, K. T. Korista, D. A. Verner, J. W. Ferguson, J. B. Kingdon, and E. M. Verner. CLOUDY 90: Numerical Simulation of Plasmas and Their Spectra. *Publications of the ASP*, 110:761–778, July 1998.

G. B. Field. Thermal Instability. *Astrophysical Journal*, 142:531, August 1965.

A. Finoguenov and C. Jones. SN IA Enrichment in Virgo Early-type Galaxies from ROSAT and ASCA Observations. *Astrophysical Journal*, 539:603–617, August 2000.

A. B. Ford, B. D. Oppenheimer, R. Davé, N. Katz, J. A. Kollmeier, and D. H. Weinberg. Hydrogen and metal line absorption around low-redshift galaxies in cosmological hydrodynamic simulations. *Monthly Notices of the RAS*, 432:89–112, June 2013.

W. Forman, J. Schwarz, C. Jones, W. Liller, and A. C. Fabian. X-ray observations of galaxies in the Virgo cluster. *Astrophysical Journal, Letters*, 234:L27–L31, November 1979.

W. Forman, C. Jones, and W. Tucker. Hot coronae around early-type galaxies. *Astrophysical Journal*, 293:102–119, June 1985.

A. J. Fox, B. P. Wakker, J. V. Smoker, P. Richter, B. D. Savage, and K. R. Sembach. Exploring the Origin and Fate of the Magellanic Stream with Ultraviolet and Optical Absorption. *Astrophysical Journal*, 718:1046–1061, August 2010.

F. Fraternali and J. J. Binney. Accretion of gas on to nearby spiral galaxies. *Monthly Notices of the RAS*, 386:935–944, May 2008.

F. Fraternali, A. Marasco, F. Marinacci, and J. Binney. Ionized Absorbers as Evidence for Supernova-driven Cooling of the Lower Galactic Corona. *Astrophysical Journal, Letters*, 764:L21, February 2013.

C. S. Froning and J. C. Green. The cosmic origins spectrograph: capabilities and prelaunch performance. *Astrophysics and Space Science*, 320:181–185, April 2009.

A. Gatto, F. Fraternali, J. I. Read, F. Marinacci, H. Lux, and S. Walch. Unveiling the corona of the Milky Way via ram-pressure stripping of dwarf satellites. *Monthly Notices of the RAS*, 433:2749–2763, August 2013.

J. C. Green, C. S. Froning, S. Osterman, D. Ebbets, S. H. Heap, C. Leitherer, J. L. Linsky, B. D. Savage, K. Sembach, J. M. Shull, O. H. W. Siegmund, T. P. Snow, J. Spencer, S. A. Stern, J. Stocke, B. Welsh, S. Béland, E. B. Burgh, C. Danforth, K. France, B. Keeney, J. McPhate, S. V. Penton, J. Andrews, K. Brownsberger, J. Morse, and E. Wilkinson. The Cosmic Origins Spectrograph. *Astrophysical Journal*, 744:60, January 2012.

N. Grevesse and A. J. Sauval. Standard Solar Composition. *Space Science Reviews*, 85:161–174, May 1998.

F. Haardt and P. Madau. Modelling the UV/X-ray cosmic background with CUBA. In D. M. Neumann and J. T. V. Tran, editors, *Clusters of Galaxies and the High Redshift Universe Observed in X-rays*, 2001.

T. M. Heckman, M. D. Lehnert, D. K. Strickland, and L. Armus. Absorption-Line Probes of Gas and Dust in Galactic Superwinds. *Astrophysical Journal, Supplement*, 129:493–516, August 2000.

H. Holweger. Photospheric abundances: Problems, updates, implications. In R. F. Wimmer-Schweingruber, editor, *Joint SOHO/ACE workshop "Solar and Galactic Composition"*, volume 598 of *American Institute of Physics Conference Series*, pages 23–30, November 2001.

Y.-H. Huang, H.-W. Chen, S. D. Johnson, and B. J. Weiner. Characterizing the chemically enriched circumgalactic medium of 38 000 luminous red galaxies in SDSS DR12. *Monthly Notices of the RAS*, 455:1713–1727, January 2016.

P. J. Humphrey, D. A. Buote, C. R. Canizares, A. C. Fabian, and J. M. Miller. A Census of Baryons and Dark Matter in an Isolated, Milky Way Sized Elliptical Galaxy. *Astrophysical Journal*, 729:53, March 2011.

C. Jones, W. Forman, A. Vikhlinin, M. Markevitch, L. David, A. Warmflash, S. Murray, and P. E. J. Nulsen. Chandra Observations of NGC 4636-an Elliptical Galaxy in Turmoil. *Astrophysical Journal, Letters*, 567:L115–L118, March 2002.

G. G. Kacprzak and C. W. Churchill. The H I Mass Density in Galactic Halos, Winds, and Cold Accretion as Traced by Mg II Absorption. *Astrophysical Journal, Letters*, 743:L34, December 2011.

G. G. Kacprzak, C. L. Martin, N. Bouché, C. W. Churchill, J. Cooke, A. LeReun, I. Schroetter, S. H. Ho, and E. Klimek. New Perspective on Galaxy Outflows from the First Detection of Both Intrinsic and Traverse Metal-line Absorption. *Astrophysical Journal, Letters*, 792:L12, September 2014.

R. C. Kennicutt, Jr. The Global Schmidt Law in Star-forming Galaxies. *Astrophysical Journal*, 498:541–552, May 1998.

D. Kereš, N. Katz, M. Fardal, R. Davé, and D. H. Weinberg. Galaxies in a simulated ΛCDM Universe - I. Cold mode and hot cores. *Monthly Notices of the RAS*, 395: 160–179, May 2009.

L. J. Kewley, M. J. Geller, and R. A. Jansen. [O II] as a Star Formation Rate Indicator. *Astronomical Journal*, 127:2002–2030, April 2004.

B. P. Koester, T. A. McKay, J. Annis, R. H. Wechsler, A. Evrard, L. Bleem, M. Becker, D. Johnston, E. Sheldon, R. Nichol, C. Miller, R. Scranton, N. Bahcall, J. Barentine, H. Brewington, J. Brinkmann, M. Harvanek, S. Kleinman, J. Krzesinski, D. Long, A. Nitta, D. P. Schneider, S. Sneddin, W. Voges, and D. York. A MaxBCG Catalog

of 13,823 Galaxy Clusters from the Sloan Digital Sky Survey. *Astrophysical Journal*, 660:239–255, May 2007.

K. M. Lanzetta, A. M. Wolfe, and D. A. Turnshek. The IUE Survey for Damped Lyman-alpha and Lyman-Limit Absorption Systems: Evolution of the Gaseous Content of the Universe. *Astrophysical Journal*, 440:435, February 1995.

A. H. Maller and J. S. Bullock. Multiphase galaxy formation: high-velocity clouds and the missing baryon problem. *Monthly Notices of the RAS*, 355:694–712, December 2004.

F. Marinacci, J. Binney, F. Fraternali, C. Nipoti, L. Ciotti, and P. Londrillo. The mode of gas accretion on to star-forming galaxies. *Monthly Notices of the RAS*, 404: 1464–1474, May 2010.

F. Marinacci, F. Fraternali, C. Nipoti, J. Binney, L. Ciotti, and P. Londrillo. Galactic fountains and the rotation of disc-galaxy coronae. *Monthly Notices of the RAS*, 415: 1534–1542, August 2011.

C. L. Martin, A. E. Shapley, A. L. Coil, K. A. Kornei, K. Bundy, B. J. Weiner, K. G. Noeske, and D. Schiminovich. Demographics and Physical Properties of Gas Outflows/Inflows at $0.4 < z < 1.4$. *Astrophysical Journal*, 760:127, December 2012.

W. G. Mathews and F. Brighenti. Hot Gas in and around Elliptical Galaxies. *Annual Review of Astron and Astrophys*, 41:191–239, 2003.

M. McCourt, S. P. Oh, R. M. O'Leary, and A.-M. Madigan. A Characteristic Scale for Cold Gas. *ArXiv e-prints*, October 2016.

S. S. McGaugh, J. M. Schombert, W. J. G. de Blok, and M. J. Zagursky. The Baryon Content of Cosmic Structures. *Astrophysical Journal, Letters*, 708:L14–L17, January 2010.

M. J. Miller and J. N. Bregman. The Structure of the Milky Way's Hot Gas Halo. *Astrophysical Journal*, 770:118, June 2013.

M. J. Miller and J. N. Bregman. Constraining the Milky Way's Hot Gas Halo with O VII and O VIII Emission Lines. *Astrophysical Journal*, 800:14, February 2015.

B. P. Moster, R. S. Somerville, C. Maulbetsch, F. C. van den Bosch, A. V. Macciò, T. Naab, and L. Oser. Constraints on the Relationship between Stellar Mass and Halo Mass at Low and High Redshift. *Astrophysical Journal*, 710:903–923, February 2010.

J. F. Navarro, C. S. Frenk, and S. D. M. White. Simulations of X-ray clusters. *Monthly Notices of the RAS*, 275:720–740, August 1995.

J. H. Oort. The formation of galaxies and the origin of the high-velocity hydrogen. *Astronomy and Astrophysics*, 7:381–404, September 1970.

T. Oosterloo, F. Fraternali, and R. Sancisi. The Cold Gaseous Halo of NGC 891. *Astronomical Journal*, 134:1019, September 2007.

S. V. Penton, J. T. Stocke, and J. M. Shull. The Local Lyalpha Forest. III. Relationship between Lyalpha Absorbers and Galaxies, Voids, and Superclusters. *Astrophysical Journal*, 565:720–742, February 2002.

Planck Collaboration, P. A. R. Ade, N. Aghanim, M. Arnaud, M. Ashdown, J. Aumont, C. Baccigalupi, A. J. Banday, R. B. Barreiro, J. G. Bartlett, and et al. Planck 2015 results. XIII. Cosmological parameters. *Astronomy and Astrophysics*, 594:A13, September 2016.

J. X. Prochaska, B. Weiner, H.-W. Chen, J. Mulchaey, and K. Cooksey. Probing the Intergalactic Medium/Galaxy Connection. V. On the Origin of Lyalpha and O VI Absorption at z $<$ 0.2. *Astrophysical Journal*, 740:91, October 2011.

M. E. Putman, D. R. Saul, and E. Mets. Head-tail clouds: drops to probe the diffuse Galactic halo. *Monthly Notices of the RAS*, 418:1575–1586, December 2011.

M. J. Rees and J. P. Ostriker. Cooling, dynamics and fragmentation of massive gas clouds - Clues to the masses and radii of galaxies and clusters. *Monthly Notices of the RAS*, 179:541–559, June 1977.

K. H. R. Rubin, B. J. Weiner, D. C. Koo, C. L. Martin, J. X. Prochaska, A. L. Coil, and J. A. Newman. The Persistence of Cool Galactic Winds in High Stellar Mass Galaxies between z = 1.4 and 1. *Astrophysical Journal*, 719:1503–1525, August 2010.

K. H. R. Rubin, J. X. Prochaska, D. C. Koo, and A. C. Phillips. The Direct Detection of Cool, Metal-enriched Gas Accretion onto Galaxies at z ˜ 0.5. *Astrophysical Journal, Letters*, 747:L26, March 2012.

K. H. R. Rubin, J. X. Prochaska, D. C. Koo, A. C. Phillips, C. L. Martin, and L. O. Winstrom. Evidence for Ubiquitous Collimated Galactic-scale Outflows along the Star-forming Sequence at z = 0.5. *Astrophysical Journal*, 794:156, October 2014.

R. Sancisi, F. Fraternali, T. Oosterloo, and T. van der Hulst. Cold gas accretion in galaxies. *Astronomy and Astrophysics Reviews*, 15:189–223, June 2008.

C. L. Sarazin, J. A. Irwin, and J. N. Bregman. Chandra X-Ray Observations of the X-Ray Faint Elliptical Galaxy NGC 4697. *Astrophysical Journal*, 556:533–555, August 2001.

B. D. Savage and K. R. Sembach. Interstellar Abundances from Absorption-Line Observations with the Hubble Space Telescope. *Annual Review of Astron and Astrophys*, 34:279–330, 1996.

K. R. Sembach, B. P. Wakker, B. D. Savage, P. Richter, M. Meade, J. M. Shull, E. B. Jenkins, G. Sonneborn, and H. W. Moos. Highly Ionized High-Velocity Gas in the Vicinity of the Galaxy. *Astrophysical Journal, Supplement*, 146:165–208, May 2003.

P. Serra, T. Oosterloo, R. Morganti, K. Alatalo, L. Blitz, M. Bois, F. Bournaud, M. Bureau, M. Cappellari, A. F. Crocker, R. L. Davies, T. A. Davis, P. T. de Zeeuw, P.-A. Duc, E. Emsellem, S. Khochfar, D. Krajnović, H. Kuntschner, P.-Y. Lablanche, R. M. McDermid, T. Naab, M. Sarzi, N. Scott, S. C. Trager, A.-M. Weijmans, and L. M. Young. The ATLAS^{3D} project - XIII. Mass and morphology of H I in early-type galaxies as a function of environment. *Monthly Notices of the RAS*, 422:1835–1862, May 2012.

A. E. Shapley, C. C. Steidel, M. Pettini, and K. L. Adelberger. Rest-Frame Ultraviolet Spectra of z=3 Lyman Break Galaxies. *Astrophysical Journal*, 588:65–89, May 2003. doi: 10.1086/373922.

J. M. Shull. Where do Galaxies End? *Astrophysical Journal*, 784:142, April 2014.

L. Spitzer, Jr. On a Possible Interstellar Galactic Corona. *Astrophysical Journal*, 124: 20, July 1956.

J. Stern, J. F. Hennawi, J. X. Prochaska, and J. K. Werk. A Universal Density Structure for Circumgalactic Gas. *Astrophysical Journal*, 830:87, October 2016.

J. T. Stocke, J. M. Shull, S. Penton, M. Donahue, and C. Carilli. The Local LY alpha Forest: Association of Clouds with Superclusters and Voids. *Astrophysical Journal*, 451:24, September 1995.

J. M. Stone, T. A. Gardiner, P. Teuben, J. F. Hawley, and J. B. Simon. Athena: A New Code for Astrophysical MHD. *Astrophysical Journal, Supplement*, 178:137-177, September 2008.

D. K. Strickland and T. M. Heckman. Iron Line and Diffuse Hard X-Ray Emission from the Starburst Galaxy M82. *Astrophysical Journal*, 658:258–281, March 2007.

R. S. Sutherland and M. A. Dopita. Cooling functions for low-density astrophysical plasmas. *Astrophysical Journal, Supplement*, 88:253–327, September 1993.

C. Thom, J. Tumlinson, J. K. Werk, J. X. Prochaska, B. D. Oppenheimer, M. S. Peeples, T. M. Tripp, N. S. Katz, J. M. O'Meara, A. B. Ford, R. Davé, K. R. Sembach, and D. H. Weinberg. Not Dead Yet: Cool Circumgalactic Gas in the Halos of Early-type Galaxies. *Astrophysical Journal, Letters*, 758:L41, October 2012.

J. Tumlinson, C. Thom, J. K. Werk, J. X. Prochaska, T. M. Tripp, D. H. Weinberg, M. S. Peeples, J. M. O'Meara, B. D. Oppenheimer, J. D. Meiring, N. S. Katz, R. Davé, A. B. Ford, and K. R. Sembach. The Large, Oxygen-Rich Halos of Star-Forming Galaxies Are a Major Reservoir of Galactic Metals. *Science*, 334: 948, November 2011.

J. Tumlinson, C. Thom, J. K. Werk, J. X. Prochaska, T. M. Tripp, N. Katz, R. Davé, B. D. Oppenheimer, J. D. Meiring, A. B. Ford, J. M. O'Meara, M. S. Peeples, K. R. Sembach, and D. H. Weinberg. The COS-Halos Survey: Rationale, Design, and a Census of Circumgalactic Neutral Hydrogen. *Astrophysical Journal*, 777:59, November 2013.

B. P. Wakker. High-velocity clouds. In H. Bloemen, editor, *The Interstellar Disk-Halo Connection in Galaxies*, volume 144 of *IAU Symposium*, 1991.

B. P. Wakker and B. D. Savage. The Relationship Between Intergalactic H I/O VI and Nearby ($z < 0.017$) Galaxies. *Astrophysical Journal, Supplement*, 182:378–467, May 2009.

B. P. Wakker and H. van Woerden. High-Velocity Clouds. *Annual Review of Astron and Astrophys*, 35:217–266, 1997.

B. J. Weiner, A. L. Coil, J. X. Prochaska, J. A. Newman, M. C. Cooper, K. Bundy, C. J. Conselice, A. A. Dutton, S. M. Faber, D. C. Koo, J. M. Lotz, G. H. Rieke, and K. H. R. Rubin. Ubiquitous Outflows in DEEP2 Spectra of Star-Forming Galaxies at $z = 1.4$. *Astrophysical Journal*, 692:187–211, February 2009.

J. K. Werk, J. X. Prochaska, C. Thom, J. Tumlinson, T. M. Tripp, J. M. O'Meara, and M. S. Peeples. The COS-Halos Survey: An Empirical Description of Metal-line Absorption in the Low-redshift Circumgalactic Medium. *Astrophysical Journal, Supplement*, 204:17, February 2013.

J. K. Werk, J. X. Prochaska, J. Tumlinson, M. S. Peeples, T. M. Tripp, A. J. Fox, N. Lehner, C. Thom, J. M. O'Meara, A. B. Ford, R. Bordoloi, N. Katz, N. Tejos, B. D. Oppenheimer, R. Davé, and D. H. Weinberg. The COS-Halos Survey: Physical Conditions and Baryonic Mass in the Low-redshift Circumgalactic Medium. *Astrophysical Journal*, 792:8, September 2014.

J. K. Werk, J. X. Prochaska, S. Cantalupo, A. J. Fox, B. Oppenheimer, J. Tumlinson, T. M. Tripp, N. Lehner, and M. McQuinn. The COS-Halos Survey: Origins of the Highly Ionized Circumgalactic Medium of Star-Forming Galaxies. *Astrophysical Journal*, 833:54, December 2016.

S. D. M. White and C. S. Frenk. Galaxy formation through hierarchical clustering. *Astrophysical Journal*, 379:52–79, September 1991. doi: 10.1086/170483.

S. D. M. White and M. J. Rees. Core condensation in heavy halos - A two-stage theory for galaxy formation and clustering. *Monthly Notices of the RAS*, 183:341–358, May 1978.

Y. Yao, J. M. Shull, Q. D. Wang, and W. Cash. Detecting the Warm-Hot Intergalactic Medium through X-Ray Absorption Lines. *Astrophysical Journal*, 746:166, February 2012.

L. M. Young, M. Bureau, T. A. Davis, F. Combes, R. M. McDermid, K. Alatalo, L. Blitz, M. Bois, F. Bournaud, M. Cappellari, R. L. Davies, P. T. de Zeeuw, E. Emsellem, S. Khochfar, D. Krajnović, H. Kuntschner, P.-Y. Lablanche, R. Morganti, T. Naab, T. Oosterloo, M. Sarzi, N. Scott, P. Serra, and A.-M. Weijmans. The ATLAS^{3D} project - IV. The molecular gas content of early-type galaxies. *Monthly Notices of the RAS*, 414:940–967, June 2011.

G. Zhu, B. Ménard, D. Bizyaev, H. Brewington, G. Ebelke, S. Ho, K. Kinemuchi, V. Malanushenko, E. Malanushenko, M. Marchante, S. More, D. Oravetz, K. Pan, P. Petitjean, and A. Simmons. The large-scale distribution of cool gas around luminous red galaxies. *Monthly Notices of the RAS*, 439:3139–3155, April 2014.